

8-2018

Plasma based synthesis and surface modification of graphene.

Rong Zhao
University of Louisville

Follow this and additional works at: <https://ir.library.louisville.edu/etd>

 Part of the [Condensed Matter Physics Commons](#)

Recommended Citation

Zhao, Rong, "Plasma based synthesis and surface modification of graphene." (2018). *Electronic Theses and Dissertations*. Paper 3042.
<https://doi.org/10.18297/etd/3042>

This Doctoral Dissertation is brought to you for free and open access by ThinkIR: The University of Louisville's Institutional Repository. It has been accepted for inclusion in Electronic Theses and Dissertations by an authorized administrator of ThinkIR: The University of Louisville's Institutional Repository. This title appears here courtesy of the author, who has retained all other copyrights. For more information, please contact thinkir@louisville.edu.

PLASMA BASED SYNTHESIS AND SURFACE MODIFICATION OF GRAPHENE

By

Rong Zhao

B.S., Xidian University, 2008
M.S., Shanghai University, 2013
M.S., University of Louisville, 2015

A Dissertation
Submitted to the Faculty of the
College of Arts and Sciences of the University of Louisville
in Partial Fulfillment of the Requirements
For the Degree of

Doctor of Philosophy in Physics

Department of Physics and Astronomy
University of Louisville
Louisville, Kentucky

August 2018

PLASMA BASED SYNTHESIS AND SURFACE MODIFICATION OF GRAPHENE

By

Rong Zhao

B.S., Xidian University, 2008
M.S., Shanghai University, 2013
M.S., University of Louisville, 2015

A Dissertation Approved on

July 16th, 2018

By the Following Dissertation Committee:

Dr. Gamini Sumanasekera (Dissertation Director)

Dr. Chakram. S. Jayanthi

Dr. Ming Yu

Dr. Shamus P. McNamara

ACKNOWLEDGEMENTS

It is a pleasure to thank the many people who made this thesis possible. Foremost, I would like to express my sincere gratitude to my advisor Dr. Gamini Sumanasekera for the continuous support of my Ph.D. study and research, for his patience, motivation, enthusiasm, and immense knowledge. His guidance helped me in all the time of research and writing of this thesis. His suggestions and discussions have always led me back on track whenever I have been lost or confused. Many thanks to Dr. C. S. Jayanthi and Dr. Chris. L Davis who have worked extremely hard to ensure I was funded during my Ph. D. study and always available when I needed advice. Dr. Ming Yu has greatly impacted my life by first introducing me to University of Louisville and helps me a lot in my research and life. I thank Dr. Shamus P. McNamara for being a part of my committee in addition to providing advice and guidance that has improved my thesis. I would like to offer special thanks to Dr. Shi-Yu Wu, who although no longer with us, continues to inspire me. I would also like to express my appreciations to all the professors within the Department of Physics and Astronomy, the supporting staff, especially Ms. Mary Gayle Wrocklage, Ms. Rea Diehlmann and Joshua Rimmer. I thank my lab partners Ruchira Dharmasena, Adel Alruqi, Meysam Akhtar, George Anderson, Taruq Afaneh, Andry Sherehiy for making the lab experience educational and enjoyable.

And last but not least, I want to thank my daughter Kathy Zhao. It was not possible to write this thesis without looking into her lovely face, hugging her and listening her

moving laughter. Words cannot express how much I am grateful to Congyan Zhang who is my best friend, colleague, beloved love and wife for her endless support and love. I am so fortunate having such wonderful parents; Deyuan Zhao and Liancui Wu; brother Ying Zhao and sisters Jing Zhao and Zhen Zhao that continuously support and help me through my life.

ABSTRACT

PLASMA BASED SYNTHESIS AND SURFACE MODIFICATION OF GRAPHENE

Rong Zhao

July 16th, 2018

Graphene, an atom thick layer of carbon, has attracted intense scientific interest due to its exceptional electrical, mechanical and chemical properties. Especially, it provides a perfect platform to explore the unique electronic properties in absolute two-dimension. Pristine graphene possesses zero band gap and weakens its competitiveness in the field of semiconductors. In order to induce a band gap and control its semiconducting properties, functionalization and doping are two of the most feasible methods. In the context of functionalization, large area monolayer graphene synthesized by chemical vapor deposition was subjected to controlled and sequential fluorination using radio frequency plasma while monitoring its electrical properties. It was found that the initial metallic behavior of pristine graphene changes to insulating behavior with fluorination progresses where transport properties obey variable range hopping (VRH). As determined by the high temperature resistance behavior, an emergence of a small band gap is observed and the band gap is seen to increase as the fluorination progresses.

Next, we studied the transport properties of graphene with plasma induced nitrogen doping. The nitrogen is presumed to be incorporated into the carbon lattice of graphene by

making covalent bonding as observed by the swinging of the sign of the thermopower from (initial) positive to (eventual) negative.

We have even observed significant changes in electrical transport properties of graphene upon adsorption of noble gasses. The strength of the van der Waals interactions between noble gases and carbon was found to follow the order $\text{Kr} > \text{Ar} > \text{He}$.

In addition, we investigated the electrical transport properties of uniform and vertically oriented graphene nanowalls directly synthesized on multiple substrates using plasma enhanced chemical vapor deposition at lower temperatures. The temperature for optimum growth was established with the aid of transmission electron microscopy, scanning electron microscopy, and Raman spectroscopy analysis of the growth products. This approach offers means for low-cost graphene fabrication as well as avoidance of the inconvenient post growth transfer processes commonly used.

TABLE OF CONTENTS

ACKNOWLEDGMENTS	ii
ABSTRACT.....	v
LIST OF TABLES	x
LIST OF FIGURES	xi
CHAPTER 01 INTRODUCTION.....	1
1.1 Background of graphene.....	1
1.2 Band structure of graphene.....	4
1.3 Properties and potential applications of graphene	7
1.4 Synthesis of graphene	11
1.4.1 Mechanical exfoliation	12
1.4.2 Liquid phase exfoliation	14
1.4.3 Epitaxial growth	15
1.4.4 Chemically derived graphene	16
CHAPTER 02 CHEMICAL VAPOR DEPOSITION (CVD) OF GRAPHENE: SYNTHESIS AND CHARACTERIZATION	18
2.1 CVD of graphene	18
2.2 Transfer of graphene films.....	22
2.3 Plasma Enhanced CVD of graphene.....	24

2.4 Electrical properties of materials	26
2.4.1 The electrical conductivity	26
2.4.2 Four probe resistivity for sheet resistance	27
2.4.3 Hall mobility measurements	29
2.4.4 Thermoelectric power.....	31
2.5 Characterization of graphene	33
2.5.1 Raman Spectroscopy	33
2.5.2 Scanning electron microscope	36
2.5.3 Transmission electron microscopy	37
2.5.4 X-ray photoelectron spectroscopy	39
 CHAPTER 03 FLUORINATION OF GRAPHENE: TRANSPORT PROPERTIES AND BAND GAP FORMATION	 42
3.1 Introduction.....	42
3.2 <i>in-situ</i> functionalization of graphene	44
3.3 <i>ex-situ</i> characterization of fluorinated graphene.....	48
3.4 Conclusions.....	59
 CHAPTER 04 NITROGEN DOPING OF GRAPHENE: TRANSPORT PROPERTIES.....	 60
4.1 Introduction.....	60
4.2 Nitrogen doping of graphene	62

4.3 <i>in-situ</i> characterization of nitrogen doping of graphene	63
4.4 <i>ex-situ</i> characterization of nitrogen doped graphene	66
4.5 Conclusion	73
CHAPTER 05 TRANSPORT PROPERTIES OF GRAPHENE-NOBLE GAS	
ADSORPTION.	74
5.1 Introduction.....	74
5.2 Noble gas adsorption of graphene	75
5.3 Conclusion	80
CHAPTER 06 SYNTHESIS AND CHARACTERIZATION OF PECVD GRAPHENE	
NANOWALLS.	82
6.1 Introduction.....	82
6.2 Plasma Enhanced CVD of graphene nanowalls	84
6.3 Surface characterization of PECVD graphene nanowalls	86
6.4 Electronic properties of PECVD graphene nanowalls.....	91
6.5 Conclusion	99
REFERENCES... ..	100
CURRICULUM VITAE.....	129

LIST OF TABLES

Table 1. Properties of graphene.....	9
Table 2. Carbon solubility and the growth mechanism on typical metals for CVD graphene [33]......	19
Table 3. Bulk resistivity or sheet resistance R_{sh} for the case of linear and square arrangements of four probes on a semi-infinite 3D material, infinite 2D sheet, and 1D wire.	29
Table 4. Fitted parameters for graphene samples on glass at varying growth temperatures.	97

LIST OF FIGURES

Figure 1.1 Schematic illustration of the 0D (fullerene), 1D (carbon nanotube) and 2D (graphene) nanostructure of carbon-based materials [1].....	2
Figure 1.2 Number of publications (article, proceeding paper, review or letter) related to graphene per year. Source: Thomas Reuters Web of Science, as 12.31.2017. ...	3
Figure 1.3 (a) Left: the band structure of graphene in the honeycomb lattice. Right: zoom-in of the energy bands close to one of the Dirac points [5]. (b) The hexagonal lattice of graphene, with the nearest neighbor δ_i and the primitive, a_i vectors depicted. The area of the primitive cell is $A_c = 33a_0^2/2 \approx 5.1 \text{ \AA}^2$ and $a_0 \approx 1.42 \text{ \AA}$. (c) The Brillouin zone of graphene, with the Dirac points K and K' indicated.	4
Figure 1.4 Industrial applications of graphene-based materials [29].....	10
Figure 1.5 TD and BU synthesis compared (not to scale). (a) TD synthesis showing a wooden statue of an owl made from a tree. (b) BU synthesis where a tree is derived from an acorn. (c) BU synthesis where a seed might be programmed, via DNA, to directly form a wooden statue [30].	11
Figure 1.6 A process flow chart of Graphene synthesis [38].....	12
Figure 1.7 Schematic representation of sequential steps followed to exfoliate graphene layers using the scotch tape method [45].	13

Figure 1.8 Schematic diagram of liquid phase exfoliation method [55].....	15
Figure 1.9 Basics of epitaxial thermal growth graphene on SiC substrate [58].	16
Figure 1.10 Scheme showing the chemical route for the synthesis of graphene [66].	17
Figure 2.1 Schematics of CVD graphene grown on (a) metals with high carbon solubility, (b) Cu foil, (c) Cu enclosure, and (d) sapphire [33].....	20
Figure 2.2 Schematic diagram of CVD growth of graphene.	21
Figure 2.3 Temperature curve during the CVD growth of graphene.....	22
Figure 2.4 Schematic diagram of graphene transferring on target substrate.	23
Figure 2.5 Mechanism of growth of graphene that involves decomposition of CH ₄ /H ₂ mixed plasma.	25
Figure 2.6 Room-temperature conductivity of various materials. (Superconductors, having conductivities many orders of magnitude larger than copper, near 0 K, are not shown. The conductivity of semiconductors varies substantially with temperature and purity.).....	27
Figure 2.7 Schematic of a square 4P probe configuration with $s_1 = s_4 = s$ and $s_2 = s_3 = 2s$	28
Figure 2.8 Schematic of (a) Van der Pauw configuration used in the determination of the Hall voltage V_H . (b) the sample placed in the magnetic field.	29
Figure 2.9 Schematic diagram of the circuit [99].	31
Figure 2.10 The energy diagram of Rayleigh and Raman scattering.	33

Figure 2.11 (a) Raman spectra of graphene, (b) The position of G band for different layer number of graphene, (c) 2D band method for the determination of the layer number of graphene [103].	36
Figure 2.12 Schematic of Scanning Electron Microscope internal components.	36
Figure 2.13 (a) A SEM micrograph showing the edge of a transferred graphene sheet on the SiO ₂ /Si substrate; b) a highly corrugated structure with small and big wrinkles, indicated as the blue circle and yellow circle, respectively; c) a schematic depicting the roughness contrast for a corrugated graphene sheet on the SiO ₂ /Si substrate [105].	37
Figure 2.14 Basic principle of Transmission Electron Microscopy (TEM).	38
Figure 2.15 A HR-TEM image of a folding edge of graphene flake show dark and bright lines.	39
Figure 2.16 Schematic of X-ray photoelectron spectroscopy.	40
Figure 3.1 Example of chemical bonds in fluorinated graphene.	43
Figure 3.2 Schematic of plasma functionalization setup and graphene sample on chip carrier for <i>in-situ</i> measurements.	45
Figure 3.3 Resistance and thermopower of graphene during annealing.	46
Figure 3.4 Time dependence of the resistance, R(t) and thermopower, S(t) during fluorination. The arrowheads indicate the initiation of plasma.	47
Figure 3.5 Temperature dependence of the four-probe resistance, R(T) of fluorinated graphene samples including the pristine and degassed graphene.	48

Figure 3.6 (a) $\text{Log}(G)$ vs $\text{Log}(T)$ plot for progressively fluorinated graphene samples. (b) G vs $T^{1/3}$ plot for the three curves represented by F, G, and H (only low temperature data is shown).....	49
Figure 3.7 $\text{Log}(R)$ vs $T^{-1/3}$ plot for VRH analysis.....	50
Figure 3.8 T_0 vs. R/R_0 values (T_0 is extracted from VRH fitting and R_0 is the room temperature resistance).....	51
Figure 3.9 Raman spectroscopy results for (a) pristine and progressively fluorinated graphene (b) evolution of the D band (c) deconvolution of the G and D' bands and (d) Ratio of intensities of D and G bands, I_D/I_G vs. R/R_0	52
Figure 3.10 (a) Normalized Magnetoresistance ($\Delta R/R$) data for progressively fluorinated graphene. Data for the untreated graphene is also shown. (b) Normalized Magnetoresistance ($\Delta R/R$) data and the best fit for WL theory. Each data set has been offset in the ordinate for clarity.	54
Figure 3.11 The temperature dependence of (a) thermopower, $S(T)$. (b) Hall voltage over excitation current, V_H/I for progressively fluorinated graphene.	57
Figure 3.12 The Arrhenius plot of $\text{Ln}(R)$ vs $1/(k_B T)$ for densely fluorinated graphene samples at higher temperatures. The slope of the linear range is used to extract the band gap values.	58
Figure 4.1 Schematic band structures of graphene. (a) Band structure of pristine graphene with zero bandgap. Band structures of (b) p-type and (c) n-type graphene with the bandgap.	61
Figure 4.2 Three common bonding configurations of Nitrogen-doped Graphene [139]..	62

Figure 4.3 Schematic of the plasma doping of graphene and <i>in-situ</i> measurement setup.	64
Figure 4.4 (a) In situ time evolution of the resistance, $R(t)$ and (b) thermopower, $S(t)$ during nitrogen doping. The arrowheads represent the initiation of intermittent plasma.	65
Figure 4.5 Temperature dependence of Resistance (Right axis) and Thermopower (left axis) of graphene before and after nitrogen doping. Inset: Low temperature (below 50K) resistance behavior with logarithmic temperature axis.....	67
Figure 4.6 Magnetotransport: Magnetoresistance (MR) data for pristine and nitrogen-doped graphene. Dataset is offset for clarity.....	68
Figure 4.7 Magnetotransport: $(\Delta R/R)$ data for pristine and nitrogen-doped graphene with the best fit for WL theory at low magnetic field values in logarithmic B axis.	69
Figure 4.8 The Raman spectra of graphene sample before and after nitrogen doping.	70
Figure 4.9 XPS survey spectrum of nitrogen doped graphene	71
Figure 4.10 (a) The C1s XPS peak, (b) the N1s XPS peak for nitrogen-doped graphene	72
Figure 5.1 Three different adsorption sites on top of graphene: above (a), bridge (b) and center (c).....	75
Figure 5.2 Schematic of the gas absorption measurement setup.	76
Figure 5.3 Resistance of graphene during noble gas adsorption and desorption.....	77
Figure 5.4 Thermopower of graphene during noble gas adsorption and desorption.	78
Figure 5.5 Temperature dependent on resistance for graphene with different noble gases adsorption.....	79

Figure 5.6 Temperature dependent of thermopower of graphene with different noble gases adsorption.....	80
Figure 6.1 Schematic illustration of graphene nanowalls.....	83
Figure 6.2 Home-made split ring radiofrequency plasma enhanced CVD system.....	85
Figure 6.3 (a) Optical image of graphene nanowalls on glass substrate; (b) on SiO ₂ /Si wafer, (c) SEM image of graphene nanowalls on glass substrate, (d) pattern growth of graphene on SiO ₂ /Si wafer.....	87
Figure 6.4 Raman spectra of graphene nanowalls on Cu, glass and SiO ₂ /Si substrates... ..	87
Figure 6.5 Raman spectra of the graphene nanowalls directly deposited on glass substrates at different growth temperature. The inset is the relative intensity ratio of I _{2D} /I _G	88
Figure 6.6 SEM images for the graphene nanowalls directly deposited on glass substrate at different growth temperatures.....	89
Figure 6.7 HRTEM image of graphene nanowalls synthesized at different temperature, left: 550 °C, right: 650 °C.....	91
Figure 6.8 (a) Temperature dependence of 4-probe resistance for graphene nanowalls grown at varying temperatures (b) Temperature dependence of Hall voltage over excitation current, V_H/I for graphene on glass at 650 °C. The inset shows V_H vs I curve at 300 K and 50 K.....	92
Figure 6.9 Best fits (black curves) of temperature dependent resistance for graphene on glass deposited at different temperatures (a) Best fits for VRH model at low temperatures (b) Best fits for TA model at high temperatures.....	93

Figure 6.10 T_0 values (extracted from VRH fitting to resistance data) for each synthesis temperature vs. $I(D)/I(G)$ ratio. The ξ localization lengths are plotted in the right-hand axis of Figure 5..... 95

Figure 6.11 Best fits (black curves) of temperature dependent TEP for graphene nanowalls on glass deposited at different temperatures. 96

Figure 6.12 Comparison of 4-probe resistance (top) and thermopower (bottom) of CVD graphene grown on copper foils at 1000 °C and PECVD graphene nanowalls grown on glass at 600 °C..... 98

CHAPTER 01

INTRODUCTION

1.1 Background of graphene

Carbon, belonging to the group-14 of the Periodic Table is present in all organic compounds, the earth's crust, and atmosphere etc. Carbon-based systems show an unlimited number of different structures with large variety of physical properties due to the flexibility of its chemical bonding. The best known all-carbon structures are graphite, diamond and amorphous carbon. The atomic number of carbon is six with a $2s^2 2p^2$ electron configuration. It tends to form covalent chemical bonds between carbon atoms with sp^1 , sp^2 , and sp^3 hybridization. Graphite is a typical sp^2 hybridized carbon allotrope and it is a layered structure with intralayer sp^2 hybridization and interlayer van der Waals interactions. The discovery of atomically thin graphene layers of graphite brought the most exciting and fruitful periods of scientific and technological research. Graphene is the basic structural element of all graphitic materials, including 0D fullerenes, 1D carbon nanotubes, and 2D graphene (see Figure 1.1). It fills the bridge between the 3D materials and 1D carbon nanotubes.

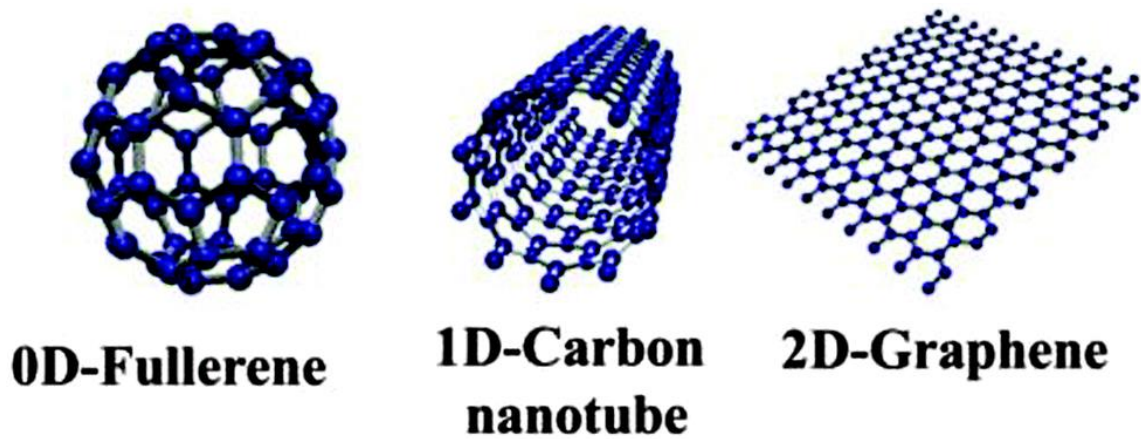


Figure 1.1 Schematic illustration of the 0D (fullerene), 1D (carbon nanotube) and 2D (graphene) nanostructure of carbon-based materials [1].

Graphene is a two-dimensional nanomaterial made of one-atom-thick planar sheet of hexagonally arranged carbon atoms in sp^2 hybridization. For a long time, it was believed to be thermodynamically unstable and presumed not to exist as a free-standing material [2]. The reasoning behind this statement relies on the fact that both finite temperature and quantum fluctuation conspire to destroy the perfect 2D structure. This idea continued until 2004 when a group of researchers in Manchester and Chernogolovka [3] employed a surprisingly simple approach to prepare graphene using an adhesive scotch tape, which led to the 2010 Nobel prize in physics for “groundbreaking experiments regarding the two-dimensional material graphene”. Such a “kindergartner” approach can provide high-quality graphene with sizes in hundreds of microns. Furthermore, two-dimensional crystals of other materials such as hexagonal boron nitride, transition metal dichalcogenides were also obtained by this technique.

The relatively simple preparation method led to a huge increase of interest since research groups all over the world were able to produce and investigate graphene samples with ease. Since then, the research of graphene including controlling of the graphene layers on substrates, functionalizing graphene and exploring the applications of graphene has grown exponentially. This intense interest is also reflected by the number of publications related to graphene research as depicted in Figure 1.2.

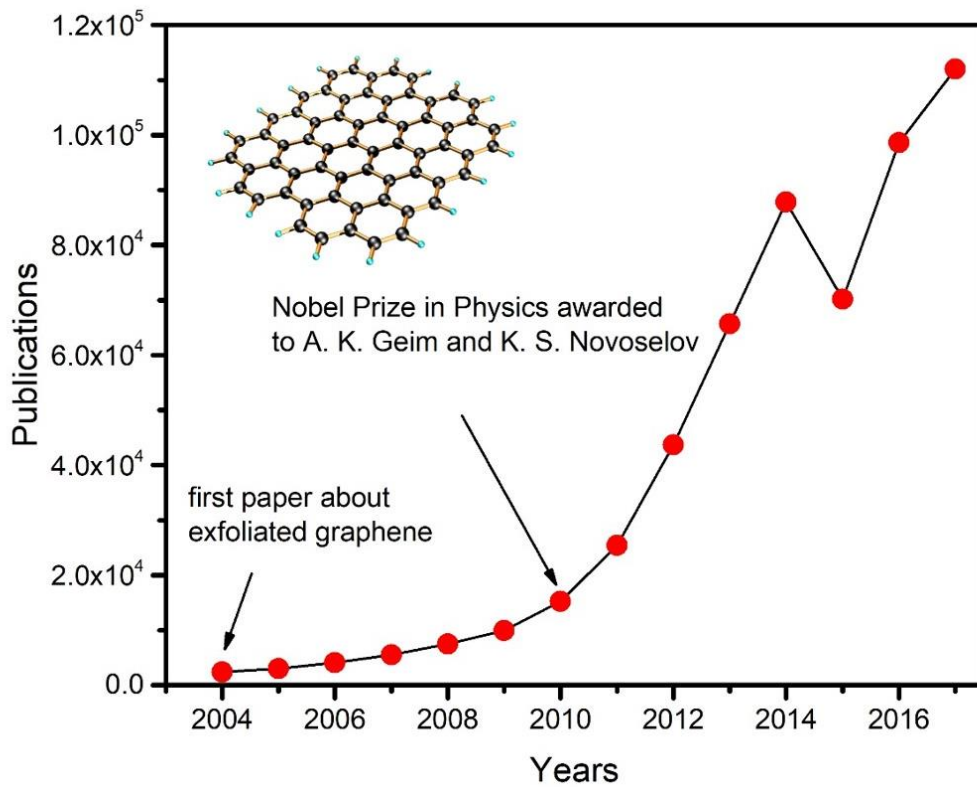


Figure 1.2 Number of publications (article, proceeding paper, review or letter) related to graphene per year. Source: Thomas Reuters Web of Science, as 12.31.2017.

1.2 Band structure of graphene

Electronic energy band structure of graphene was first studied theoretically by Wallace using the tight binding method in 1947 [4]. He explained the behavior as a semimetal due to the lack of an energy gap between the valence and conduction bands and vanishing density of states at the point where the conduction and valence bands touch at the Brillouin zone corners.

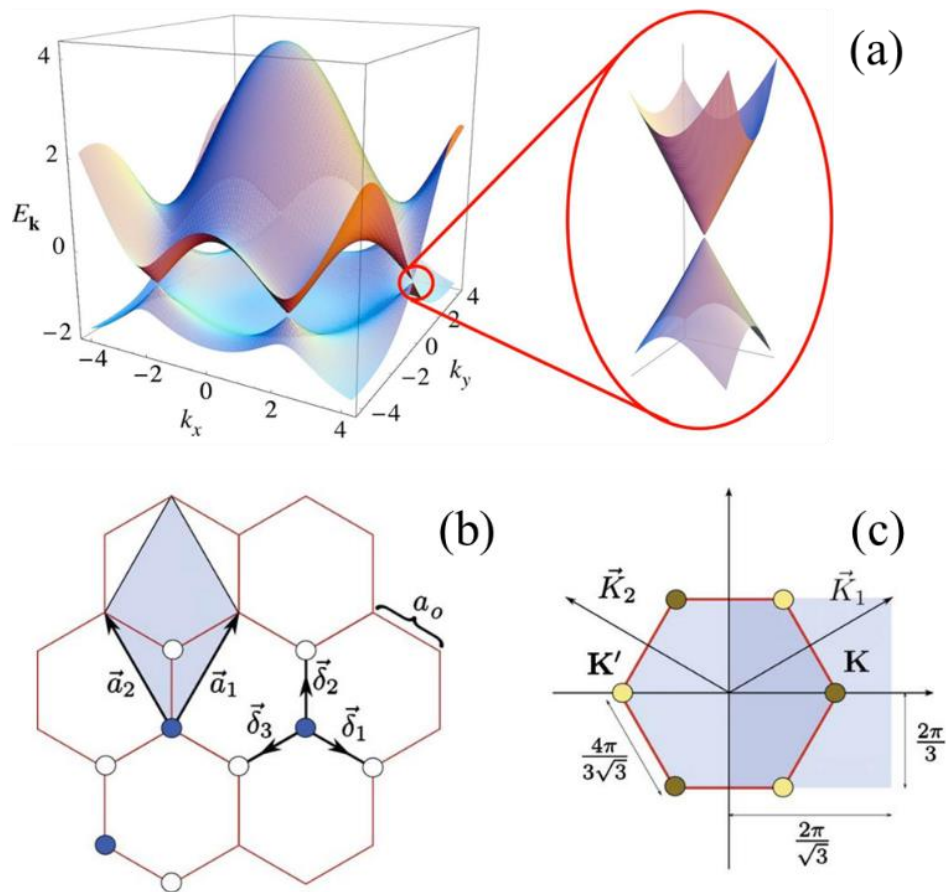


Figure 1.3 (a) Left: the band structure of graphene in the honeycomb lattice. Right: zoom-in of the energy bands close to one of the Dirac points [5]. (b) The hexagonal lattice of graphene, with the nearest neighbor δ_i and the primitive, a_i vectors depicted. The area of

the primitive cell is $A_c = 3\sqrt{3}a_0^2/2 \approx 5.1 \text{ \AA}^2$ and $a_0 \approx 1.42 \text{ \AA}$. (c) The Brillouin zone of graphene, with the Dirac points K and K' indicated.

The touched point is known as Dirac point as shown in Figure 1.3 (a). For undoped graphene, Fermi level lies exactly at the Dirac point thus making graphene a zero-band-gap semiconductor. This unique band structure gives the carriers a constant Fermi velocity and allows graphene to be easily tuned from electron-like to hole-like via an external gate. The hexagonal arrangement of carbon atoms in graphene and the corresponding hexagonal Brillouin zone are shown in Figure 1.3 (b), (c).

As shown in Figure 1.3, the structure of graphene can be seen as a triangular lattice with a basis of two atoms per unit cell, the lattice vectors can be written as

$$\mathbf{a}_1 = \frac{a}{2}(3, \sqrt{3}), \quad \mathbf{a}_2 = \frac{a}{2}(3, -\sqrt{3}),$$

where $a \approx 1.42 \text{ \AA}$ is the carbon-carbon distance. The reciprocal-lattice vectors are given by

$$\mathbf{b}_1 = \frac{2\pi}{3a}(1, \sqrt{3}), \quad \mathbf{b}_2 = \frac{2\pi}{3a}(1, -\sqrt{3}),$$

The positions of Dirac points in momentum space are given by

$$K = \frac{2\pi}{3a}, \frac{2\pi}{3\sqrt{3}a}, \quad K' = \frac{2\pi}{3a}, -\frac{2\pi}{3\sqrt{3}a},$$

The three nearest-neighbor vectors in real space are given by

$$\boldsymbol{\delta}_1 = \frac{a}{2}(1, \sqrt{3}), \quad \boldsymbol{\delta}_2 = \frac{a}{2}(1, -\sqrt{3}), \quad \boldsymbol{\delta}_3 = -a(1, 0)$$

while the six second-nearest neighbors are located at $\boldsymbol{\delta}'_1 = \pm\mathbf{a}_1$, $\boldsymbol{\delta}'_2 = \pm\mathbf{a}_2$, $\boldsymbol{\delta}'_3 = \pm(\mathbf{a}_2 - \mathbf{a}_1)$.

Considering that electrons can hop to both nearest- and next-nearest-neighbor atoms, the tight-binding Hamiltonian for electrons in graphene has the form

$$H = -t \sum_{\langle i,j \rangle, \sigma} (a_{\sigma,i}^\dagger b_{\sigma,j} + \text{H. c.}) - t' \sum_{\langle\langle i,j \rangle\rangle, \sigma} (a_{\sigma,i}^\dagger a_{\sigma,j} + b_{\sigma,i}^\dagger b_{\sigma,j} + \text{H. c.}),$$

where $a_{\sigma,i}$ ($a_{\sigma,i}^\dagger$) annihilates (creates) an electron with spin σ ($\sigma = \uparrow, \downarrow$) on site R_i on sublattice A (an equivalent definition is used for sublattice B), t (≈ 2.8 eV) is the nearest-neighbor hopping energy (hopping between different sublattices), and t' is the next nearest-neighbor hopping energy (hopping in the same sublattice). The energy bands derived from this Hamiltonian have the form [4]

$$E_{\pm}(k) = \pm t \sqrt{3 + f(k)} - t' f(k),$$

$$f(k) = 2 \cos(\sqrt{3}k_y a) + 4 \cos\left(\frac{\sqrt{3}}{2}k_y a\right) + \cos\left(\frac{3}{2}k_x a\right),$$

where the plus sign applies to the upper (π^*) and the minus sign the lower (π) band. It is clear that the spectrum is symmetric around zero energy if $t' = 0$. For finite values of t' , the electron-hole symmetry is broken and the π and π^* bands become asymmetric. Figure 1.3 (a) shows a zoom in of the band structure close to one of the Dirac points. This dispersion can be obtained by expanding the full band structure, $E_{\pm}(k)$, close to the K (or K') vector, as $k = K + q$, with $|q| \ll |K|$

$$E_{\pm}(q) \approx \pm v_F |q| + O\left[\left(\frac{q}{K}\right)^2\right],$$

where q is the momentum measured relatively to the Dirac points and v_F is the Fermi velocity given by $v_F = 3ta/2$, with a value $v_F \approx 1 \times 10^6$ m/s. This approximation leads

to the situation that charge carriers close to the Dirac points possess the same energy dependence on their momentum as relativistic massless Dirac particles.

The absence of a band gap in the energy dispersion of graphene implies that the conduction in this material cannot be simply switched on or off by means of a gate voltage which acts on the position of the Fermi level, limiting the use of graphene in conventional transistor applications. Indeed, even when the Fermi level in graphene devices is at $E = 0$, the current in graphene is far from being completely pinched-off. However, the gapless energy dispersion of graphene is a consequence of the assumption that the electron onsite energy between the A and B sublattice carbon atoms are equal. Whenever they are not equal, a band gap opens in the energy spectrum of graphene.

1.3 Properties and potential applications of graphene

In a perfect graphene sheet, there are two carbon atoms per unit cell in graphene, every carbon atom has four valence electrons with three of them are used for chemical bonds (σ bonds). The bonding energy of one C-C bond in graphene amount to 4.93eV [6]. The remaining 2p orbitals on each carbon atoms, which are perpendicular to the graphene planar structure form highly delocalized π bonds. There are two such electrons in one-unit cell corresponding to two π bands, π and π^* , with π corresponding to valence band and π^* corresponding to conduction band.

These strong σ bonds are responsible for extraordinary mechanical properties of graphene. The experimentally determined values of the second-order and third-order elastic stiffnesses for monolayer graphene are $E^{2D} = 340 \pm 50 \text{ Nm}^{-1}$ and $D^{2D} = -690 \pm 120 \text{ Nm}^{-1}$, respectively. The intrinsic strength is $\sigma_{\text{int}}^{2D} = 42 \pm 4 \text{ Nm}^{-1}$. These correspond to Young's

modulus of $E = 1.0 \pm 0.1$ TPa and a third-order elastic stiffness of $D = -2.0 \pm 0.4$ TPa, assuming an effective graphene thickness of 0.335 nm [7]. Apart from this, graphene is unbelievably light, weighing about only 0.77 mg/m². According to 2010 Nobel physics announcement which illustrates that 1 m² of graphene hammock would support a 4 kg cat, but would weigh only as much as one of the cat's whiskers.

Besides its remarkable mechanical properties, graphene also possesses extraordinary electronic properties. Due to the zero band gap feature, the charge carriers in graphene have very small effective mass so that carrier mobilities are as high as up to 200,000 cm²V⁻¹s⁻¹ at a carrier density of 10¹² cm⁻² [8]. The highest measured mobilities exceed 40000 cm²V⁻¹s⁻¹, even at room temperature and under ambient condition [3, 9-11]. Furthermore, graphene is an ultra-wide-band optical material that interacts strongly with the light of a wide range of wavelengths. Graphene absorbs 2.3% of light in the visible to infrared region. This absorption coefficient is one to three orders of magnitude higher than those of conventional semiconductor materials.

The strong and anisotropic bonding and the low mass of the carbon atoms give graphene and related materials unique thermal properties. The thermal conductivity of graphene was reported in the range 3000-5000 Wm⁻¹K⁻¹ [7, 12]. High in-plane thermal conductivity is due to covalent sp² bonding between carbon atoms, whereas out-of-plane heat flow is limited by weak van der Waals coupling. Heat flow in graphene or graphene composites could also be tunable through a variety of means, including phonon scattering by substrates, edges, or interfaces [13]. The unusual thermal properties of graphene stem from its 2D nature, forming a rich playground for new discoveries of heat-flow physics and potentially leading to novel thermal management applications.

Table 1. Properties of graphene

Property	Value	Comparison with other materials	Ref.
Breaking strength	42 Nm ⁻¹	More than 100 times great than steel	[7]
Elastic limit	~20%		[14]
Carrier mobility at RT	200,000 cm ² V ⁻¹ s ⁻¹	More than 100 times higher than Si	[15]
Thermal conductivity	~5000 Wm ⁻¹ K ⁻¹	More than 10 times higher than Cu	[7, 12]
Max. current density	>108 Acm ⁻¹	~100 times larger than Cu	[16]
Optical absorption coefficient	2.3%	~50 times higher than GaAs	[17-18]

The properties of graphene suggest that various applications are possible. For example, several layer thick graphene films are transparent, electrically conductive and flexible. Therefore, flexible transparent electrode applications including touch screens [19] and solar cells [20-22] have been extensively studied. Single and multilayer graphene films also offer the potential for significant weight reduction in lithium-ion batteries for next-generation power systems, including microbatteries [23]. These batteries use graphene on the surface of anode. Defects in the graphene sheet provide pathways for the lithium-ions to attach to the anode substrate. The time needed to recharge a battery using the graphene anode is much shorter than with conventional lithium-ion batteries. Due to the high surface area to mass ratio of graphene, another potential application is in the conductive plates of supercapacitors [24]. Such graphene-based supercapacitors are an exciting prospect as they could contribute to green energy solutions by use in electric cars, trains and perhaps airplanes.

As high-performance sensors, graphene has been widely researched as an ideal material. Because of the planar consistent arrangement of atoms in a graphene sheet, every

atom within the sheet is exposed to the surrounding environment. This allows graphene to effectively detect changes in its surroundings at micrometer dimensions, providing a high degree of sensitivity. Graphene is also able to detect individual events on a molecular level. For example, it has been used in diagnostics for detection of glucose [25], cholesterol [26], hemoglobin [27] and cancer cells [28].

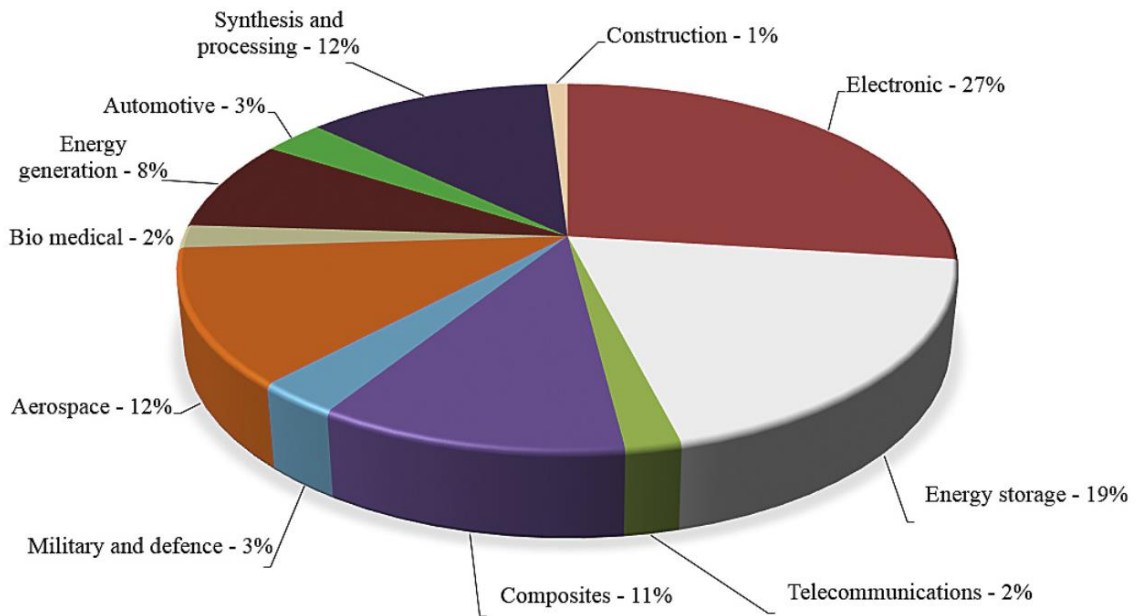


Figure 1.4 Industrial applications of graphene-based materials [29].

Figure 1.4 shows the industrial oriented applications of graphene, where energy-related applications and electronic application occupy the highest percentages, whereas composites represent 11% of application usages [29]. While graphene has tremendous potential in novel applications, many challenges must be overcome to ensure commercial and technological success; from cost-effective large-scale fabrication to controlling and understanding the dependence of its electronic properties on extrinsic factors.

1.4 Synthesis of graphene

Many efforts have been made in the preparation of graphene via a number of physical and chemical methods. Some of these methods provide high-quality graphene and have opened up new possible routes to address the challenges in preparation and molecular engineering of high-quality processable graphene cost-effectively in large-scale. Researchers are considering two primary methods for the synthesis of graphene: a top-down (TD) and a bottom-up (BU) approach. TD synthesis is analogous to cutting down a tree and chiseling a statue from the tree trunk (Figure 1.5). In TD process, graphene or modified graphene sheets are produced by separation/exfoliation of graphite or graphite derivatives such as graphite oxide and graphite fluoride. Conversely, BU approach is done by starting with smaller entities such as carbon atoms and building them up to larger functional constructs such as graphene films.

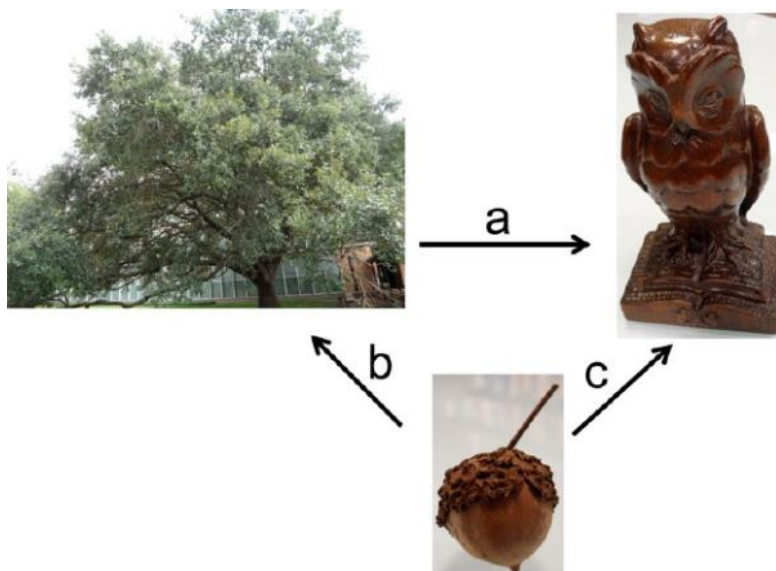


Figure 1.5 TD and BU synthesis compared (not to scale). (a) TD synthesis showing a wooden statue of an owl made from a tree. (b) BU synthesis where a tree is derived from

an acorn. (c) BU synthesis where a seed might be programmed, via DNA, to directly form a wooden statue [30].

Various techniques such as mechanical cleaving (exfoliation) [3], chemical exfoliation [31], wet chemical synthesis [32], and the chemical vapor deposition (CVD) have been established for graphene synthesis [33]. Some other new techniques have also been reported including unzipping of nanotubes [34-36] and microwave synthesis [37]. An overview of graphene synthesis techniques is shown in the flowchart in Figure 1.6.

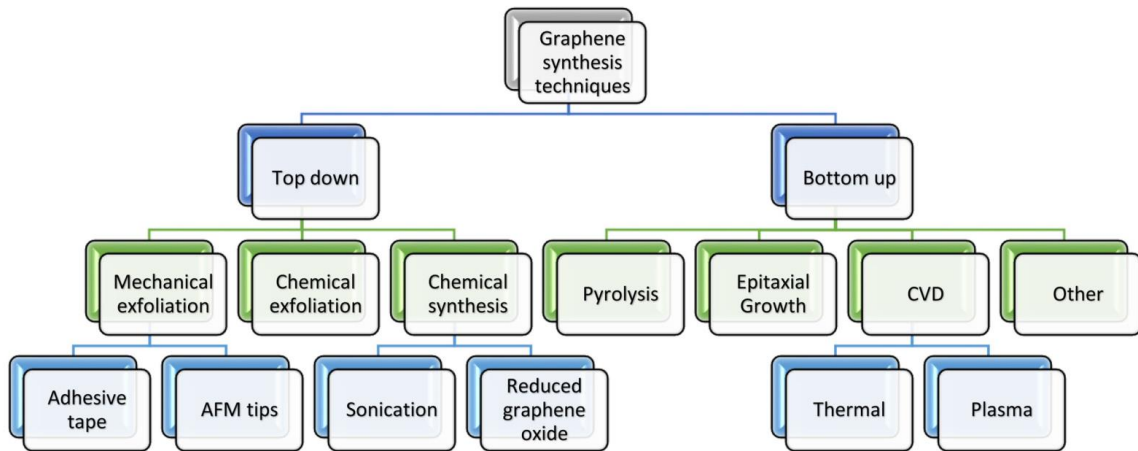


Figure 1.6 A process flow chart of Graphene synthesis [38].

1.4.1 Mechanical exfoliation

Mechanical exfoliation of graphene was the initial technique used to synthesize high-quality monolayers of graphene flakes on preferred substrates [3]. This is a top-down technique in nanotechnology, by which a longitudinal or transverse stress is created on the surface of the layered structure materials. Layers in bulk highly ordered pyrolytic graphite (HOPG) are stacked together by weak van der Waals energy. The interlayer distance and bond energy are 3.34 Å and 2 eV/nm², respectively. About 300 nN/μm² external force is

required to remove monolayer graphene flake from graphite [39]. Such small force can be easily managed by adhesive tape. After repeating the peeling process, graphene from adhesive tape can be transferred to SiO₂/Si substrate by gentle pressing [3, 40] (Figure 1.7). This peeling/exfoliation can be done using a variety of agents like scotch tape [3], ultrasonication [41], electric field [42] and even by transfer printing technique [43-44] etc. Graphene flakes synthesized by mechanical exfoliation are usually characterized by optical microscopy, Raman spectroscopy, and AFM. This method spread quickly in the scientific community since it is comparatively easy to learn and no expensive equipment is required. However, the graphene flakes obtained by this method are very small and limited to the order of few μm . This technique is not scalable to industrial level but serves as a good technique to obtain high-quality graphene samples with almost no defects for research purposes.

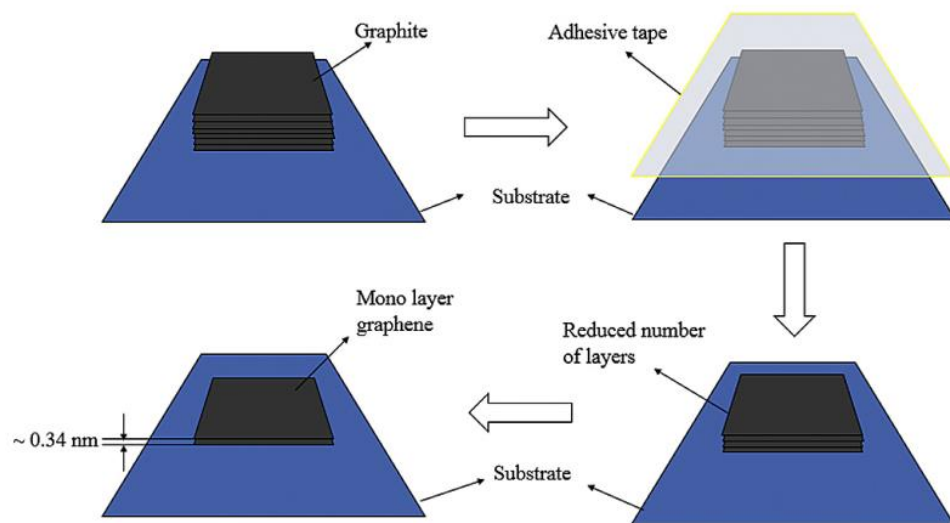


Figure 1.7 Schematic representation of sequential steps followed to exfoliate graphene layers using the scotch tape method [45].

1.4.2 Liquid phase exfoliation

Liquid phase exfoliation of graphite into single and few layer graphene with the aid of sonication is another promising method for graphene synthesis. Typically, graphite can be exfoliated into graphene in a solvent having a surface tension (γ) close to 40 mJm^{-2} [46-48], which favors an increase in the total area of graphite crystallites. Solvents like N-methyl-2-pyrrolidone (NMP) [49], ortho-dichlorobenzene [50], and dimethylformamide (DMF) [51] are commonly chosen as a dispersion media. When subjected to sonication, graphite flakes split into individual graphene sheets that are stabilized in the liquid media. During the ultrasound treatment, flakes of different size and thickness of graphene can be produced. Then centrifugation can be used to separate graphene sheets from unexfoliated material.

Liquid phase exfoliation graphene can be used for many applications: graphene dispersions as optical limiters, films of graphene flakes as transparent conductors or sensors, and exfoliated graphene as mechanical reinforcement for polymer-based composites [46]. Recently, researchers have used this method to remove chemical vapor deposition grown graphene samples from the substrates and to obtain graphene in solution form, which in turn can make the post-processing easier for practical applications [52]. The processable form of graphene dispersion can be applied to different substrates using spin coating, spray coating or ink-jet printing [53-54].

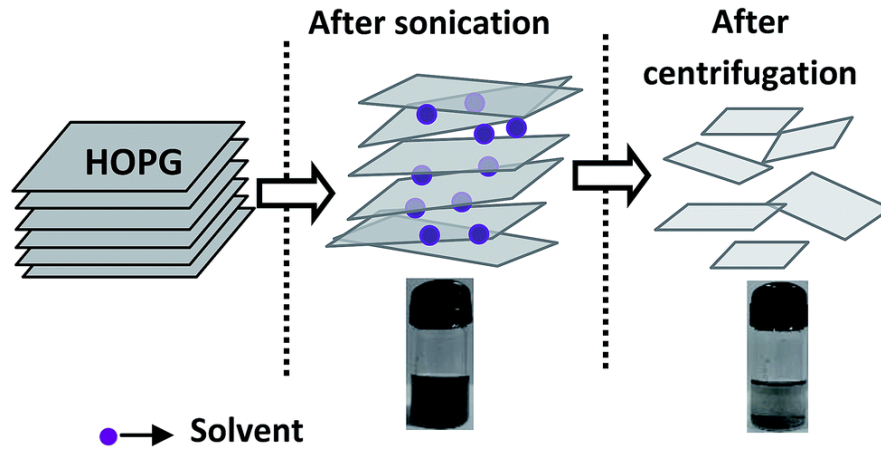


Figure 1.8 Schematic diagram of liquid phase exfoliation method [55].

1.4.3 Epitaxial growth

Epitaxial thermal growth on a single crystalline silicon carbide (SiC) surface is one of the most praised methods of graphene synthesis. SiC as polar material has two inequivalent terminations, called the Si-face, corresponding to the (0001) polar surface, and the C face (000 $\bar{1}$). For both the Si-face and C face, the growth mechanism of graphene is driven by the same physical process: sublimation of Si at elevated temperatures at a rate much faster than C due to its higher vapor pressure [56]. The remaining C forms a graphene film on the surface. The surface reconstructions and growth kinetics for Si and C faces are different, resulting in different graphene growth rates, growth morphologies and electronic properties [57]. The main advantages of epitaxial graphene on SiC are that no transfer is needed for device processing and the size of the graphene sheet can be as large as the substrate, which is another benefit for device processing. However, this method is too expensive due to the high cost of SiC substrate and the necessity of high processing temperature. Moreover, compared to graphene via exfoliation method, more fragile and

defective graphene tends to be formed due to the large lattice mismatch between SiC and graphene during epitaxial method.

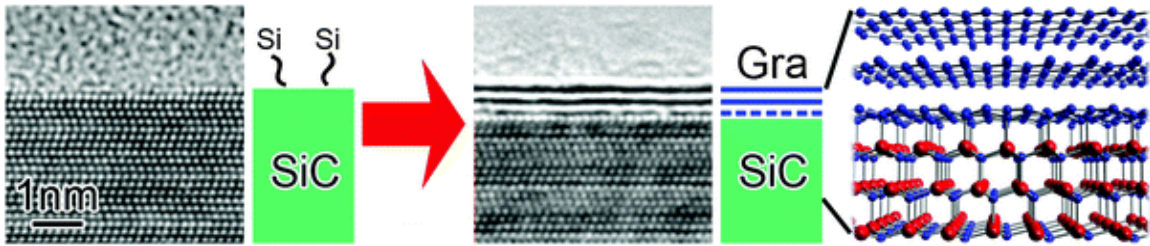


Figure 1.9 Basics of epitaxial thermal growth graphene on SiC substrate [58].

1.4.4 Chemically derived graphene

Chemical conversion of graphite to graphene oxide has emerged to be a viable route to afford graphene-based single sheets in considerable quantities. This is one of the low-cost methods for the large-scale production of graphene. Graphene oxide is usually synthesized through the oxidation of graphite using oxidants including concentrated sulfuric acid, nitric acid and potassium permanganate based on Hummers method [59]. The graphene oxide films produced are thicker than the pristine graphene sheets of 0.34 nm thick due to the displacement of sp^3 hybridized atoms. The chemical reduction of graphene oxide sheets can be performed in the presence of different reducing agents, including hydrazine [60], sodium borohydride [61], hydroquinone [62] and ascorbic acid [63]. During the reduction process, the oxygen atoms can be removed, which results in less hydrophilic nature of graphene oxide sheets [64]. The thermal reduction is another way of reducing graphene oxide that involves the removal of oxide functional groups by heat treatment [65].

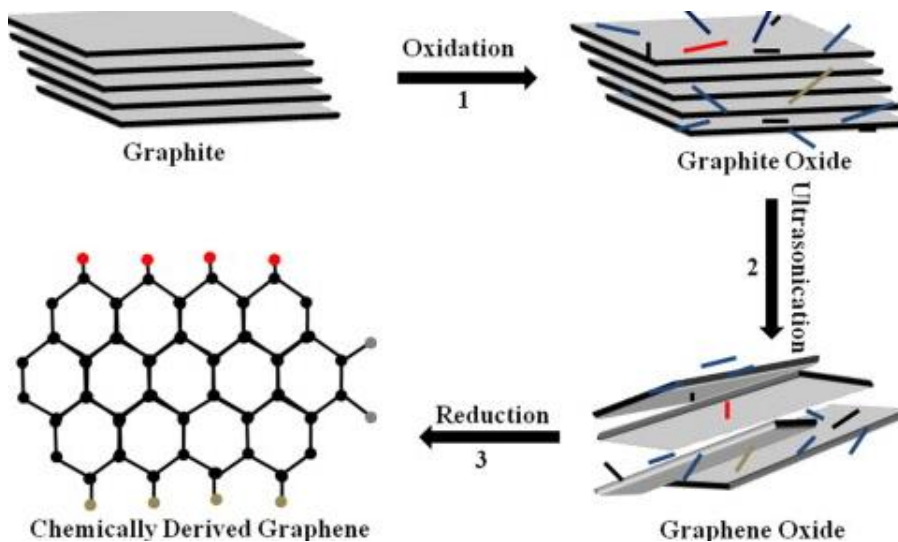


Figure 1.10 Scheme showing the chemical route for the synthesis of graphene [66].

Graphene produced by this method is suitable for a variety of applications such as paper-like materials, polymer composites, energy storage materials, and transparent conductive electrodes, etc. However, this chemical reduction of graphene contains some amount of functionalization groups such as oxygen, hydroxyl groups, epoxy groups etc. Further study must be done to understand the structure and reaction mechanisms to produce high quality chemically derived graphene.

There are several other methods to synthesize graphene such as electron beam irradiation of PMMA nanofibers [67], arc discharge of graphite [68], thermal fusion of PAHs [69], conversion of nanodiamond [70] and so on. The results show that these techniques are capable of synthesizing high-quality monolayer graphene sheet. However, more effort is still needed to improve on the graphene synthesis techniques in term of scalability and cost-effectiveness in order for them to be used in different industrial applications.

CHAPTER 02

CHEMICAL VAPOR DEPOSITION (CVD) OF GRAPHENE: SYNTHESIS AND CHARACTERIZATION

2.1 CVD of graphene

As we discussed in chapter 01, a number of methods have been established for graphene synthesis. Among these methods, CVD is regarded as having the most potent way to synthesize high quality, large-scale and single layer graphene [71]. CVD graphene was first reported in 2008 and 2009, using Ni and Cu as substrates, which was then followed by an explosion of research activities. High temperature decomposition of various hydrocarbon sources by CVD method to produce thin, graphitic layers on transition metal surfaces and metal carbides have been studied for over 60 years. Generally, CVD of graphene involves the thermal decomposition of a hydrocarbon source on a heated substrate, it is created in two steps, the precursor pyrolysis of a material to form carbon and the formation of the carbon structure of graphene using the disassociated carbon atoms on heated substrates. Transition metals are the most widely used substrates in graphene synthesis [33].

During the CVD reaction, the metal substrate works as a catalyst to lower the energy barrier of the reaction and determines the graphene deposition mechanism. Table 2 lists the solubility of carbon in various metal substrates and the corresponding growth mechanism.

For metals with high carbon solubility such as Ni and Fe, the carbon will diffuse into the substrate at high temperature. As the substrate cooling, the dissolved carbon will segregate to the surface to form graphene sheets [72-74] as shown in Figure 2.1 (a). In the case of metals having low carbon solubility such as Cu, carbon atoms will nucleate and laterally expand around the nucleus to form graphene domains with the decomposition of hydrocarbon catalyzed by the substrates at high temperature (Figure 2.1 (b)).

Table 2. Carbon solubility and the growth mechanism on typical metals for CVD graphene [33].

Metal (bulk)	Carbon solubility at 1000 C (at.%)	Primary growth mechanism
Copper (Cu)	0.04	Surface deposition/penetration
Cobalt (Co)	3.41	Segregation
Platinum (Pt)	1.76	Segregation/surface deposition
Nickel (Ni)	2.03	Segregation/surface deposition
Palladium (Pd)	5.98	Segregation
Iron (Fe)	7.89	Segregation
Germanium (Ge)	0.00	Surface deposition

The growth process will terminate when the substrates are fully covered by the graphene layer, which is referred as a “self-limited surface deposition” growth mechanism [75]. The thermodynamic parameters such as the temperature and pressure of the system also influence the mechanism of graphene growth, whether the process is performed at atmospheric pressure, low pressure (LP) (0.1-1 Torr), or under ultrahigh vacuum (UHV) condition (10^{-4} - 10^{-6} Torr), the kinetics of the growth phenomenon are different, leading to a variation in the uniformity of the graphene overlayer area.

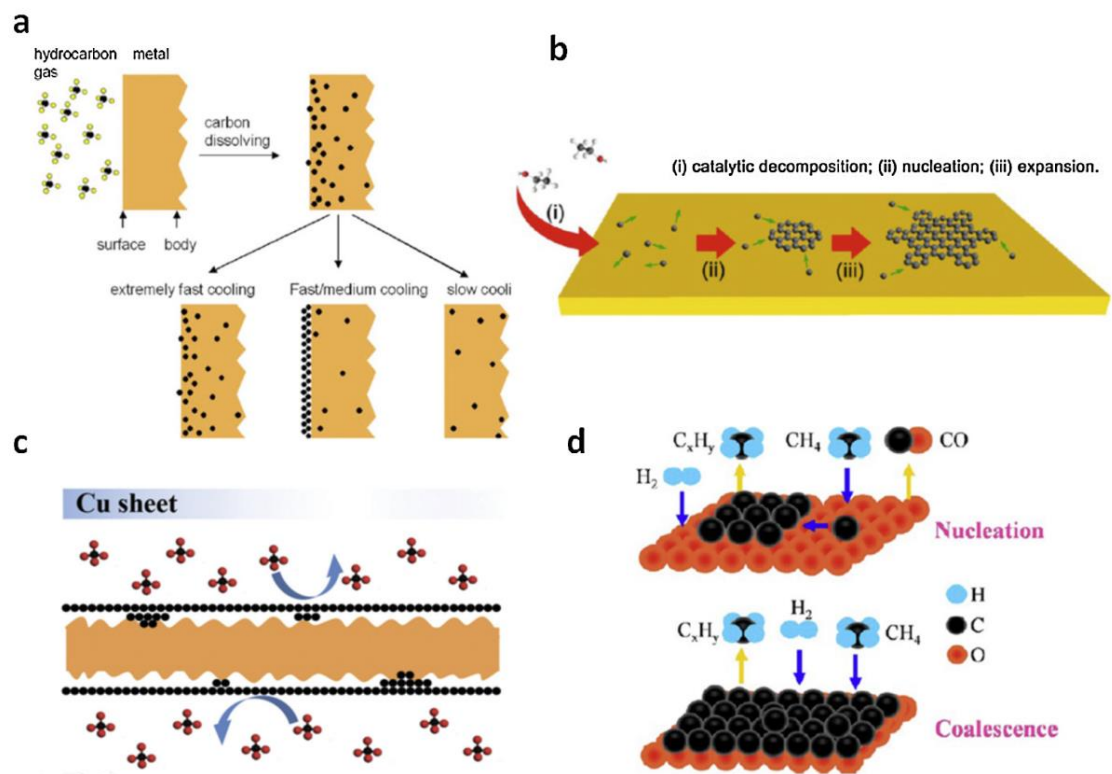


Figure 2.1 Schematics of CVD graphene grown on (a) metals with high carbon solubility, (b) Cu foil, (c) Cu enclosure, and (d) sapphire [33].

There are also variety of precursors for CVD graphene, including solid, liquid and gas precursor, have been used for carbon source molecules to synthesize graphene film. Hydrocarbon gas precursors, such as methane (CH_4), ethylene (C_2H_4) [76-80] and acetylene (C_2H_2) [81] are among the most popular carbon sources used for synthesizing graphene. CH_4 is the most commonly used precursor among these hydrocarbon gas, as it is comparatively stable at high temperature around 1000 °C. Figure 2.2 shows the schematic diagram of the CVD system, it is composed a gas delivery system with mass flow controllers to control the flow rates of gases, high temperature tube furnace, pressure

control system with butterfly valve and gas removal system to remove the byproducts during the graphene growth.

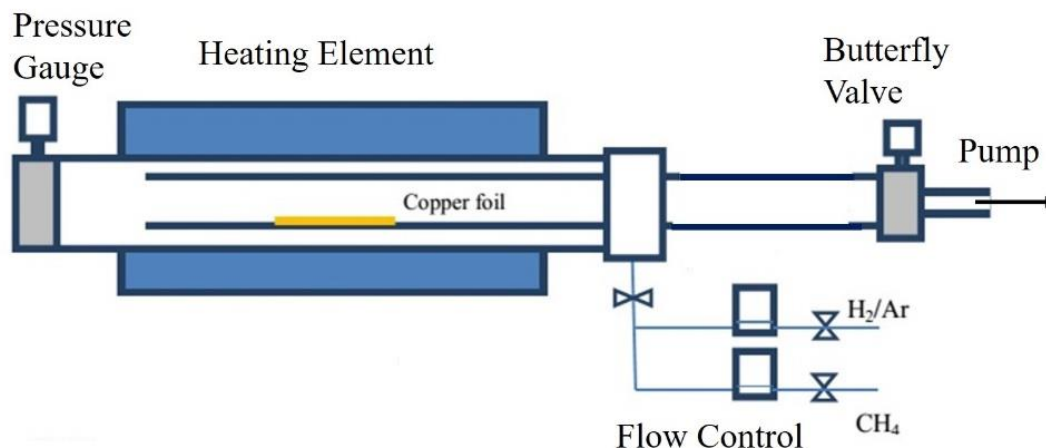


Figure 2.2 Schematic diagram of CVD growth of graphene.

During the synthesis, copper foils were cut into pieces of $\sim 2 \times 2 \text{ cm}^2$, and cleaned with acetone and isopropanol in a sonicator for 5 minutes. Then the cleaned copper substrates were placed inside a quartz crucible and loaded into the inner tube placed inside the furnace. This dual tube design helps to maintain the undisturbed temperature profile along the reactor area. It is achieved by preheating the precursors before it enters in the reaction zone. Prior to heating up, the system was pumped to a base pressure of $\sim 10 \text{ mTorr}$ with the butterfly valve fully open. Temperature of the furnace was ramped from room temperature to $1000 \text{ }^\circ\text{C}$ at a rate of $25 \text{ }^\circ\text{C}/\text{min}$ with a flow rate of 5 sccm (standard cubic centimeters per minute) Argon and Hydrogen mixture (Ar 60%, H₂ 40%). The Cu foils were annealed for 20-30 min to initiate Cu grain growth, remove residual copper oxide, and to smoothen the surface. Subsequently, methane was introduced at a rate of 20 sccm to the system and the synthesis time was maintained ~ 20 minutes. The samples were then

cooled down to room temperature at a rate of 25 °C/min under a flow rate of 5 sccm Ar and H₂ mixture. Complete temperature profile during the graphene growth process is shown in Figure 2.3.

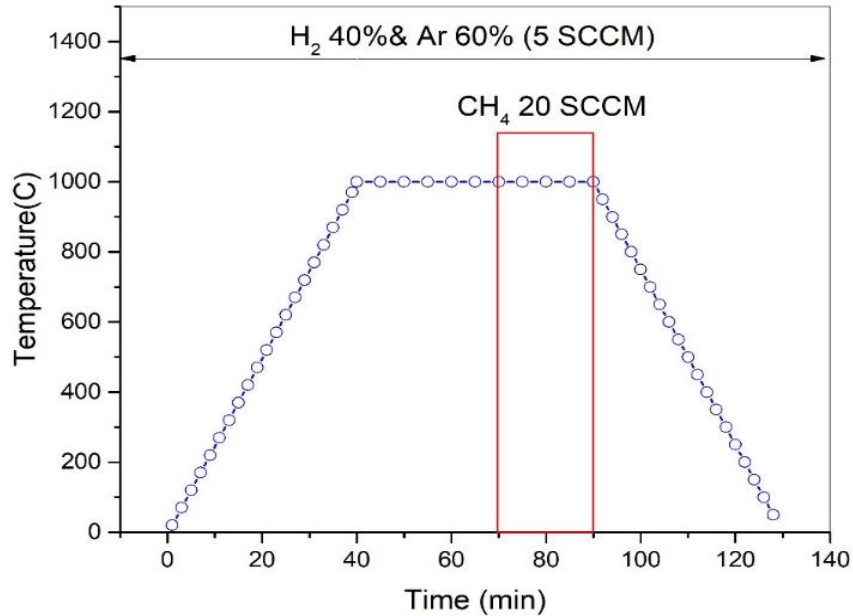


Figure 2.3 Temperature curve during the CVD growth of graphene.

2.2 Transfer of graphene films

Utilization of CVD-grown graphene for further characterization and applications in nanoelectronic or photovoltaics requires a transfer process to remove the graphene from the catalytic metal substrates and transfer it onto an arbitrary substrate. This transfer process needs to be efficient, low cost, scalable and high quality. It also has to address two problems: the separation of the graphene layer from the metal substrate and the protection of the graphene integrity after the separation. Various methods have been developed to transfer graphene onto different substrates [82]. Currently, the most commonly used

transfer method relies on Polymethylmethacrylate (PMMA) or Polydimethylsiloxane (PDMS) [83-87]. A schematic diagram of the transfer process is shown in Figure 2.4. During the transfer process, graphene was first coated by PMMA or PDMS. After removing the metal layers by metal etchant (such as iron chloride, hydrochloric acid, nitric acid, iron nitrate and copper chloride) the polymer coated graphene can be scooped onto an arbitrary substrate. The film is cleaned by deionized (DI) water and then transferred onto a target substrate. After evaporating the water vapor away, polymer was removed by acetone, leaving a graphene film on top of the target substrate. However, this method is not suitable for the transfer of large-area graphene film as it can easily introduce contamination, cracks and tears during the transfer process [83, 86], and requires greater handling skills.

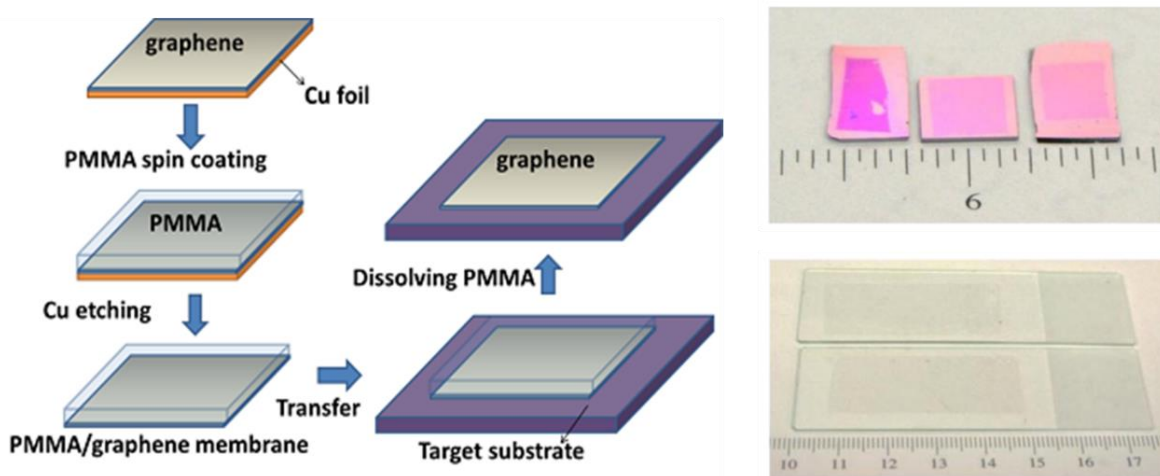


Figure 2.4 Schematic diagram of graphene transferring on target substrate.

Recently, some non-polymer based graphene transfer methods have been discovered for reliable ultraclean graphene transfer, such as Metal-assisted graphene transfer [88], Small molecules assisted graphene transfer [89], Hexan-assisted graphene transfer [90], and Static charge based graphene transfer [91]. Each graphene transfer

method possesses unique characteristics and the selection of a transfer technique largely depends on the applications. For example, the roll-to-roll transfer method is suitable for mass production of graphene on flexible substrates, while the support-free technique is superior for the study of graphene chemistry. Graphene transfer will remain the only alternative for a number of applications, especially those involving plastic substrates, which cannot withstand the high temperatures required for the CVD growth of graphene.

2.3 Plasma Enhanced CVD of graphene

Plasma Enhanced chemical vapor deposition (PECVD) has been widely used to produce carbon related materials based on its prominent and additional advantages such as lower reaction temperature, higher growth selectivity, purer atmosphere, and better control in nanostructure ordering/patterning. Synthesis of graphene directly on insulating substrates such as SiO₂/Si or glass using PECVD is helpful to overcome the quality degradation and additional defects caused by the transfer process. The plasma can provide a rich chemical environment, including a mixture of radicals, molecules and ions from a simple hydrogen-hydrocarbon feedstock, allowing for lower deposition temperatures and faster growth than thermal CVD method. However, the quality of PECVD graphene to date has not been significantly better than that of thermal CVD [92-93].

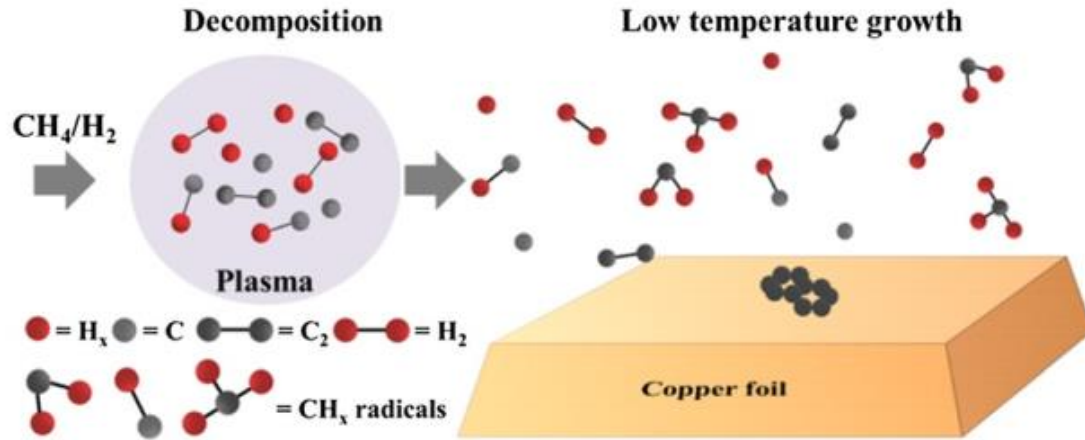


Figure 2.5 Mechanism of growth of graphene that involves decomposition of CH_4/H_2 mixed plasma.

Figure 2.5 shows the graphene growth mechanism that involves the decomposition of CH_4 and H_2 mixed plasma and CH_x radicals. The gaseous CH_x radicals recombined with each other after they had floated for a certain distance, and the metastable carbon atoms and molecules formed a sp^2 structure on the substrate. It is crucial to select a proper carbon source and control well its ratio in the feedstock gases aiming at high quality growth. The feedstock gas flow rate and plasma energy are two competing factors: most PECVD processes are conducted at a low pressure to achieve a relatively long mean free path of electrons while the massive production of graphene calls for a large volume of gas input. Recently, PECVD employing a variety of plasma sources such as Microwave Plasma [93], Radio frequency Plasma [94], and DC discharges [95] with different reactor configurations have been successfully demonstrated for graphene growth.

2.4 Electrical properties of materials

2.4.1 The electrical conductivity

Materials are classified based on their electrical properties as conductors, semiconductors, and insulators. New to this group is superconductors. When presented with a new material, two things are important to know: how the electrons in the material respond to electrical forces and how the atoms respond to mechanical forces. The first one is defined in terms of ease of charge flow through it called electrical conductivity. Charge that flows comprised of either electrons, ions, charged holes and their combinations. When an electric potential V is applied across a material, a current of magnitude I flows. In most conductors, the current I is proportional to V , according to Ohm's Law:

$$V = RI$$

where R is the electrical resistance, it depends on the intrinsic ρ of the materials and on the geometry (length l and the cross-sectional area A through which the current passes).

$$R = \frac{\rho l}{A}$$

The electrical conductivity (the ability of a substance to conduct an electric current) is the inverse of the resistivity: $\sigma = \frac{1}{\rho}$.

Since the electric field intensity in the material is $E = V/L$, Ohm's Law can be rewritten in terms of current density $J = I/A$ as:

$$J = \sigma E$$

It is also expressed as $J = nqv_d$, where n is the charge carrier density and q is the electron charge. The velocity with which the charges move in the direction of the applied field is known as the drift velocity v_d . When there is less scattering in a material, the charge carriers will travel farther with the same electric field. This ratio is defined as the mobility, $\mu = v_d/E$. One can then express the conductivity of a material in terms of its mobility by:

$$\sigma = nq\mu$$

From the equation, the electrical conductivity of a material can be controlled by (i) controlling number of charge carriers, n or (ii) controlling the mobility of the carriers, μ . Electrical conductivity varies between different materials by over 27 orders of magnitude, the greatest variation of any physical property.

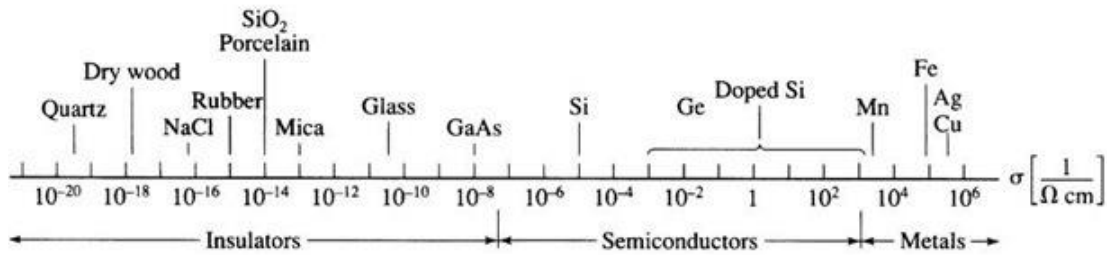


Figure 2.6 Room-temperature conductivity of various materials. (Superconductors, having conductivities many orders of magnitude larger than copper, near 0 K, are not shown. The conductivity of semiconductors varies substantially with temperature and purity.)

2.4.2 Four probe resistivity for sheet resistance

The concept of sheet resistance is used to characterize both wafers as thin doped layers since it is typically easier to measure the sheet resistance rather than the resistivity of the material. The sheet resistance of a layer with resistivity, ρ , and thickness, t , is given by their ratio:

$$R_s = \frac{\rho}{t}$$

Note that the dimension of sheet resistance is also measured in ohms, but is often denoted by Ωsq^{-1} (ohms per square) to make it distinguishable from the resistance itself. The origin of this peculiar unit name relies on the fact that a square sheet with a sheet resistance of $1 \Omega sq^{-1}$ would have an equivalent resistance, regardless of its dimensions. Therefore, the resistance of a rectangular rod of length l and cross section $A = wt$ can be written as $R = \rho l/A$, which immediately simplifies to $R = R_s$ for the special case of square lamella with sides $l = w$ (see Figure 2.7) [96].

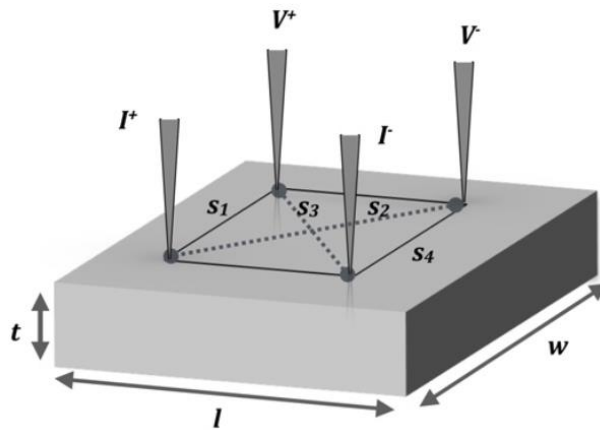


Figure 2.7 Schematic of a square 4P probe configuration with $s_1 = s_4 = s$ and $s_2 = s_3 = \sqrt{2}s$.

For small thin films characterization, the square arrangement is better than a straight line since it has the advantage of requiring a smaller area (the maximum probe spacing is only $\sqrt{2}s$ against the $3s$ for the collinear arrangement) and reveals a slightly higher sensitivity. Table 3 summarized all relations for the infinite 3D and 2D systems with both in-line and square arrangements of four probes.

Table 3. Bulk resistivity or sheet resistance R_{sh} for the case of linear and square arrangements of four probes on a semi-infinite 3D material, infinite 2D sheet, and 1D wire.

Sample shape	4P in-line	4P square
3D bulk	$2\pi s \frac{V}{I}$	$\frac{2\pi s}{2 - \sqrt{2}} \frac{V}{I}$
2D sheet	$\frac{\pi}{\ln 2} \frac{V}{I}$	$\frac{2\pi}{\ln 2} \frac{V}{I}$
1D wire	$\frac{\Sigma V}{s I}$	–

2.4.3 Hall mobility measurements

Hall effect measurements have been valuable tools for material characterization since Edwin Hall discovered the phenomenon in 1879. The Hall effect can be observed when the combination of a magnetic field B through a sample and a current I along the length of the sample create an electrical current perpendicular to both the magnetic field and the current, which in turn creates a transverse voltage (known as the Hall voltage V_H) perpendicular to both the field and the current.

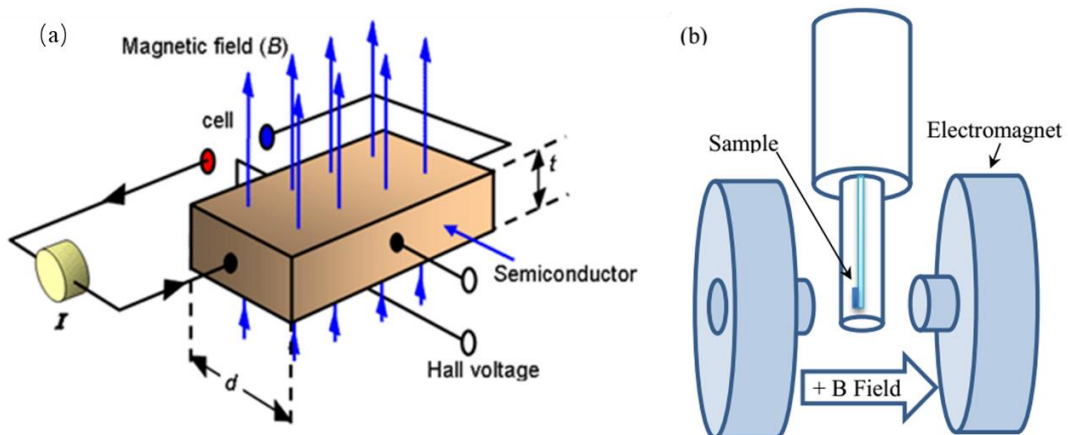


Figure 2.8 Schematic of (a) Van der Pauw configuration used in the determination of the Hall voltage V_H . (b) the sample placed in the magnetic field.

To derive the Hall voltage, we first note that the magnetic force exerted on the carriers has magnitude qv_dB , where v_d is the drift speed of the carrier. In equilibrium, this force is balanced by the electric force qE_H , where E_H is the magnitude of the electric field due to the charge separation. Therefore, we can obtain:

$$qv_dB = qE_H \quad (1)$$

$E_H = v_dB = V_H/d$, where d is the width of the conductor.

Thus, the measured Hall voltage gives a value for the drift speed of the charge carriers if d and B are known. We can obtain the charge carrier density n by measuring the current:

$$I = v_d n q A \quad (2)$$

where A is the cross-sectional area of the conductor and can write as $A = td$ (t is the thickness of the conductor). Substituting equation (2) into equation (1), we obtained:

$$V_H = IBd/nqA = IB/nqt = R_H IB/t \quad (3)$$

where $R_H = 1/nq$ is the Hall coefficient.

Substituting $\sigma = nq\mu$ to equation (3), the Hall mobility can be calculated as:

$$\mu = \sigma R_H = R_H/R_S t \quad (4)$$

By sweeping a perpendicular magnetic field, B , measuring R_H and sheet resistance R_S , one can determine the carrier mobility, μ . This is a technique known as the Hall Effect and is commonly used to characterize conducting samples. We will use this in Chapter 03 and 04 to determine the transport properties for graphene films.

2.4.4 Thermoelectric power

An electron in solids is an elementary particle with a negative charge of e , and carries electric current. Since an enormous number of electrons are at thermal equilibrium in solids, they also carry heat and entropy. Thus in the presence of temperature gradient, they can flow from a hot side to a cold side to cause an electric current. This implies a coupling between thermal and electrical phenomena, which is called thermoelectric effects, including Seebeck effect and Peltier effect. The Seebeck effect is a phenomenon that voltage V is induced in proportion to applied temperature gradient ΔT , expressed as

$$V = S\Delta T \quad (5)$$

where S is called the Seebeck coefficient, also thermoelectric power or thermopower.

Various methods are used in thermoelectrical power measurements such as pulse [97] and AC [98] techniques. Here we introduced a simple, inexpensive method to obtain the thermopower in the range 4 K to 700 K using ordinary thermocouple systems.

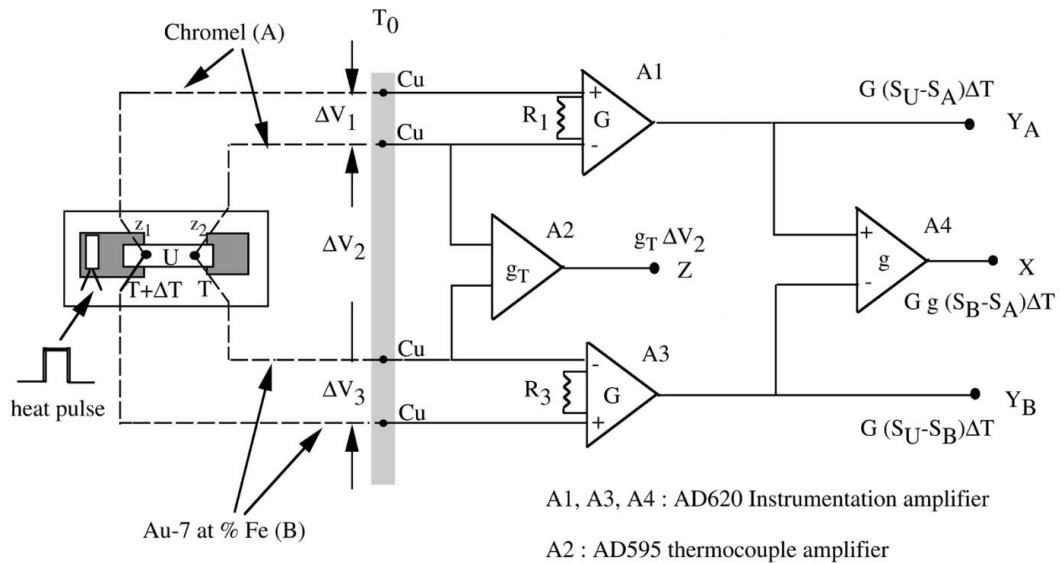


Figure 2.9 Schematic diagram of the circuit [99].

Figure 2.9 shows the three thermoelectrical voltages ΔV_1 , ΔV_2 , and ΔV_3 which determine the absolute thermoelectrical power of the sample, S_U and the average sample temperature T [99]. Using the definition of the thermoelectrical power S , the voltage difference ΔV developed between position z_1 and z_2 in a homogeneous material with temperature profile $T(z)$ is given by:

$$\Delta V = V(z_2) - V(z_1) = \int_{z_1}^{z_2} S \frac{dT}{dz} dz \quad (6)$$

where $V(z_1)$ and $V(z_2)$ are the voltages at z_1 and z_2 respectively. The voltages in Figure 2.9 can therefore be written as:

$$\begin{aligned} \Delta V_1 &= \int_{T_0}^T S_A dT + \int_T^{T+\Delta T} S_U dT + \int_{T+\Delta T}^{T_0} S_A dT \\ &= \int_T^{T+\Delta T} (S_U - S_A) dT = (S_U - S_A) \Delta T \end{aligned} \quad (7)$$

$$\begin{aligned} \Delta V_2 &= \int_{T_0}^T S_A dT + \int_T^{T_0} S_B dT \\ &= \int_T^{T_0} (S_B - S_A) dT = V_{BA}(T) \end{aligned} \quad (8)$$

$$\begin{aligned} \Delta V_3 &= \int_{T_0}^T S_B dT + \int_T^{T+\Delta T} S_U dT + \int_{T+\Delta T}^{T_0} S_B dT \\ &= \int_T^{T+\Delta T} (S_U - S_B) dT = (S_U - S_B) \Delta T \end{aligned} \quad (9)$$

The subscripts in equation (7) - (9) refer to either the thermocouple wire materials (A and B) or the sample (U). T_0 is approximately the room temperature which refers to the temperature of thermocouple junctions of A and B with copper leads that transfer the signals from this reservoir to the instrumentation amplifiers. The thermopower for a variety

of samples includes graphene films can be measured by this approach between a wide range of temperature.

2.5 Characterization of graphene

2.5.1 Raman Spectroscopy

Raman spectroscopy is a spectroscopic technique based on inelastic scattering of monochromatic light, usually from a laser source. When light is scattering by matter, almost all of the scattering is an elastic process (Rayleigh scattering) and there is no change in energy. Unlike Rayleigh scattering, Raman scattering is inelastic. It means that the frequency of photons in laser source changes upon interaction with a sample. Photons are absorbed by the sample and then reemitted. Frequency of the reemitted photons is shifted up or down in comparison with original monochromatic frequency, which is called the Raman effect.

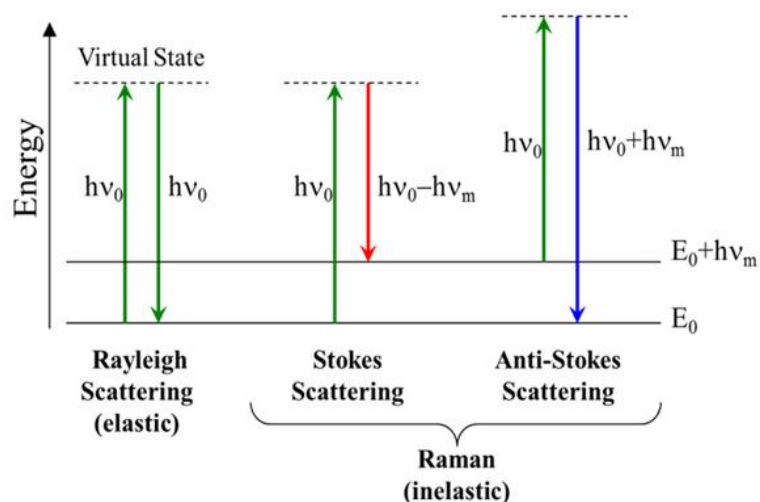


Figure 2.10 The energy diagram of Rayleigh and Raman scattering.

The Jablonski diagram illustrates the energy transitions involved in Rayleigh and Raman scattering [100]. In both cases, the molecule makes a transition from the ground electronic state to a virtual state. Raman scattering is different in that the molecule either emits a photon of lower frequency (Stokes) or higher frequency (anti-Stokes) than that of the incident photon. Stokes transitions have a greater probability of occurring than anti-Stokes transitions since molecules are predominantly in the ground state at room temperature. The frequency difference, $\Delta \nu$, is known as the Raman shift and is what appears on the abscissa of a Raman spectrum. This shift provides information about vibrational, rotational and other low frequency transitions in molecules. Raman spectroscopy can be used to study solid, liquid and gaseous samples to identify unknown substance and polymorphs, track changes in molecular structures and crystallinity, evaluate the magnitude of residual stress and assess the direction of orientation of molecules.

Raman spectroscopy has played an important role in the structural characterization of graphitic materials [101], and has also become a powerful tool for understanding the behavior of electrons and phonons in graphene [102]. Generally, the Stokes phonon energy shift in graphene caused by laser excitation creates two main peaks in the Raman spectroscopy: G (1580 cm^{-1}), a primary in-plane vibrational mode involving the sp^2 hybridized carbon atoms that comprise the graphene sheet. 2D or G' (2690 cm^{-1}), a second-order overtone of the D band corresponding the result of a two phonon lattice vibrational process. The D (1350 cm^{-1}) band is known as the disorder band or the defect band and it represents a ring breathing mode from sp^2 carbon rings, although to be active the ring must be adjacent to a graphene edge or a defect. The band is typically not visible in high quality graphene because of crystal symmetries [103] as shown in Figure 2.11 (a).

The G band position is highly sensitive to strain effects and indicates the number of layers in the graphene sample [104]. The position of G band moves to lower frequencies, as the number of layers increases, as shown in Figure 2.11 (b). However, no major change is observed in spectral shape. In addition, the G band is sensitive to doping and both the line width and frequency of this peak can be employed to examine the doping level. Unlike the G band position method, the 2D band method for the determination of the layer number depends on the band position and band shape. Figure 2.11 (c) shows the differences between the layers in this band. The distinct band shape differences allow the 2D band to be effective in differentiating the layer thickness between single and multilayer graphene of less than four layers. Moreover, high quality defect free single layer graphene can also be identified by analyzing the peak intensity of the 2D and G bands. The ratio I_{2D}/I_G of these bands will be seen to be equal to 2. This ratio, lack of a D band and a sharp symmetric 2D is a confirmation for a high quality defect-free graphene sample.

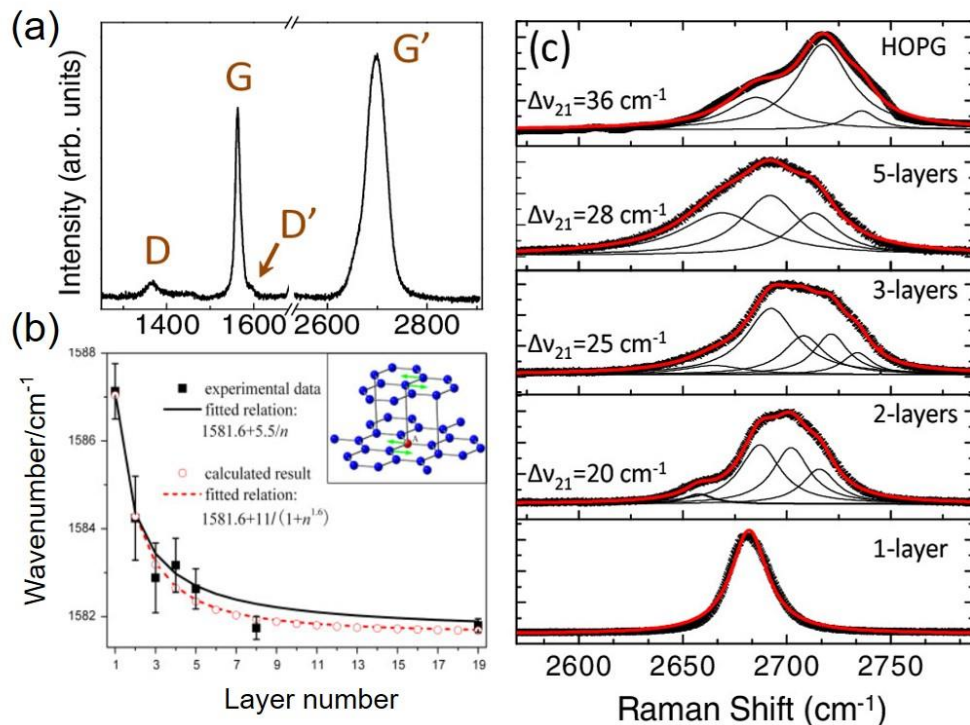


Figure 2.11 (a) Raman spectra of graphene, (b) The position of G band for different layer number of graphene, (c) 2D band method for the determination of the layer number of graphene [103].

2.5.2 Scanning electron microscope

The Scanning Electron Microscope (SEM) is used for observation of specimen surfaces. When the specimen is irradiated with a fine electron beam (called an electron probe), secondary electrons are emitted from the specimen surface. Topography of the surface can be observed by two-dimensional scanning of the electron probe over the surface and acquisition of an image from the detected secondary electrons.

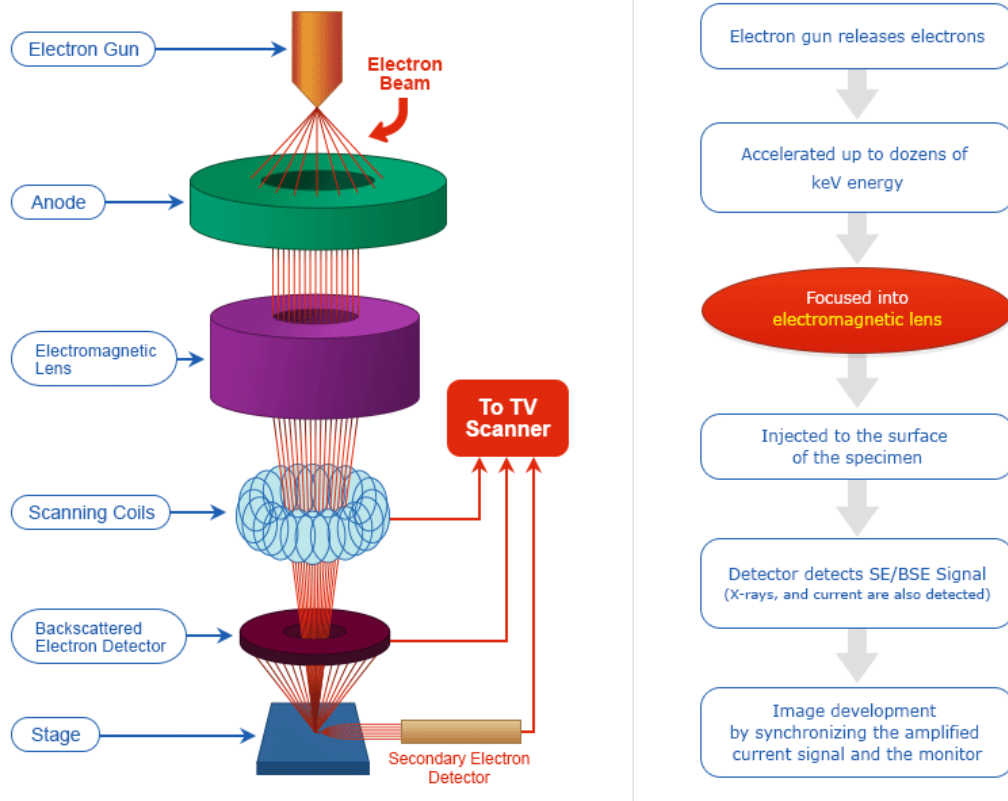


Figure 2.12 Schematic of Scanning Electron Microscope internal components.

As a powerful technique, SEM has been extensively used for imaging new materials, especially at micro and nanoscales. For graphene films, SEM imaging technique is a rapid, non-invasive and effective manner for imaging the morphologies. Particularly, many electronic applications require uniform and defect free graphene in large area, SEM has the advantages in detecting impurities, ruptures, folds, voids, and discontinuities of synthesized or transferred graphene on a variety of substrates as shown in Figure 2.13.

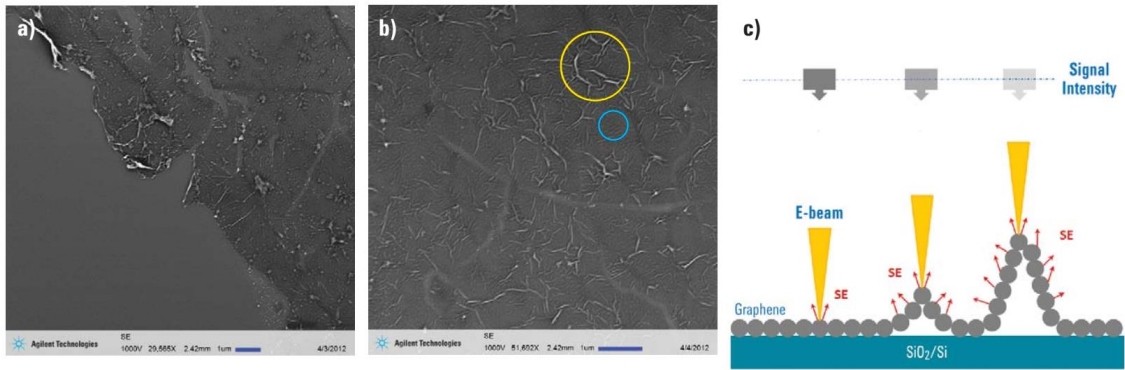


Figure 2.13 (a) A SEM micrograph showing the edge of a transferred graphene sheet on the SiO_2/Si substrate; b) a highly corrugated structure with small and big wrinkles, indicated as the blue circle and yellow circle, respectively; c) a schematic depicting the roughness contrast for a corrugated graphene sheet on the SiO_2/Si substrate [105].

2.5.3 Transmission electron microscopy

Transmission electron microscopy (TEM) is frequently used to image nano size materials to the atomic scale resolution where a transmitted electron beam passes through the ultra-thin sample and reaches to the imaging lenses and detector. When an accelerated beam of electrons impinges upon a sample a rich variety of interactions takes place (Figure 2.14). The versatility of electron microscopy and x-ray microanalysis is derived in large

measure from this variety of interactions that the beam electrons undergo in the specimen. The interactions that occur during the collision of the electron beam and the sample include directly transmitted electrons, backscattered electrons, secondary electrons, coherent elastic scattered electrons, incoherent inelastic electrons, incoherent elastic forward scattered electrons, Auger electrons, phonons, et al. In principle all these products of primary beam interaction can be used to derive information on the nature of the specimen.

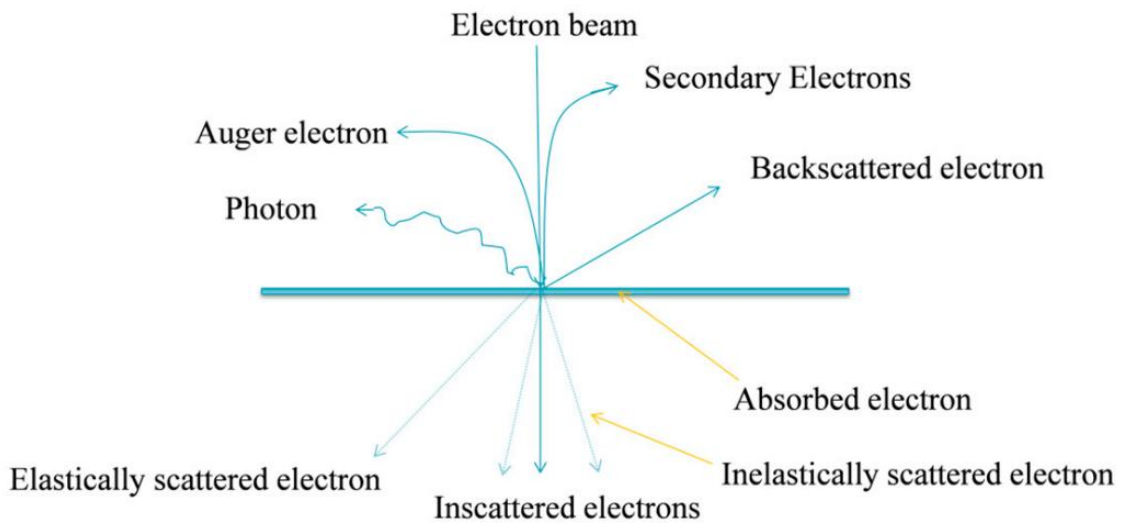


Figure 2.14 Basic principle of Transmission Electron Microscopy (TEM).

TEM has been successfully applied to study adsorbates on graphene and the atomic structure of graphene [106]. High resolution imaging is an extensively used method in TEM to estimate the thickness of graphene flakes exactly. For this purpose, the electron beam is focused on the folding edge of a flake. At the folding edge, the graphene planes become parallel to the electron beam where each plane diffracts the electrons and appears as a dark line in the phase contrast image (see Figure 2.15). This dark lines of the image or minima of the intensity can be counted to obtain the layer number of the graphene flake.

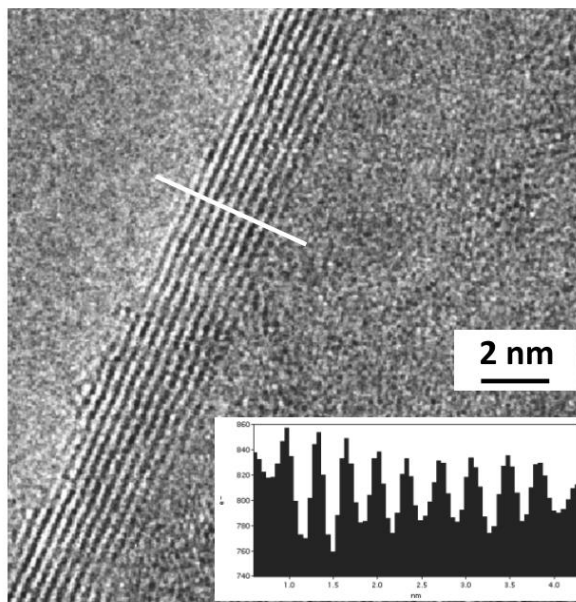


Figure 2.15 A HR-TEM image of a folding edge of graphene flake show dark and bright lines.

2.5.4 X-ray photoelectron spectroscopy

X-ray photoelectron spectroscopy (XPS) is a classical method for the semi-quantitative analysis of surface composition and very crucial for analyzing functionalized graphene sample. It is typically accomplished by exciting the surface of a sample with mono-energetic Al $K\alpha$ x-rays or Mg $K\alpha$ x-rays causing photoelectrons to be emitted from the sample surface. An electron energy analyzer is used to measure the energy of the emitted photoelectrons. From the binding energy and intensity of a photoelectron peak, the elemental identity, chemical state, and quantity of a detected element can be determined. The processes can be summarized in the simplified three step model. In the first step a photon with an energy of $h\nu$ impinges the surface and excites an electron. After the excitation, the electron is transported to the surface. Finally, the electron has to overcome

the vacuum barrier and becomes a free electron, which has a kinetic energy E_{kin} that can be analyzed by energy analyzer. (see Figure 2.16).

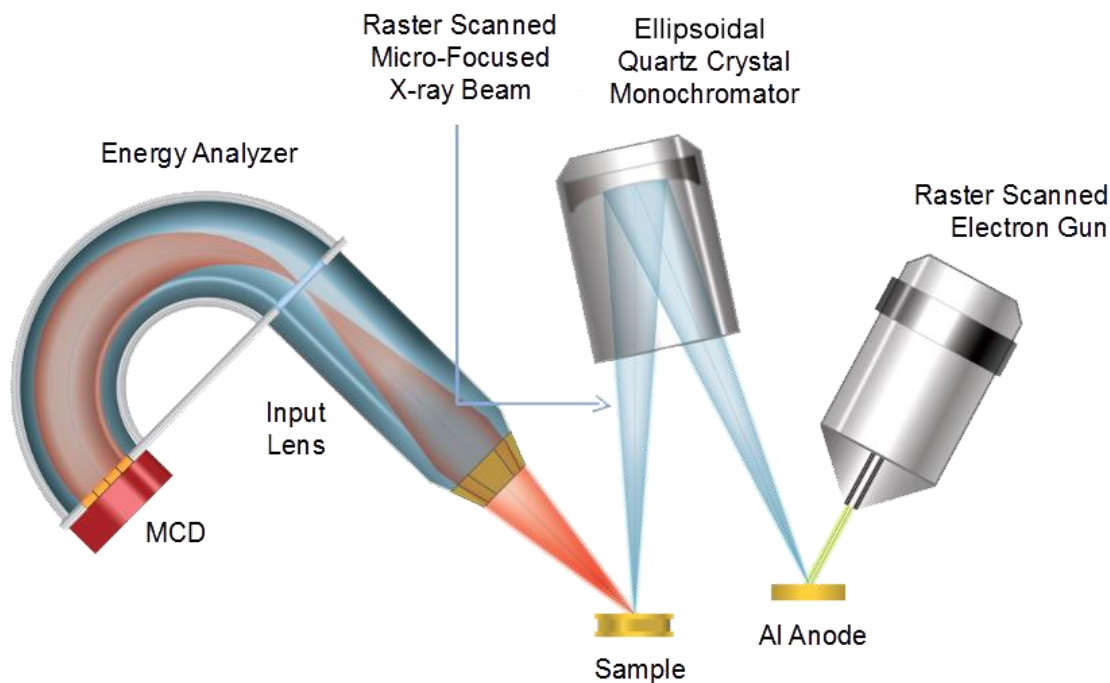


Figure 2.16 Schematic of X-ray photoelectron spectroscopy.

Through the conservation of energy one can convert the kinetic energy scale into a binding energy scale by using the following equation:

$$E_{bin} = E_{photon} - (E_{kin} + \phi)$$

where E_{bin} is the binding energy of the electron, E_{photon} is the energy of the X-ray photons being used, E_{kin} is the kinetic energy of the electron as measured by the instrument and ϕ is the work function dependent on both the spectrometer and the material. The term ϕ is an adjustable instrumental correction factor that accounts for the few eV of kinetic energy given up by the photoelectron as it becomes absorbed by the instrument's detector. It is a constant that rarely needs to be adjusted in practice.

Since the binding energy of a core level electron is influenced by its chemical surrounding, one can use XPS to not only identify different elements due to their specific binding energies but also obtain information about the chemical state the element is in. This is a surface-sensitive quantitative spectroscopic technique that measures the elemental composition of functionalized and doped graphene samples.

CHAPTER 03

FLUORINATION OF GRAPHENE: TRANSPORT PROPERTIES AND BAND GAP FORMATION

3.1 Introduction

Since the first experimental evidence of the electronic properties of graphene in 2004, graphene continues to attract intense interest in both scientific and industrial communities due to its extraordinary properties [3]. It is worth mentioning that graphene itself possesses zero band gap as well as inertness to reaction, which weakens the competitive strength of graphene in the field of semiconductors and sensors. Band gap opening of graphene by functionalizing, doping, and striping would be useful for nanoelectronic devices. Various derivatives by both covalent and noncovalent means have functionalized the surface of graphene in order to tailor its further properties [107-110]. The functionalization not only inherits unique carbon conjugated structures but also brings about a promise to alter the graphene's properties including dispersion, orientation, interaction and electronic properties.

Fluorinated graphene is regarded as the two-dimensional basic structural element which receives much attention in self-cleaning, solid lubricants, super hydrophobic coating and the electrode of electrochemical cell because of its extremely low surface energy, good chemical and thermal stabilities and high electromotive force [111]. It is a stable and wide

band gap nanosheet in which a certain amount of C atoms is covalently bonded to F atoms. Compared with other derivatives, fluorinated graphene shows many unique properties because of the formation of various types of C-F bonds. Because of F atoms has a higher electronegativity (4.0) than C (2.5), H (2.2), and O atoms (3.4), fluorinated graphene show great potential for using as an atomically thin insulator or a tunnel barrier based on the heterostructures [112]. Moreover, fluorinated graphene exhibits several C-F bonding characters from ionic, semi-ionic to covalent bonds controlled by the fluorination conditions [113].

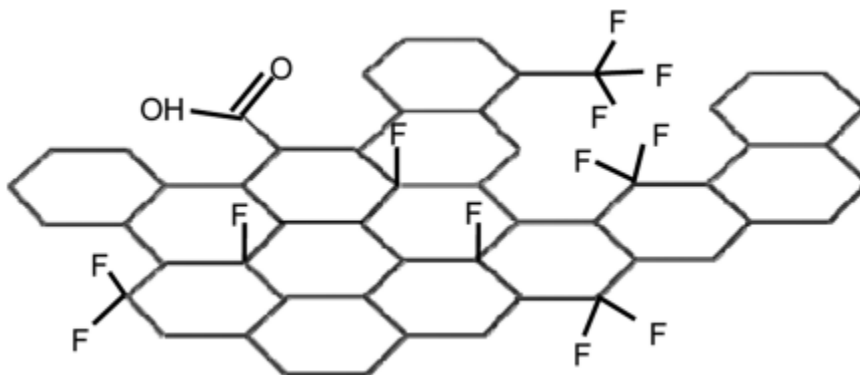


Figure 3.1 Example of chemical bonds in fluorinated graphene.

Many methods for synthesizing fluorinated graphene have been discovered such as direct gas-fluorination [112], plasma fluorination [114-117], hydrothermal fluorination [118], and photochemical/electrochemical synthesis [119-120]. High quality fluorinated graphene offers a great potential for modulating various properties by controlling the microstructures such as layer, size and surface chemistry. In this chapter, we report the *in-situ* monitoring of electrical properties of graphene during plasma induced fluorination followed by *ex-situ* property measurements [121].

3.2 *in-situ* functionalization of graphene

The synthesis and transfer of few layer graphene onto Si/SiO₂ and glass substrates have been described in chapter 02. Having access to large area graphene enables direct measurements of electrical, thermal and magneto transport properties without undergoing any microfabrication processes which can cause contaminations during lithographic processes. Graphene samples were sequentially fluorinated for different fluorine concentrations using a controlled fluorine plasma. This can tune graphene gradually from metal to insulator eventually opening a bandgap. The dc conductivity was measured over a wide range of temperature by standard Van der Pauw technique. This technique clearly identifies the metallic samples, from insulating samples as described in chapter 02. Concomitant measurement of thermoelectric power (S) and mobility (μ) further validates the conductivity measurement results. Figure 3.2 shows the schematic of plasma functionalization setup and graphene sample mounted on the probe. This setup consists of controlled gas delivery system, reaction area, gas removal system etc. CF₄ gas is supplied to the system as fluorine source.

Simultaneous S and R measurements were carried out inside a quartz chamber. The chamber can be evacuated, annealed or, filled with CF₄ for plasma treatment at desired temperatures and pressures as shown in Figure 3.2. The sample was kept away from the center of the plasma to minimize the plasma induced damage to the sample while maintaining the chamber pressure at 5 Torr with 20 W plasma power and 10 sccm gas feed rate.

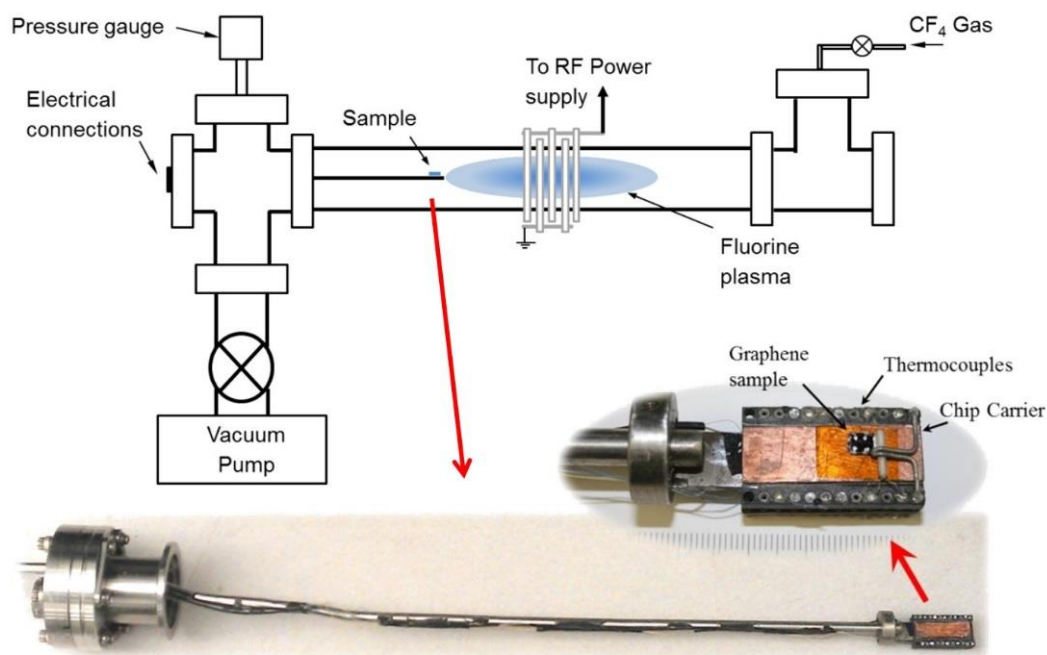


Figure 3.2 Schematic of plasma functionalization setup and graphene sample on chip carrier for *in-situ* measurements.

The graphene sample was mounted on a chip which in turn is attached to a measurement probe contained in a quartz reactor placed inside a tube furnace. Two (Chromel (KP)/Au–7at%Fe (Au: Fe)) thermocouples were mounted on the sample with SPI conductive silver paint and a small resistive heater was placed on one end of the sample. Two extra copper wires were attached as current leads for electrical transport measurements. All four contacts were arranged according to the van der Pauw configuration. Sample was degassed at 500 K by evacuating the reactor using a turbo molecular pump. S and R were recorded simultaneously as a function of time. Applied voltage pulse to the heater creates heat gradient across the sample to measure the S . Heating power is kept well under 10 mW to maintain temperature difference below 1K ($\Delta T < 1$ K) and the typical pulse duration is 3–5 seconds [99]. Raman spectroscopy measurements

were performed under ambient conditions by Invia Renishaw Raman spectrometer with 632 nm excitation wavelength. Low temperature transport measurements of graphene samples were performed using a closed cycled refrigerator (Janis Research Co. CCS-350ST-H) down to 8 K. An electromagnet (LakeShore Model EM4-CV 4-inch gap, Horizontal Field) enclosing the refrigerator column enables perpendicular magnetic field of -1 and +1 Tesla.

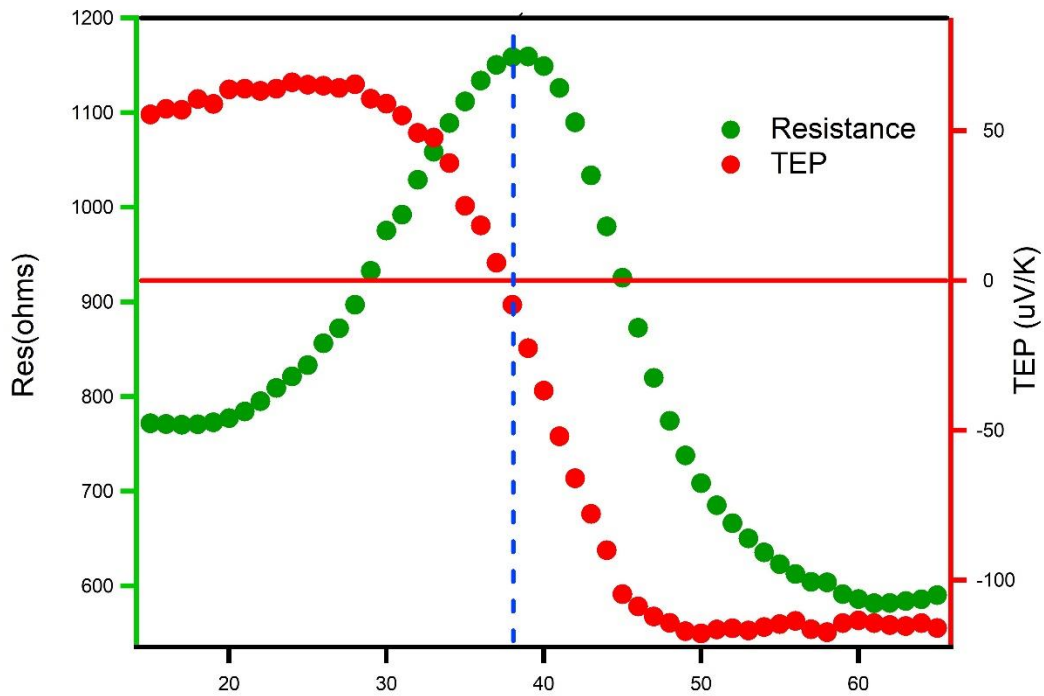


Figure 3.3 Resistance and thermopower of graphene during annealing.

Before the fluorination process, graphene sample was annealed under high vacuum conditions ($\sim 10^{-7}$ Torr) at 500 K for few hours. During annealing, S was seen to gradually undergo a sign change from $\sim +50 \mu\text{V/K}$ to $\sim -60 \mu\text{V/K}$. The positive S is characteristic p-type behavior of air exposed graphene [122] and vacuum degassing causes S to turn negative [123-124]. Concomitantly the initially R value of ~ 700 ohms was seen to

gradually increase and reach a maximum value when $S = 0$ as shown in Figure 3.3. For all investigated samples, graphene becomes n-type after vacuum annealing.

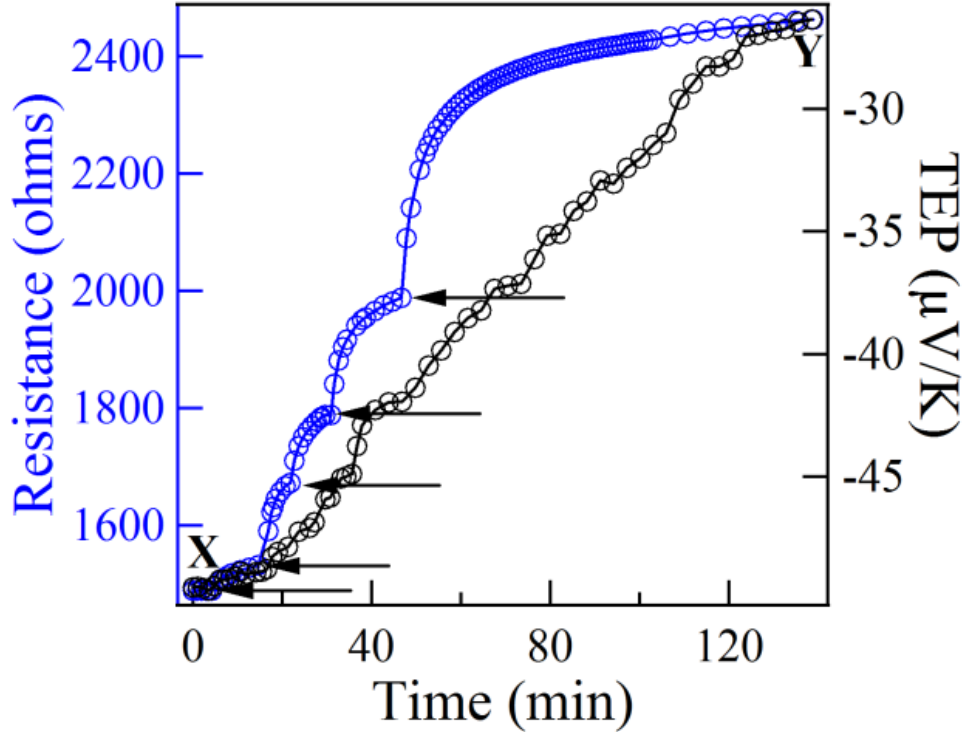


Figure 3.4 Time dependence of the resistance, $R(t)$ and thermopower, $S(t)$ during fluorination. The arrowheads indicate the initiation of plasma.

Figure 3.4 shows the time dependence of R (left axis) and S (right axis) of initially degassed graphene during fluorination. The start and the end of the fluorination process are indicated by “X” and “Y” respectively in the graph. The sample was carefully exposed to the intermittent fluorine plasma for a short period of time (~ 5 s) at each fluorination indicated by arrows. It was clearly found that S gradually start to increase (towards zero) from its negative degassed state. This can be explained by the formation of C–F bonding causing reduction of delocalized electrons in the graphene network. However, this shows

a contrast difference from the hydrogenation process where S immediately turned positive [125]. After R approached the desired final value at “Y”, the temperature dependence of R, S, and mobility (μ) were measured. This process was continued for various degrees of fluorination.

3.3 *ex-situ* characterization of fluorinated graphene

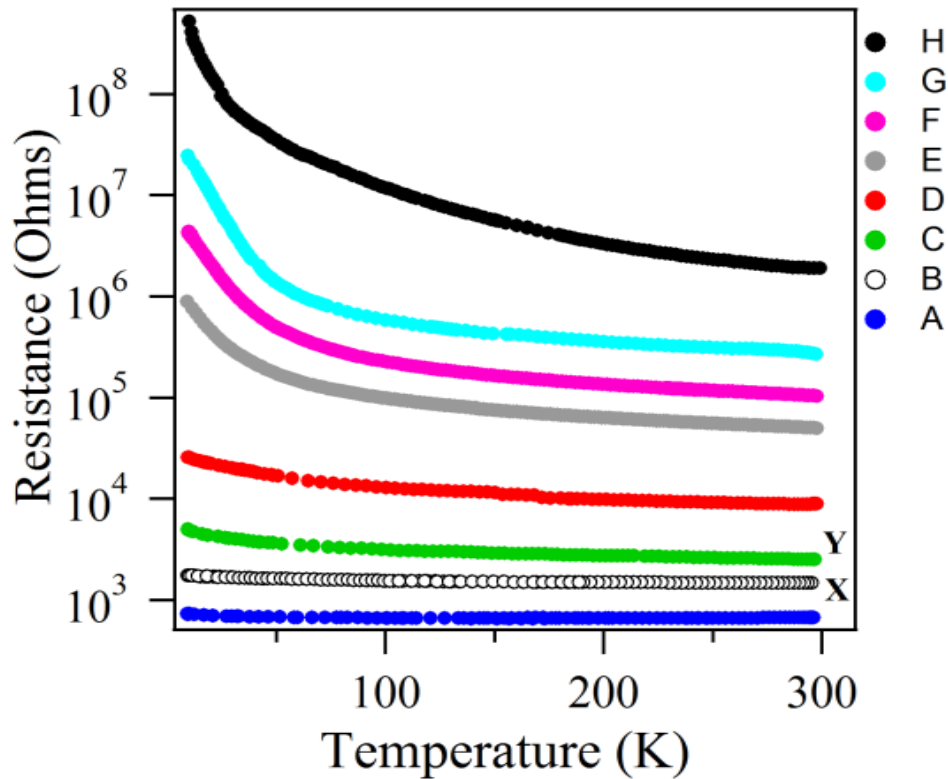


Figure 3.5 Temperature dependence of the four-probe resistance, $R(T)$ of fluorinated graphene samples including the pristine and degassed graphene.

$R(T)$ for all the samples subjected to various degrees of fluorination including the pristine and degassed samples are shown in Figure 3.5. The bottom curve (A) shows the

temperature dependence of R for the pristine sample (before degassing; oxygen/moisture loaded). The curve “B” represents $R(T)$ for graphene after degassing. The fluorination process was repeated until resistance and thermopower were no longer measurable due to limitation in the instruments. The $R(T)$ for graphene after each fluorination process are shown in Figure 3.5 marked from “C” to “H”.

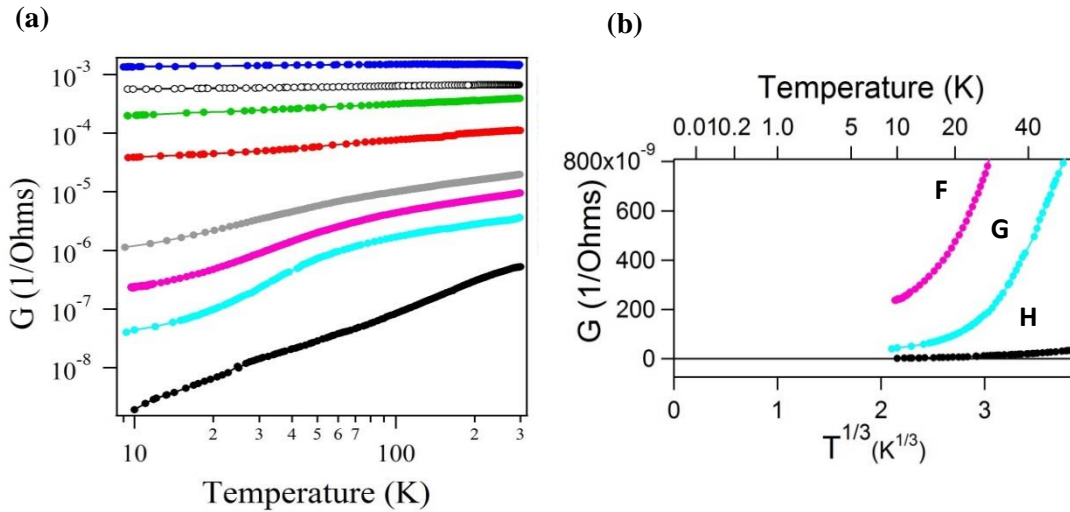


Figure 3.6 (a) G vs T plot for progressively fluorinated graphene samples. (b) G vs $T^{1/3}$ plot for the three curves represented by F, G, and H (only low temperature data is shown).

Figure 3.6 (a) shows the conductivity G ($=1/R$) and temperature in logarithmic scales for pristine, degassed and progressively fluorinated graphene samples. Samples correspond to curves from “A” to “G” remain metallic behavior since G remains nonzero at low temperature, whereas sample represented by curve “H” exhibits insulating behavior as G falls rapidly at low temperature. Furthermore, we plot G vs $T^{1/3}$, in an expanded scale in the vicinity of conductivity, $G = 0$ in Figure 3.6 (b). Conductance curve “G” is believed to remain close to critical behavior as all the samples represented by $G(T)$ curves above it

remain metallic while the sample represented by curve “H” below it does not conduct at low temperature (as conductivity begins to vanish at $T \sim 15$ K) [126-127].

In the 2D weak localization (WL) theory, the temperature dependence of the conductance, $G(T)$ is known to follow logarithmic temperature dependence, $G(T) \sim \ln(T)$. For fluorinated graphene, electrical transport properties are expected to be governed by tunneling via hopping conduction. Hence, we fitted $R(T)$ dependence to the two dimensional variable range hopping (2D-VRH) model, $R = R_0 \exp(T_0/T)^{1/3}$, where $T_0 = 13.8/(k_B N(E_F) \zeta^2)$, $N(E_F)$ is the density of states at the Fermi energy, k_B is the Boltzmann constant and ζ is the localization length [128].

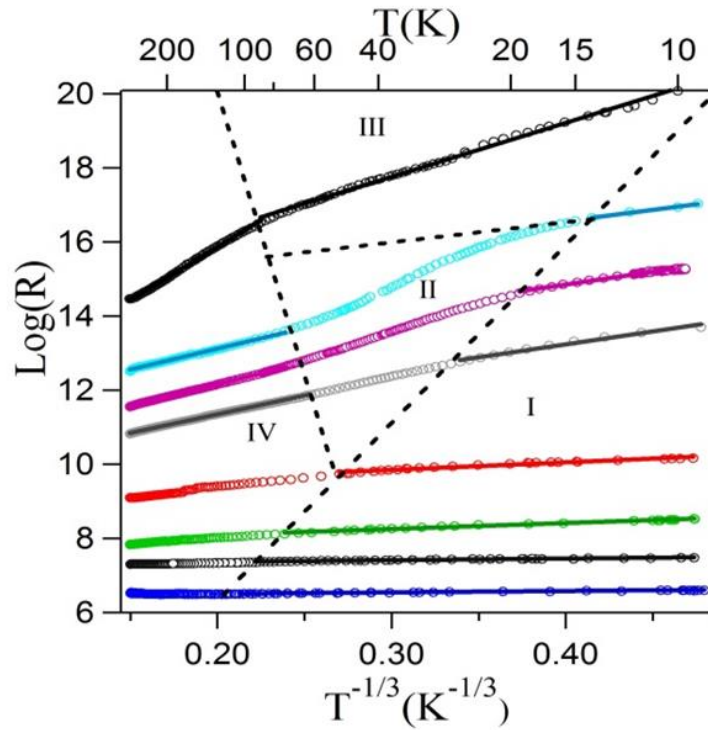


Figure 3.7 Log (R) vs $T^{-1/3}$ plot for VRH analysis.

Figure 3.7 shows the data for highly fluorinated graphene samples that can be fitted very well for the 2D-VRH theory at low temperature regime (below ~ 80 K). Meanwhile, another clear linear range for $T^{-1/3}$ dependence with a different slope is evident for high temperatures. In between we identify several regions with unique characteristic signatures as shown in Figure 3.7. Region I: low temperature R varies linearly with $T^{-1/3}$; region II: R vs. $T^{-1/3}$ becomes more non-linear as fluorination progresses; region III: insulating behavior with electron transport governed by VRH leading to strong localization (SL); region IV: high temperature R varies linearly with $T^{-1/3}$.

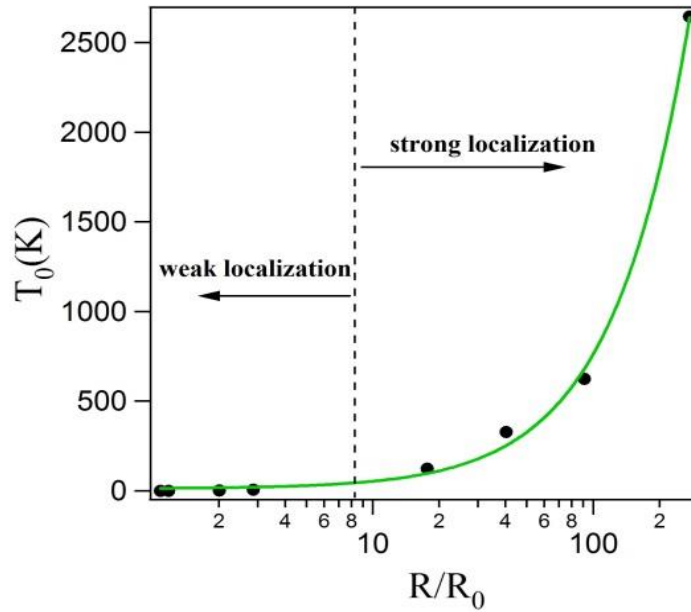


Figure 3.8 T_0 vs. R/R_0 values (T_0 is extracted from VRH fitting and R_0 is the room temperature resistance).

Figure 3.8 shows the T_0 value extracted from the fitting of VRH model to the low temperature data shown in Figure 3.5 vs. R/R_0 , where R_0 and R are the room temperature resistances of graphene before (degassed) and after each fluorination process respectively.

It should be noted that R/R_0 ratio represents the degree of fluorination. For the first few fluorination processes, T_0 remains lower than 10 K, indicating VRH is not the dominant mechanism of electron transport. However, for the last four fluorination processes, T_0 increases above 120 K for a value as high as 2600 K. This increase of T_0 marks the transition from WL to SL.

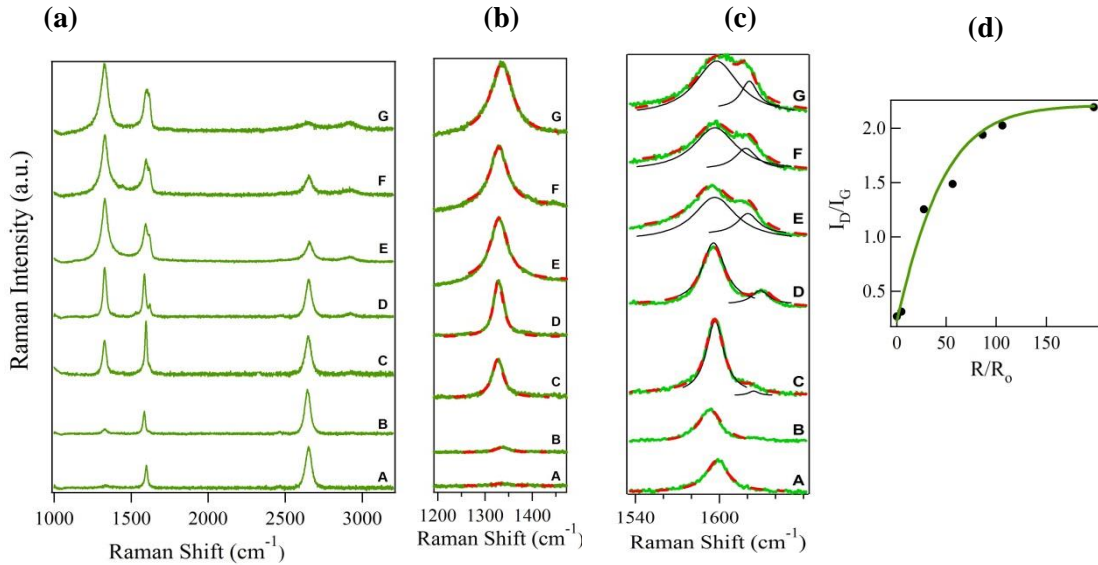


Figure 3.9 Raman spectroscopy results for (a) pristine and progressively fluorinated graphene (b) evolution of the D band (c) deconvolution of the G and D' bands and (d) Ratio of intensities of D and G bands, I_D/I_G vs. R/R_0 .

Figure 3.9 shows the Raman spectra for pristine and fluorinated graphene. G band at ~ 1580 cm⁻¹ assigned to the sp² in-plane phonon vibrations. 2D band at ~ 2700 cm⁻¹ is characteristic of the two phonon intervalley double resonance scattering. 2D band of pristine monolayer graphene is sharp and strong due to the absence of any defects. The intensity ratio I_{2D}/I_G was demonstrated to distinguish the number of layers of graphene. The observation of D band at 1340 cm⁻¹ originates due to the disordered structure of

graphene. This D band is serving as a convenient measurement of the amount of disorder in graphene. Figure 3.9 (b). shows the enhancement of the intensity of the D band as the fluorination progresses due to CF₄ plasma treatment. Figure 3.9 (c) shows the emergence of a new peak at ~1620 cm⁻¹ which is identified as the D' band arises due to the splitting of the G-band as a result of randomly distributed impurities. The intensity of D' band is seen to increase as the fluorination progresses. This new peak appears due to an intravalley double resonance process only in the presence of defects and shows up as a shoulder of the G band. Furthermore, a combination of D and G modes, the D + G band starts to appear near 2920cm⁻¹. The appearance of D, D' and D + G bands indicate the infliction of defects into the graphene lattice by the fluorine plasma [129]. During the progressive fluorination, G and 2D band intensities gradually decrease while the D and D' band intensities increase. Figure 3.9 (d) shows the ratio of the D-band to G-band intensities (I_D/I_G) corresponding to each fluorination process characterized by the change in the room temperature resistance, R/R_0 . The I_D/I_G ratio can be used to estimate the defects on the graphene film. The I_D/I_G ratio increases steeply during the initial fluorination but the rate of change becomes slower for heavy fluorination indicating reach of saturation. We utilized the $I_D/(I_D+I_G)$ ratio to estimate the degree of fluorination of each sample since this quantity represents the ratio between the number of sp³ defects and the total number of carbon atoms of the sample. However, it was necessary to account for the D band intensity of the pristine sample to estimate the degree of fluorination. The estimated degree of fluorination for sample A through G are 0%, 3%, 34%, 39%, 45%, 46%, and 48% respectively. CF₄ plasma induced fluorination of varying fluorine coverage are known to result in formation of CF, CF₂, CF₃ bonds as well as smaller fractions of CF-CF₂, C-CF, and C-CF₂ bonds indicating lattice

damage in the form of vacancy, void, terminal carbon, and fragmentation of the sheet in the fluorination process [130-131].

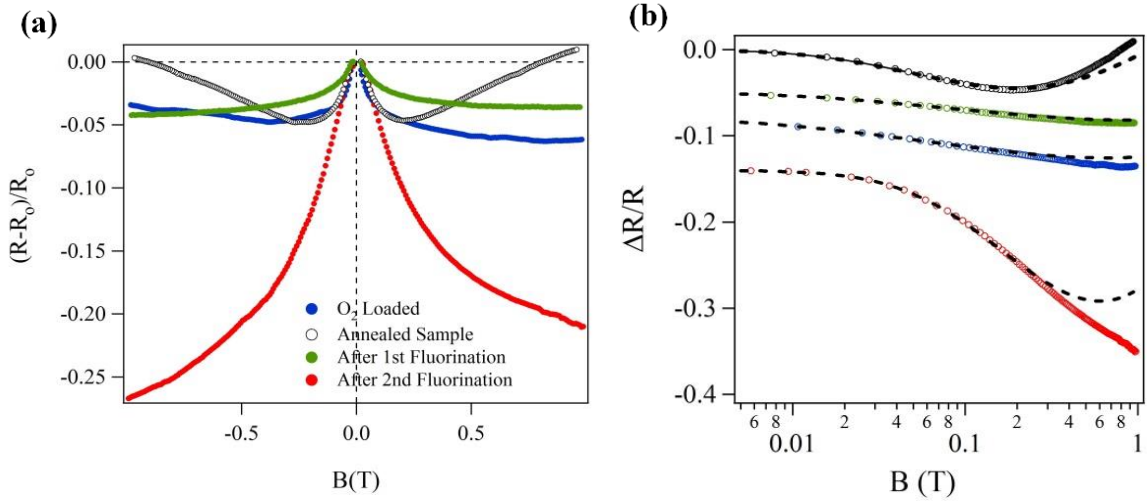


Figure 3.10 (a) Normalized Magnetoresistance ($\Delta R/R$) data for progressively fluorinated graphene. Data for the untreated graphene is also shown. (b) Normalized Magnetoresistance ($\Delta R/R$) data and the best fit for WL theory. Each data set has been offset in the ordinate for clarity.

Magnetotransport was also measured for these samples. Figure 3.10 (a) shows the normalized magnetoresistance, $MR=(R(B)-R(B=0))/R(B=0)$ for air exposed, degassed, and mildly fluorinated graphene samples with a perpendicular field at 10 K. All the samples show a negative MR at low magnetic fields. Air-exposed and mildly fluorinated samples show negative MR in the entire magnetic field range and believed to be governed by the weak localization effects. After first fluorination, MR is entirely negative and symmetric and well described by the theory of weak localization. The magnitude of the MR increases sharply as the subsequent second fluorination processes and it is seen to reach the strongly localized regime. To explain the behavior of MR, data were analyzed according to

localization theory developed for graphene. The correction to the semi-classical Drude conductivity is given by [132],

$$\delta\sigma = \frac{e^2}{\pi h} \left[F\left(\frac{\tau_B^{-1}}{\tau_\phi^{-1}}\right) - F\left(\frac{\tau_B^{-1}}{\tau_\phi^{-1} + 2\tau_{inter}^{-1}}\right) - 2F\left(\frac{\tau_B^{-1}}{\tau_\phi^{-1} + \tau_{inter}^{-1} + \tau_{intra}^{-1}}\right) \right]$$

Here, $F(x) = \ln(x) + \psi\left(\frac{1}{2} + \frac{1}{x}\right)$, where ψ is the digamma function,

$\tau_\phi^{-1} = L_\phi^2 / D$ is the phase coherence time, L_ϕ is the phase coherence length. The diffusion

constant D is expressed as $D = \frac{1}{2} v_F^2 \left(\frac{1}{\tau_{inter}} + \frac{1}{\tau_{intra}} \right)$ where $v_F \sim 10^6$ m/s is the Fermi

velocity. $B_x = \frac{\hbar}{4eD\tau_x}$ with $x = \Phi, inter, \text{ and } intra$, Then the magnetoresistance [21],

$$\frac{\Delta R}{R} = \frac{R(B) - R(B=0)}{R(B=0)} = -R_s \delta\sigma(B) \text{ is given by}$$

$$\frac{\Delta R}{R} = \frac{-e^2 R_s}{\pi h} \left[F\left(\frac{B}{B_\phi}\right) - F\left(\frac{B}{B_\phi + 2B_{inter}}\right) - 2F\left(\frac{B}{B_\phi + B_{inter} + B_{intra}}\right) \right]$$

where R_s represents the sheet resistance of the graphene sample.

Figure 3.10 (b) shows the offset data of MR with the best fit for WL theory. Both degassed and air-exposed graphene are also shown for comparison. The WL theory fits very well for the first fluorinated sample for magnetic field up to ~ 0.8 T. During the next fluorination process MR increases and the theory of WL fails to account for the higher magnetic field data above 0.2 T. This is an indication of a transition to strong localization regime. Unfortunately, we were not able to measure the MR for fluorinated sample in the

strong localization regime due to high impedance. A colossal MR in the strong localized regime has been observed by Hong et al [133]. The fluorination process may not be homogeneous due to the presence of multilayer islands, wrinkles, ripples, and grain boundaries which form a conductive network through which charge transport occurs [130]. Further, the grain boundaries tend to be highly reactive compared to pristine graphene, resulting in a pronounced functionalization between individual grains. The observed large MR properties may also be due to the introduction of highly reactive defects into the graphene surface as a result of ion bombardment. Early experiments on exfoliated graphene have shown a strong suppression of WL even at very low temperatures [134]. This is because mesoscopic conductance fluctuations dominate transport in these small graphene flakes since the sample sizes are comparable to the phase coherence length especially at low temperatures. However recent experiments have shown significant WL effects by averaging over many carrier concentrations [132]. It is expected that F atoms will first saturate the p_z orbitals at the grain boundaries, and after saturation of grain boundaries, F atoms will start to saturate the π -conjugated electronic structure of graphene.

Temperature dependence of S for graphene samples subjected to sequential fluorination processes is shown in Figure 3.11 (a). The p-type (positive S) behavior of air exposed CVD grown graphene is interpreted as due to electrochemically mediated charge transfer process while n-type (negative S) behavior of vacuum degassed graphene is presumably due to substrate effect. While air-exposed sample remains p-type, the degassed graphene sample remains n-type over the entire temperature range. Both air exposed and degassed samples show nearly linear temperature dependence. After a short fluorination process, S changed slightly from $\sim -40 \mu\text{V/K}$ to $\sim -25 \mu\text{V/K}$ and still remains n-type in the

entire temperature range. Even after exposure to air at this point, the S remains negative. Second fluorination changes S from negative to positive $\sim +20 \mu\text{V/K}$ and remains p-type throughout the entire temperature range with metallic characteristics consistent with metallic $R(T)$ behavior.

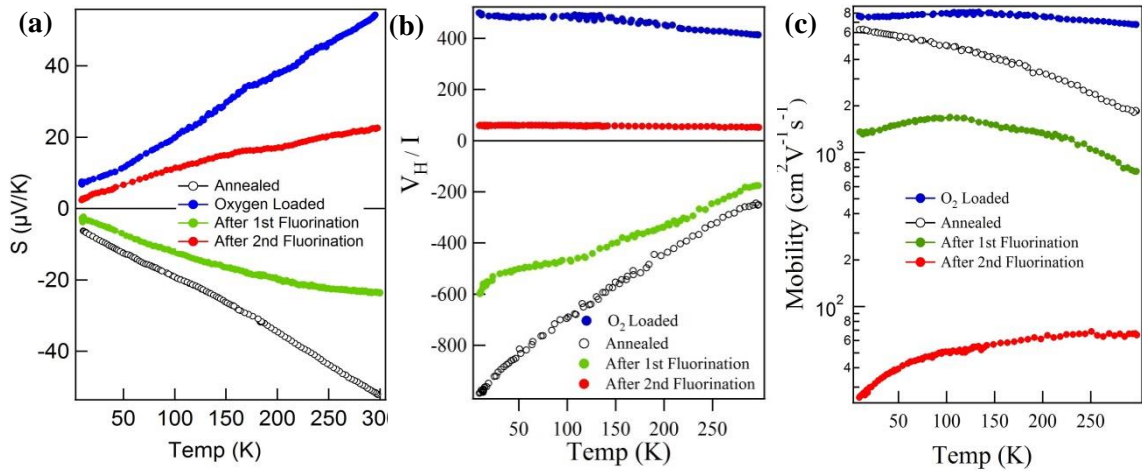


Figure 3.11 The temperature dependence of (a) thermopower, $S(T)$. (b) Hall voltage over excitation current, V_H/I for progressively fluorinated graphene.

Figure 3.11 (b) shows the temperature dependence of Hall resistance, $V_H/I(T)$, where I is the excitation current. Air-exposed graphene (prior to degassing) shows a $V_H/I \sim 420$ ohms. For the degassed graphene sample, $V_H/I \sim -200$ ohms and remains negative between 10 K and 300 K. Next V_H/I become slightly less negative after the first fluorination ~ -170 ohms and still shows n-type behavior throughout the entire temperature range. After the second fluorination, V_H/I increase up to $\sim +50$ ohms and remains p-type in the entire temperature range without any appreciable change. Figure 3.11 (c) depicts the temperature dependence of mobility, $\mu(T)$ for the fluorinated samples. It can be seen that air-exposed sample shows $\mu \sim 6700 \text{cm}^2\text{V}^{-1}\text{s}^{-1}$. Degassed sample shows reduced $\mu \sim 1857 \text{cm}^2\text{V}^{-1}\text{s}^{-1}$.

Due to the fluorination, mobility is seen to decrease down to $\mu \sim 750\text{cm}^2\text{V}^{-1}\text{s}^{-1}$, and $\mu \sim 65\text{cm}^2\text{V}^{-1}\text{s}^{-1}$ after the first and second fluorination processes respectively.

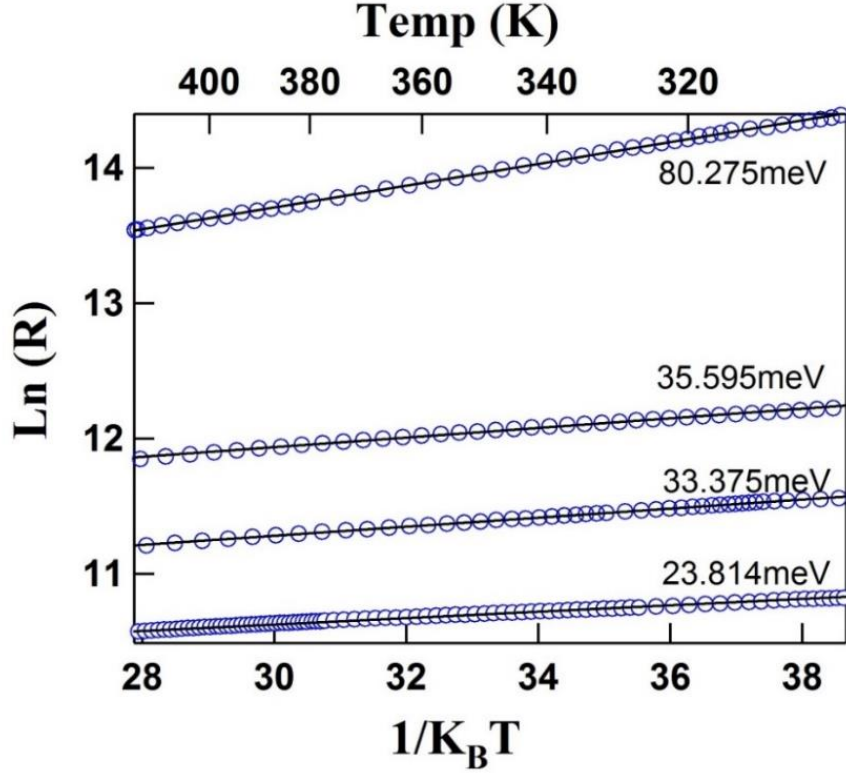


Figure 3.12 The Arrhenius plot of $\text{Ln}(R)$ vs $1/(k_B T)$ for densely fluorinated graphene samples at higher temperatures. The slope of the linear range is used to extract the band gap values.

In order to estimate the band gap, the temperature dependence of the four-probe resistance of the fluorinated samples were measured at higher temperatures up to 420 K. The Arrhenius plot of $\text{Ln}(R)$ vs $1/(k_B T)$ for densely fluorinated graphene samples are shown in Figure 3.12. The band gap, E_g was estimated using the temperature dependence of the conductivity, $\sigma = \sigma_0 \text{Exp}(-E_g/2k_B T)$, for an intrinsic semiconductor. The highest band gap for the most fluorinated graphene sample is found to be ~ 80 meV which is several

orders of magnitude less than what is expected from theoretical predictions of ~ 3.5 eV [30]. A systematic behavior of the band gap value is observed as the fluorination progresses.

3.4 Conclusions

In summary, we have studied electrical and magnetotransport properties of large area few layer graphene subjected to plasma induced fluorination. As the fluorination progresses it was found that the initial metallic behavior of graphene (with low temperature transport properties being governed by diffusion: linear S and finite σ as $T \rightarrow 0$) changes to insulating behavior ($\sigma \rightarrow 0$ as $T \rightarrow 0$) where transport properties obey variable range hopping (VRH). Onset of strong localization was seen with enhanced MR as the fluorination progresses. As determined by the high temperature resistance behavior, an emergence of a small band gap was observed and the band gap is seen to increase as the fluorination progresses.

CHAPTER 04

NITROGEN DOPING OF GRAPHENE: TRANSPORT PROPERTIES

4.1 Introduction

Graphene represents a major advancement in modern science and is one of the most promising materials for implementation in the next generation electronic devices. However, most electronic applications are handicapped by the absence of a semiconducting gap in pristine graphene. For example, the devices made from the zero-bandgap graphene are difficult to switch off, losing the advantage of the low static power consumption of the complementary metal oxide semiconductor technology. To use graphene in nano-electronic devices, a band-gap has to be engineered which will in turn reduce its electron mobility. Such a band-gap can be created by surface functionalization or chemical doping. Theoretical[135] and experimental[136] studies have shown that doping graphene can tailor the physical/chemical properties of graphene and open the possibilities of new chemistry and new physics on graphene. Substitutional doping of graphene with different atoms results in the disruption of ideal sp^2 hybridization of the carbon atoms, thus locally inducing significant changes in their electronic properties and chemical reactivity.

Among the numerous potential dopants, the boron (B) and nitrogen (N) atoms are the natural candidates for doping in graphene due to their similar atomic size as that of carbon (C) and of their hole acceptor (p-type) and electron donor (n-type) characters for

substitutional B- and N-doping, respectively (Figure 4.1). Doping with nitrogen might confer useful chemical properties to graphene, e.g., rendering it catalytic to oxygen reduction reaction [137] or enhancing its lithium intercalation properties for battery applications [138]. In addition, N-doping could also enhance the biocompatibility of carbon nanomaterials and therefore is favorable for biosensing applications [139].

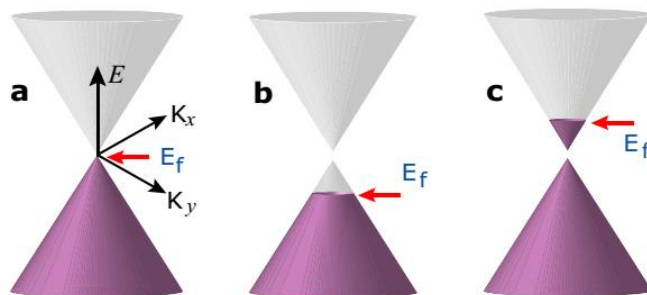


Figure 4.1 Schematic band structures of graphene. (a) Band structure of pristine graphene with zero bandgap. Band structures of (b) p-type and (c) n-type graphene with the bandgap.

Generally, graphene doped with N atoms would generate three common bonding configurations within the carbon lattice, including quaternary N (or graphitic N), pyridinic N, and pyrrolic N, as shown in Figure 4.2. Specifically, quaternary N refers to N atoms that substitute for C atoms in the hexagonal ring. Pyridinic N refers to nitrogen atoms at the edge of graphene planes, each of which is bonded to two carbon atoms and donates one p-electron to the aromatic π system. Such pyridinic N doping in carbon materials was generally considered to be responsible for their enhancement of oxygen reduction reaction (ORR) activities [140]. Pyrrolic N refers to nitrogen atoms that are bonded to two carbon atoms and contribute to the π system with two p-electrons. Because of the intriguing structures and properties, N doped graphene has been widely used in the fields of

electronics [141], fuel cells [142], secondary batteries [143-144], supercapacitors [145], and so on.

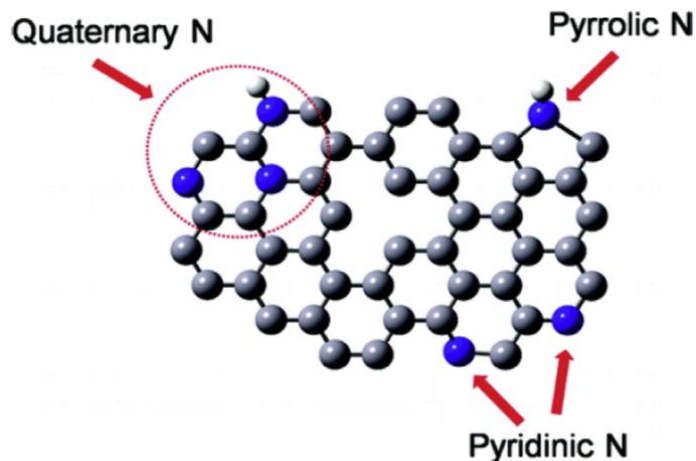


Figure 4.2 Three common bonding configurations of Nitrogen-doped Graphene [139].

4.2 Nitrogen doping of graphene

Numerous approaches have been proposed to synthesize nitrogen-doped graphene, two common methods involved for the synthesis are categorized as direct synthesis and post treatment. Direct synthesis includes nitrogen-containing precursors in chemical vapor deposition (CVD) [146-147], segregation method, solvothermal and arc discharge methodologies whereas, post treatment method involves thermal annealing of graphene oxide in ammonia [148] and N_2/NH_3 plasma treatment [149-150].

In the CVD method, the nitrogen content can be controlled by changing the flow rate and the ratio between carbon source (CH_4 , C_2H_4) and nitrogen source (NH_3). The bonding configuration of nitrogen doped graphene varies with different catalyst and precursor[151]. The synthesis of nitrogen doped graphene have revealed that the doping

environment is influenced by the flow rate, catalyst, and growth temperature. When carbon material is placed in nitrogen plasma atmosphere, carbon atoms will be partly replaced by nitrogen atoms, therefore, this method was applied to synthesize nitrogen doped graphene. The nitrogen content can be easily controlled by the plasma strength and/or exposure time.

4.3 *in-situ* characterization of nitrogen doping of graphene

Graphene was first synthesized by chemical vapor deposition on copper foils using CH_4 gas and transferred to Si/SiO₂ or glass substrates as described in Chapter 02. Electrical transport studies were performed on graphene transferred onto glass substrates. Two Chromel (KP/Au-7 at. % Fe (Au: Fe) thermocouples and a platinum resistive heater were utilized for thermopower measurements. Two additional copper wires were used for simultaneous 4-probe resistance measurements as described in Ref [152]. A custom-designed split ring capacitively coupled RF plasma system (13.56 MHz, max. power 600 W) was used at room temperature to generate nitrogen plasma as shown in Figure 4.3. Plasma exposure time was established by *in situ* monitoring of the change in resistance and thermopower of the sample. For low-temperature measurements, a chip carrier supporting the graphene sample was transferred to a closed cycled refrigerator (Janis Research Co. CCS-350ST-H) which can be cooled down to a base temperature of ~ 8 K. The sample-containing refrigerator column is enclosed by an electromagnet (LakeShore model EM4-CV 4-in. gap, Horizontal Field) capable of producing magnetic field which can be swept between -1 and $+1$ T [153].

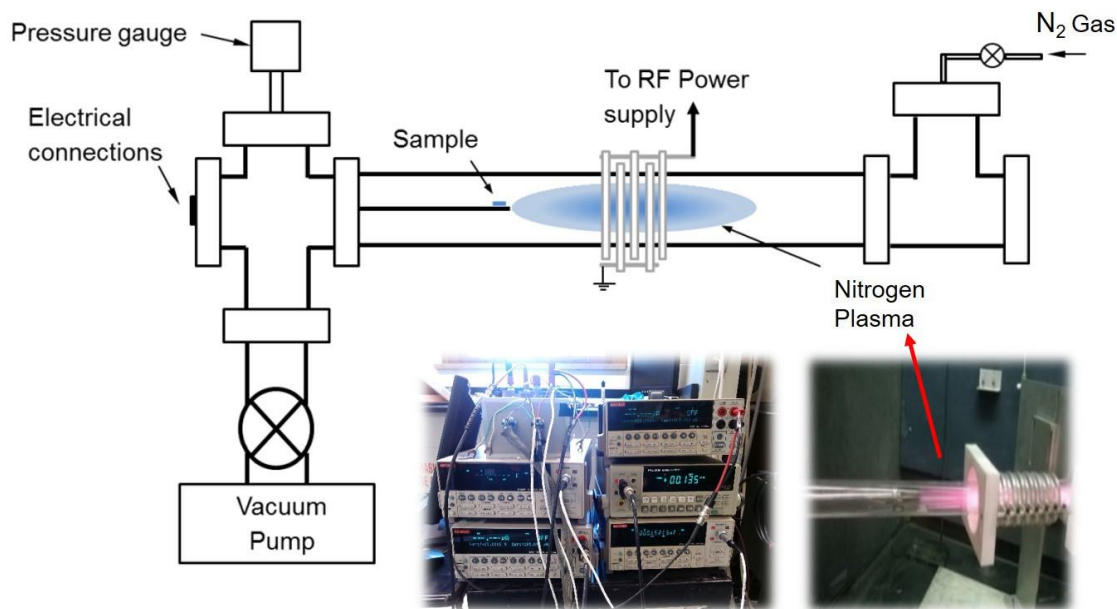


Figure 4.3 Schematic of the plasma doping of graphene and *in-situ* measurement setup.

The Raman spectra were collected using an Invia Renishaw Raman spectrometer with the excitation wavelength of 632 nm. The X-ray photoelectron spectroscopy (XPS) measurements were performed using a MultiLab 3000 VG Thermo Scientific surface analysis system. Mg K α (1253.6 eV) radiation was used as the excitation source, and the measurements were performed at room temperature and under ultrahigh vacuum conditions at pressures in the 10^{-9} Torr range. All the samples used for transport measurements and Raman/XPS characterization were subjected to nitrogen plasma under identical conditions. Two samples each for XPS and Raman were placed in addition to the sample used for transport study. All the samples were kept in close proximity to ensure they undergo similar plasma treatments.

Figure 4.4 (a) and (b) show the *in-situ* time evolution of R and S of the graphene during two successive nitrogen doping processes. The graphene sample was carefully

exposed to the nitrogen plasma of 25 KW for a short period of time (~ 60 s) at a gas flow rate of 15 standard cubic centimeters per minute (sccm) and the pressure was ~ 200 mTorr, the plasma was then turned off and the monitoring of the change in R and S was continued. Extreme care was taken in order to not inflict any damages to the sample during the process. Sample was at the floating potential.

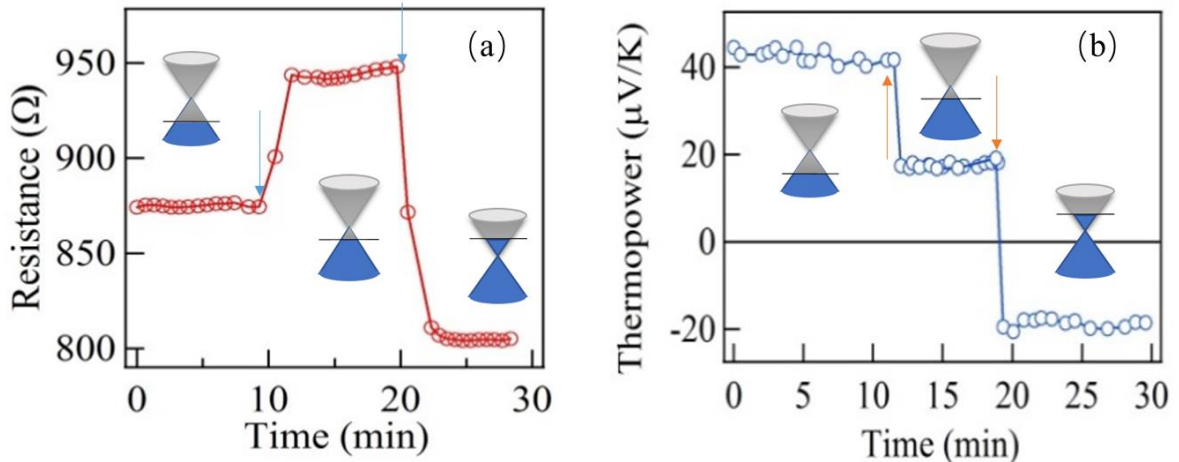


Figure 4.4 (a) In situ time evolution of the resistance, $R(t)$ and (b) thermopower, $S(t)$ during nitrogen doping. The arrowheads represent the initiation of intermittent plasma.

Pristine graphene is typically p-type due to the residual species (e.g., oxygen and water molecules) adsorbed on the surface of graphene. This ambient p-type behavior has been identified as due to electrochemically mediated charge transfer mechanism between a redox couple in humid air and the Fermi energy of graphene [154-155]. In our previous work on hydrogenation and fluorination [121, 125], we studied the functionalization effects on degassed sample in order to minimize the influence the effect of oxygen. But in the case of nitrogen doping, we were interested in the effect of substitutional doping of graphene with nitrogen which has less profound effect on the functional groups such as oxygen.

Further, the conditions used in this study (high pressure and low temperature) are not sufficient for effective degassing.

During the first nitrogen doping process, R was found to increase from its initial value of ~880 ohms to ~950 ohms and saturate. During this period, S was found to decrease from its initial value of ~+42 $\mu\text{V}/\text{K}$ (p-type) down to a ~+19 $\mu\text{V}/\text{K}$ (still p-type) and saturate. During the next nitrogen doping process, R continues to decrease down to a saturated value of ~790 ohms while S reverses its sign and saturates at a value of ~ -19 $\mu\text{V}/\text{K}$. This confirms n-type doping of graphene due to the nitrogen atom incorporation into graphene. The nitrogen doping effectively modulates the electrical properties of graphene by shifting the Fermi level above the Dirac point.

4.4 *ex-situ* characterization of nitrogen doped graphene

Temperature dependence of the transport properties were measured for both pristine graphene and nitrogen-doped graphene. Figure 4.5 shows the temperature dependence of S (left axis) and R (right axis) for the pristine and nitrogen-doped graphene. For the pristine graphene, S(T) remains p-type throughout the entire temperature region with a nearly linear behavior, while R(T) show weak temperature dependence at high temperatures and increases at low temperatures. Nitrogen-doped graphene remains negative and shows linear S(T) behavior while R(T) increases with lowering T throughout the temperature range. The pronounced R(T) dependence of nitrogen-doped graphene can be attributed to the enhanced scattering due to nitrogen dopants and presence of localized states in the conduction band induced by doping.

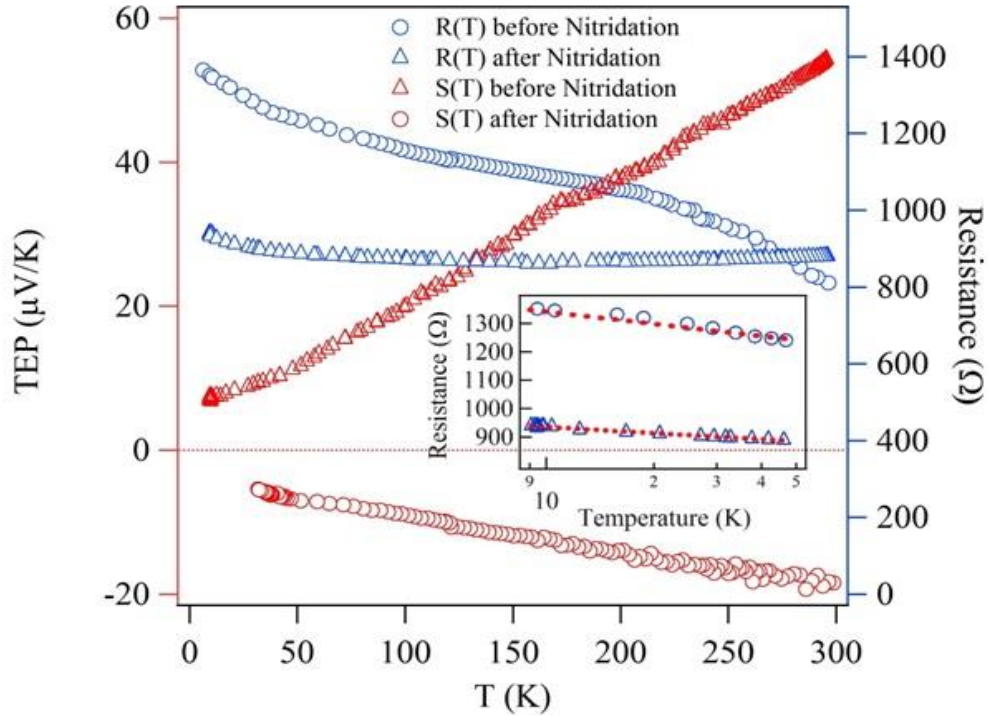


Figure 4.5 Temperature dependence of Resistance (Right axis) and Thermopower (left axis) of graphene before and after nitrogen doping. Inset: Low temperature (below 50K) resistance behavior with logarithmic temperature axis.

The inset in Figure 4.5 shows the low temperature behavior of the resistance for both samples with logarithmic temperature axis. Both resistance curves show obvious logarithm dependence at low temperatures. Generally, a two-dimensional system in the weakly localized regime exhibits logarithmic temperature dependence of resistance [156].

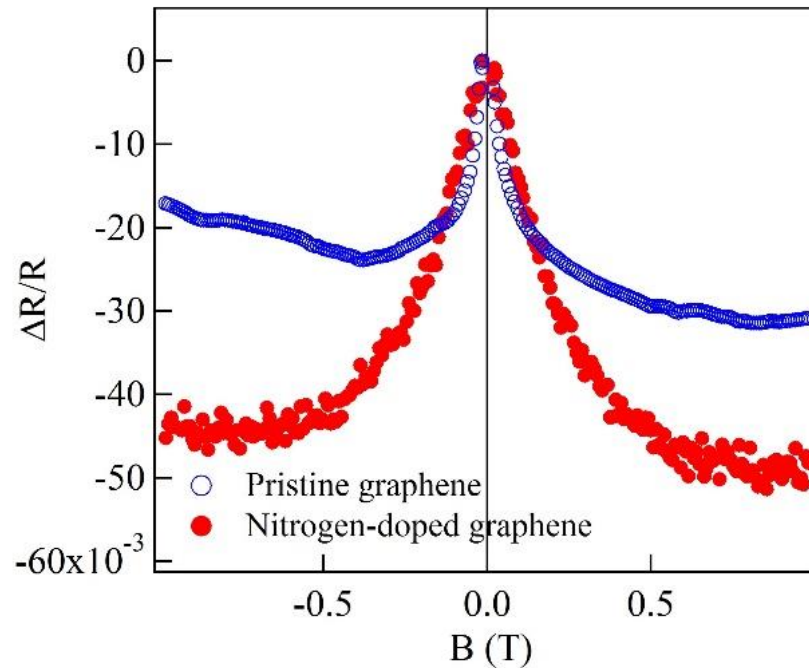


Figure 4.6 Magnetotransport: Magnetoresistance (MR) data for pristine and nitrogen-doped graphene. Dataset is offset for clarity.

Figure 4.6 shows the MR data for pristine and nitrogen-doped graphene at 8 K. The negative MR was observed for both samples in the entire magnetic field range. The pristine graphene sample shows asymmetry in the data presumably due to the contact misalignments. However, after first nitrogen doping, MR is remarkably symmetric. The negative MR with an abrupt decrease of MR near zero magnetic field strongly suggests weak localization (WL) effects for both samples and inherent for the systems where conductivity can be described in the framework of WL theory [157]. Furthermore, larger MR was observed for nitrogen-doped graphene due to an enhancement of weak localization. The low-temperature data are analyzed according to WL theory developed for graphene.

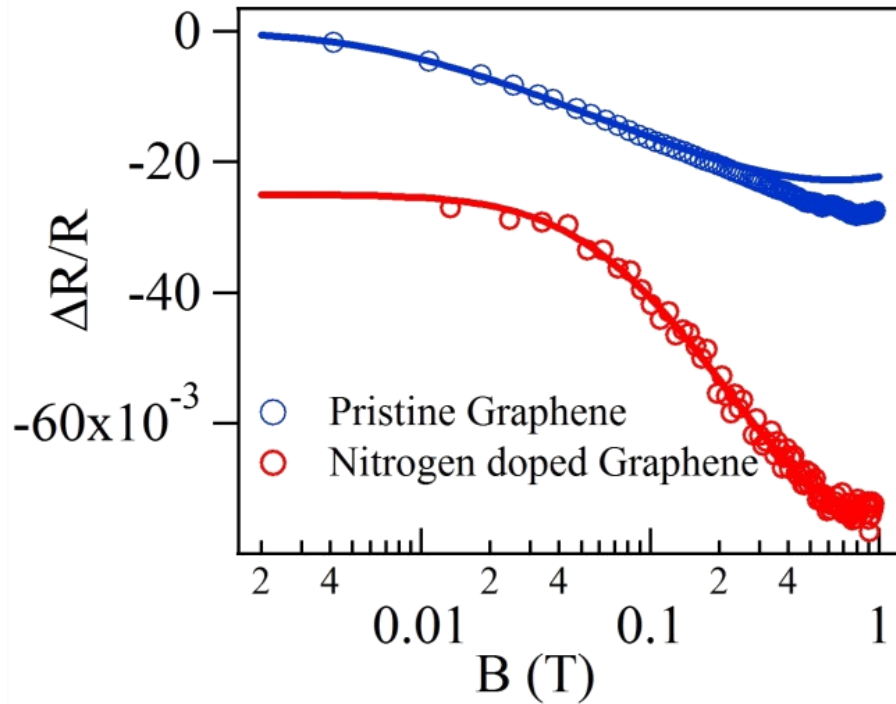


Figure 4.7 Magnetotransport: ($\Delta R/R$) data for pristine and nitrogen-doped graphene with the best fit for WL theory at low magnetic field values in logarithmic B axis.

Figure 4.7 shows the MR data with the best fit for WL theory at low magnetic fields. Each data set is offset for clarity. For pristine graphene, the WL theory fits well only for low magnetic fields up to ~ 0.2 T. However, for nitrogen-doped sample, WL can account for the entire B field range. This can be attributed to the doping induced disorder. At low magnetic fields, we use quantum transport signals to quantify the transport properties. Analyses based on weak localization models allow us to determine the phase coherence and scattering times. The dephasing magnetic field, B_ϕ was found to be larger for nitrogen-doped graphene than the one for pristine graphene. Our results support an increased elastic intervalley scattering emanating from the increased disorder with short range potentials

leading to enhancement of the weak localization for nitrogen-doped graphene. This is in excellent agreement with the Raman spectroscopy results.

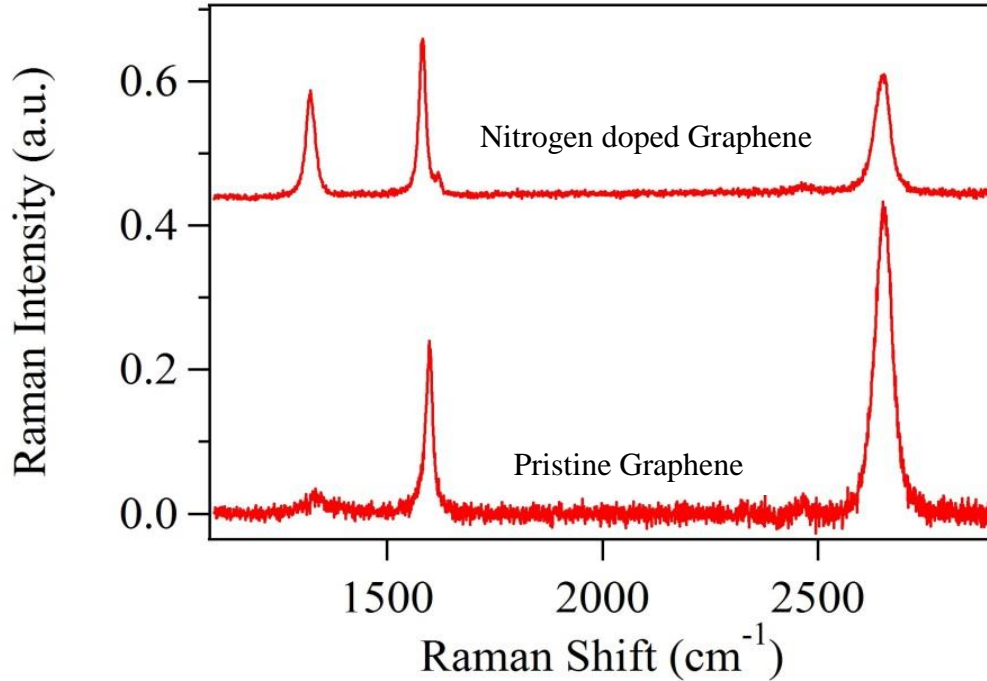


Figure 4.8 The Raman spectra of graphene sample before and after nitrogen doping.

Figure 4.8 shows a series of Raman spectra for nitrogen-doped graphene including pristine graphene. The two intense peaks, G band at $\sim 1580 \text{ cm}^{-1}$ and G'(2D) band at $\sim 2700 \text{ cm}^{-1}$, are characteristic of graphene samples due to the in-plane vibrational (E_{2g}) mode and the two phonon intervalley double resonance scattering, respectively. The peak at 1340 cm^{-1} is assigned to D band and presumed to be related to domain boundaries and growth nucleation sites. The large G-band and D-band intensity ratio, $I(G)/I(D)$ and large 2D band and G-band intensity ratio, $I(2D)/I(G)$ for pristine graphene are evident for its high degree of crystallinity. Further, the high symmetry of the 2D band confirms the presence of mostly monolayers in the graphene sample. After nitrogen doping, the D band intensity becomes

more intense and attributed to the coupling of the phonons with elastically scattered photo-excited electron created by the nitrogen atoms embedded in the graphene lattice. The emergence of D' band for nitrogen-doped graphene is presumed to be due to intravalley double resonance scattering processes. This will allow us to estimate the conductivity of our graphene samples. Our sheet resistance is, $R_s = \sim 880 \Omega/sq$. This is consistent with the mobility value, $\sim 7000 \text{ cm}^2/Vs$, and carrier density, $n = 10^{12} \text{ cm}^{-2}$, giving sheet resistance $R_s = 1/en\mu \sim 892 \Omega/sq$. If the thickness (t) of 0.33 nm (one layer), conductivity, σ is given by $\sigma = 1/R_s t = 1/880 \times 0.33 \times 10^{-9} = 0.3 \times 10^5 \text{ S/m}$.

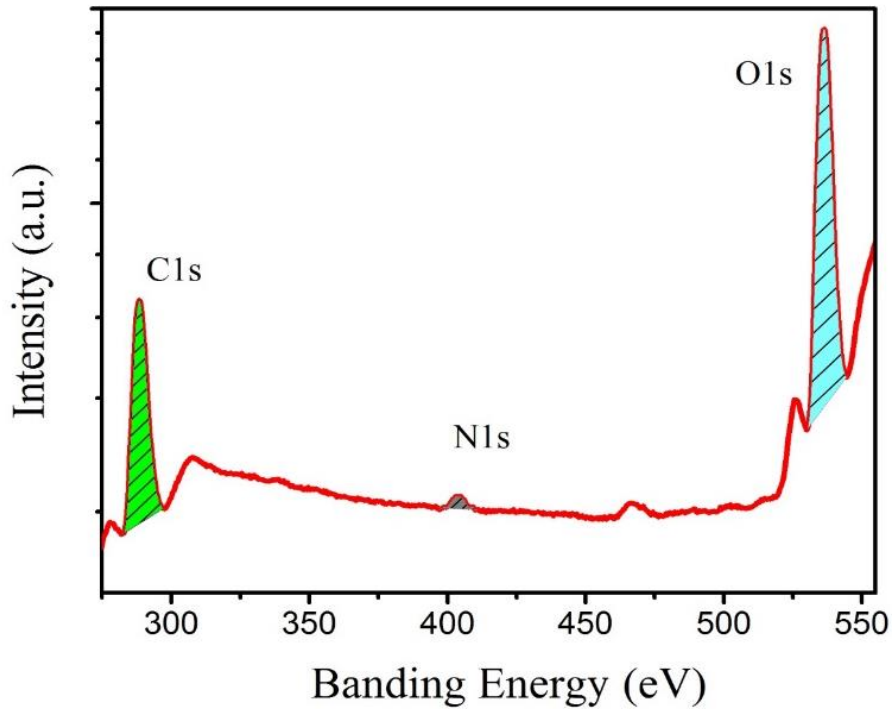


Figure 4.9 XPS survey spectrum of nitrogen doped graphene

Figure 4.9 shows the survey XPS spectrum of nitrogen doped graphene sample. Two strong peaks characteristic of C1s and O1s, as well as a weak peak characteristic of N1s are clearly seen in this XPS spectrum. By evaluating the areas under each peak and

considering the atomic sensitivity factors for each element, we estimate the carbon oxygen, and nitrogen content to be 40:56:1. This results in N/C ratio of 2.5%.

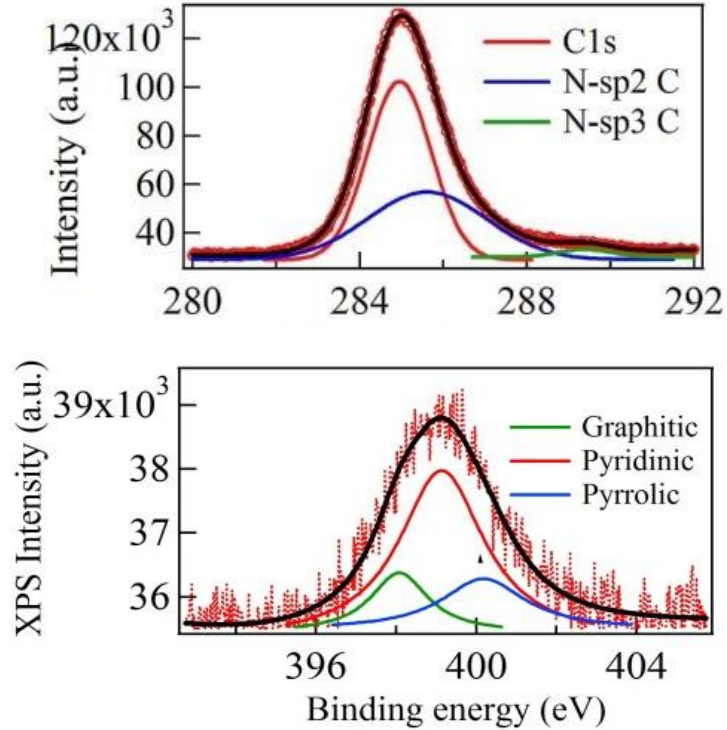


Figure 4.10 (a) The C1s XPS peak, (b) the N1s XPS peak for nitrogen-doped graphene

Figure 4.10 (a) shows the C1s peak of the XPS spectra fitted with three components: the main peak at a binding energy (BE) of 284.7 eV is assigned to sp² hybridized C atoms in graphene (C1s); other two peaks at 285.4 eV and 288.8 eV could be attributed to C-N bonding (with sp²- and sp³-hybridized carbon and nitrogen group structures). Figure 4.10 (b) shows the N1s peak of the XPS spectra fitted with three peaks in the binding energy range of 398-401 eV suggesting the presence of at least three types of C-N bonding: graphitic nitrogen located at 400.2 eV, a pyrrolic-N appeared at about 399.5 eV, and a pyridine-N signal located at 398.1 eV.

4.5 Conclusion

In summary, *in-situ* electronic transport properties of graphene during electron doping by nitrogen plasma were presented. In contrast to doping during growth or post-growth doping, *in-situ* monitoring of doping effects can offer a better understanding of processing technologies. It shows that the nitrogen doping effectively modulates the electrical properties of graphene by shifting the Fermi level above the Dirac point. *ex-situ* studies of temperature and magnetic field dependence of transport properties provide valuable information about electron doping and scattering processes, support an increased elastic intervalley scattering emanating from the increased disorder with short range potentials leading to enhancement of the weak localization for nitrogen-doping graphene. Raman and XPS provide structural information which were in excellent agreement with the transport properties after nitrogen doping.

CHAPTER 05

TRANSPORT PROPERTIES OF GRAPHENE-NOBLE GAS ADSORPTION

5.1 Introduction

The adsorption of gas on surface of graphene-based carbon allotropes (such as graphite and carbon nanotube) has attracted much attention because of its considerable potential applications in nanotechnology. Graphene-based materials (pristine graphene, graphene oxide, and reduced graphene oxide) show distinct gas adsorption characteristics due to their high specific surface area and unique electrical properties such as high mobility and low electrical noise [158-164]. The two-dimensional structure of graphene makes the electron transport highly sensitive to the adsorption of gas molecules. It possesses low intrinsic noise and high electrical conductivity even in absence of charge carriers, thus few charge carriers induced by the gas adsorbates lead to notable changes in charge carrier density resulting in detectable changes in electrical conductivity. Graphene is a p-type semiconductor in nature. When it is exposed to various gases, the response of its conductance could possibly be different. The adsorption of electron-withdrawing gas molecules such as NO_2 enhances the doping level of graphene and increases its conductance [165-167]. On the other hand, electron-donating molecules such as NH_3 dedopes graphene and decreases its conductance [168].

The adsorption of noble gases on various surfaces is a very active research field, as it provides manageable model systems that can deepen the understanding of physical adsorption of atoms onto crystalline surfaces [169]. Many theoretical works [169-172] have been studied regarding the adsorption of gases such as argon (Ar), krypton (Kr), and xenon (Xe) on single layer graphene, which are suitable substrates to study different phases of gas adsorbents. Here we investigated the transport properties of graphene with the adsorption of He, Ar, and Kr at temperature ranging from 100 to 500 K.

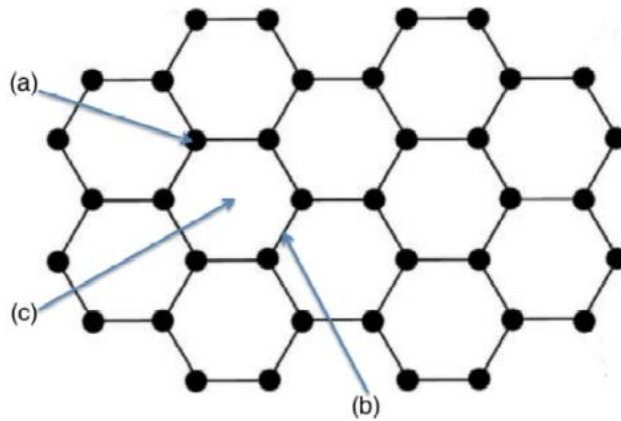


Figure 5.1 Three different adsorption sites on top of graphene: above (a), bridge (b) and center (c).

5.2 Noble gas adsorption of graphene

Graphene films for gas adsorption were first synthesized on copper foil in home-made CVD system and transferred directly onto glass substrates as described in Chapter 03. The resistance and thermoelectric power of graphene during gas adsorption were measured using a chip carrier supporting the graphene sample as shown in Figure 5.2. A dewar with liquid nitrogen was used for low-temperature measurements.

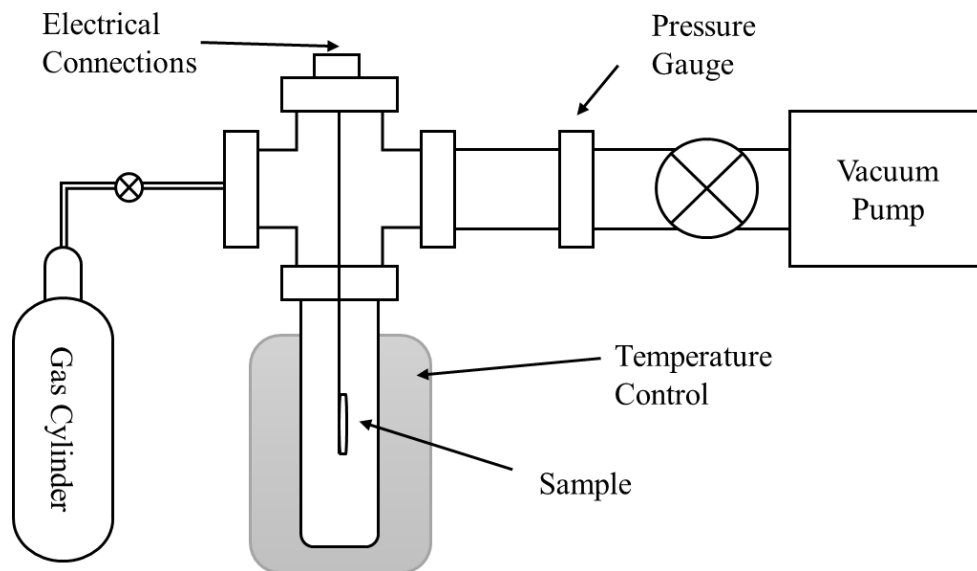


Figure 5.2 Schematic of the gas absorption measurement setup.

Before starting the experiment, the chamber was first evacuated to a based pressure below $\sim 10^{-6}$ torr using a turbo molecular pump and degassed at 500 K, while the time evolution of the resistance (R) and thermopower (S) was recorded concomitantly. During degassing, S was found to undergo a sign change from positive to negative and the resistance increased and reached a maximum value when S reaches 0. Eventually, the resistance decreased to a saturated value. After the degassing process, the valve of turbopump was closed and the noble gas was introduced to the chamber with 1 standard atmospheric pressure. Once the R and S reached a saturated value, desorption was started by pumping out the noble gases. The temperature of the chamber was controlled to decreased from 500 K to 100 K using liquid Nitrogen.

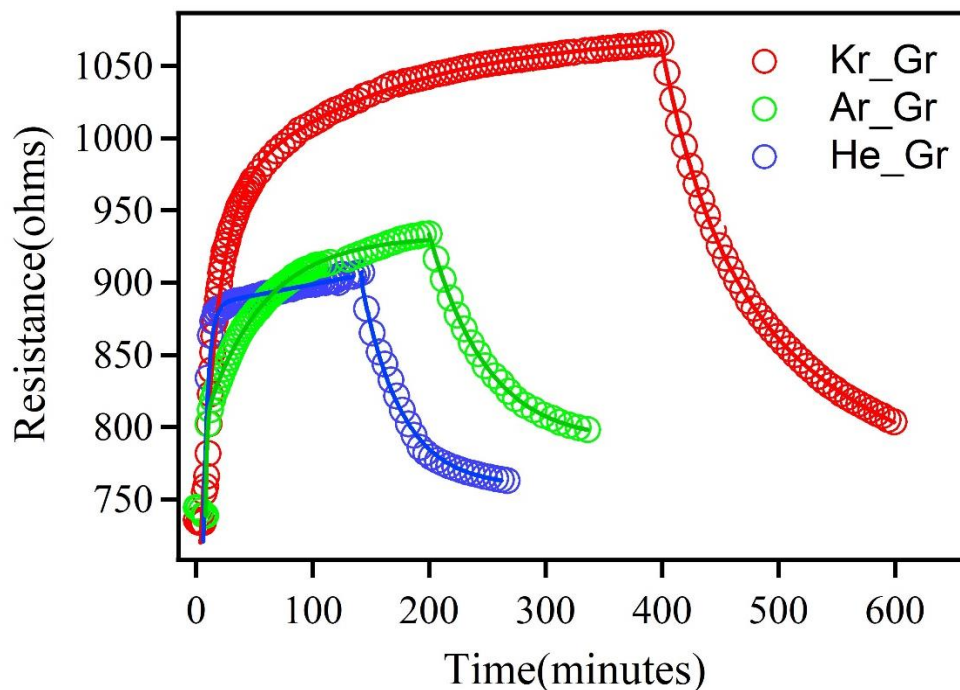


Figure 5.3 Resistance of graphene during noble gas adsorption and desorption.

Figure 5.3 shows the time evolution of resistance during noble gas (Kr, Ar, He) adsorption and desorption at room temperature. The adsorption of the noble gases on graphene reduces the delocalized electrons which shifts the Fermi level towards the Dirac point. It causes the increase of resistance as shown in Figure 5.3. For Kr adsorption, the resistance increased from initial value of ~ 700 ohms to final value of ~ 1050 ohms while for He and Ar adsorption it increased only to a final value ~ 900 ohms and ~ 940 Ohms respectively. It can be explained by the molecular dynamics calculations which assume that the strength of the van der Waals interactions between noble gases and carbon follows the order $\text{Kr} > \text{Ar} > \text{He}$, based on the binding energies measure of noble gases adsorbed on graphite [173]. It is also known that the surface binding energies depend on the substrate geometries such as defects. At the nanoscale, defects could be extremely useful since they could be exploited to adsorb noble gases.

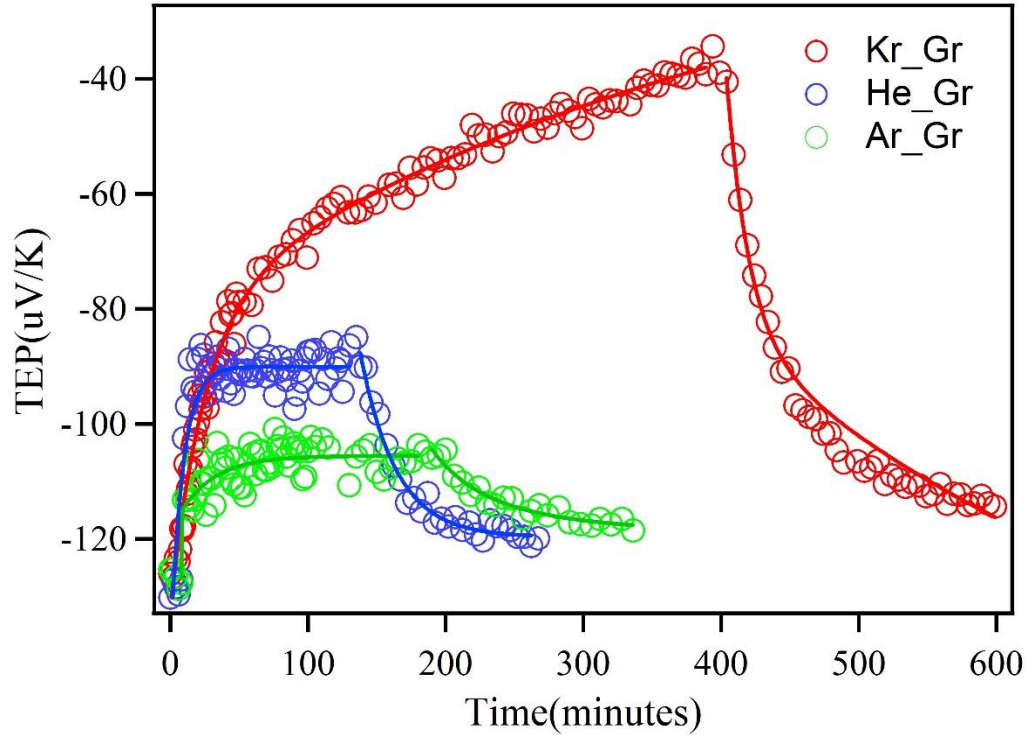


Figure 5.4 Thermopower of graphene during noble gas adsorption and desorption.

Corresponding to the resistance change during the gas adsorption, thermoelectric power also shows similar changes. In all three cases, negative thermopower was found to settle at a less negative value after the adsorption process. It showed substantially increase of S from $\sim 130 \mu\text{V/K}$ to $\sim 40 \mu\text{V/K}$ for Kr adsorption whereas, for Ar and He adsorption S increased to only $-110 \mu\text{V/K}$ and $-90 \mu\text{V/K}$ respectively. The size of these gas atoms is similar: Kr is only 6% larger than Ar. However, Kr seems to have the right size to form a commensurate solid on graphene while almost matching the density of the 2D incommensurate solid, hence doubling the energy rewards [170].

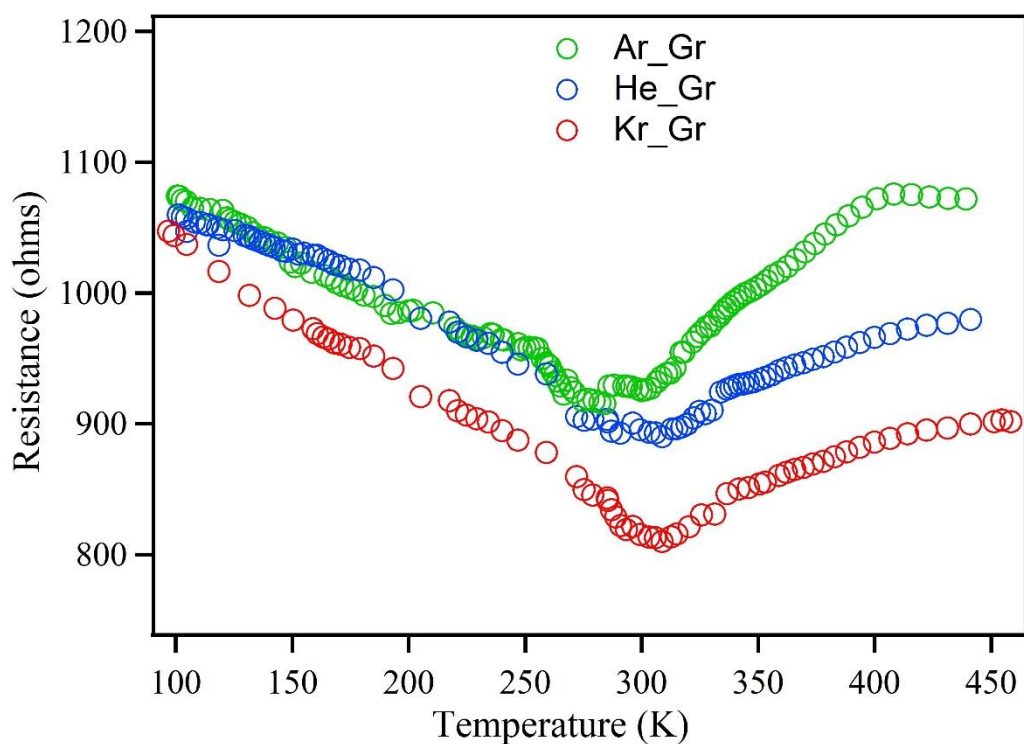


Figure 5.5 Temperature dependent on resistance of graphene with different noble gases adsorption

Temperature dependence of the resistance was measured for graphene with Kr, Ar, and He adsorption from 100 K to 500 K as shown in Figure 5.5. The resistance of the adsorbed graphene started decreasing with decrease in temperature from 500 to 300 K, indicating metallic behavior, while the resistance started to increase linearly with decreasing temperature from 300 to 100 K which is characteristic feature of intrinsic semiconducting behavior and is generally agreed to be due to the increase in thermally generated electron-hole pairs.

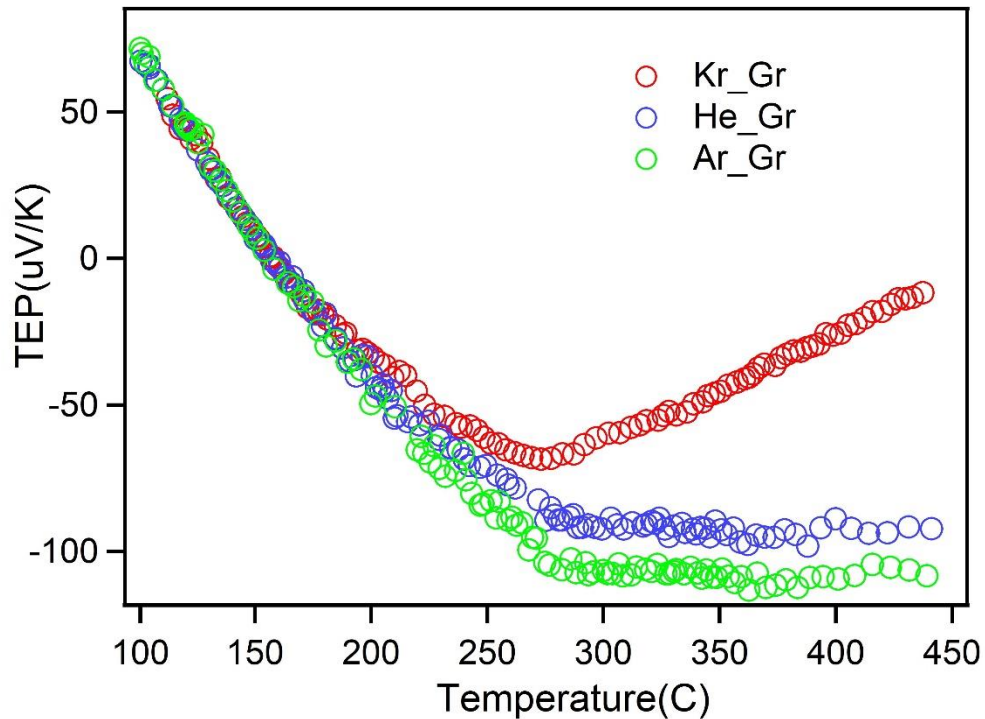


Figure 5.6 Temperature dependent of thermopower of graphene with different noble gases adsorption

Figure 5.6 shows the temperature dependence of thermopower S for adsorbed graphene samples. For Kr adsorption, S initially decreased at high temperature (270~500 K) but started to increase with further decrease of temperature (270~100 K). The Ar and He adsorption showed similar behavior, but with little or no change at high temperatures, started to show linear temperature dependence below ~280 K.

5.3 Conclusion

In summary, transport properties of graphene with noble gas adsorption were studied experimentally. The sensitivity of S and R for various noble gas adsorption can be related to the two-dimensional nature of the transport and the defects in graphene. Theoretical

calculations to investigate the scattering mechanism for various adsorption sites and molecules are now needed. As these calculations will have to deal with the details of the molecule-graphene interaction, it is hoped that these calculations and the data presented here will provide quantitative insight into the details of the gas-graphene interaction.

CHAPTER 06

SYNTHESIS AND CHARACTERIZATION OF PECVD GRAPHENE NANOWALLS

6.1 Introduction

It is well-known that sp^2 carbon, which is the most stable elementary form of carbon at room temperature, can lead to various kinds of layered structures. Among these structures, graphene is a true 2D material with the large anisotropy between the in-plane and out-of-plane directions providing possibilities to manage the 2D growth. Various methods for the synthesis of graphene have been reported, which include mechanical exfoliation from highly oriented pyrolytic graphite [9, 174], chemical exfoliation from bulk graphite [175-177], thermal decomposition from 4H-SiC substrate [178-179], etc. Recently, chemical vapor deposition (CVD) has been successfully employed to synthesize uniform and large-scale graphene films on metal substrates such as Copper and Nickel foils [180-186]. However, thermal CVD growth of graphene at high processing temperatures (1000-1600 °C) [187-189] is not cost-effective and limits the application of graphene in optoelectronic devices. Furthermore, the obtained graphene films need to be separated from the metal substrates and then transferred to insulating substrates (e.g., dielectrics, insulators) for further electronic processing [72].

Currently, use of polymethyl-methacrylate (PMMA) or polydimethylsiloxane (PDMS) to aid the transfer of graphene films is the most common approach [14, 87, 190-191]. During such complicated transfer procedures, the introduction of cracks or tears, and contamination of PMMA into graphene films are unavoidable. In this regard, to lower the reaction temperature and avoid the limitations of substrates, plasma-enhanced CVD (PECVD) has been widely used to synthesize transfer-free graphene films on different substrates including both metals and insulators [192-199].

On the other hand, PECVD is among the early methods to synthesize vertically standing few layer graphene or graphene nanowalls as shown in Figure 6.1. Compared with planar graphene sheets randomly laid down on to a substrate, graphene nanowalls (vertically oriented graphene nanosheets), graphene nanoflakes and carbon nanoflowers, can be categorized into a class of networks of the graphene oriented vertically on a substrate [193]. They have attracted substantial interest for potential applications in field emission, energy storage, gas sensing, biosensors, and lithium-ion batteries due to their unique orientation, no-stacking morphology and specific surface area.

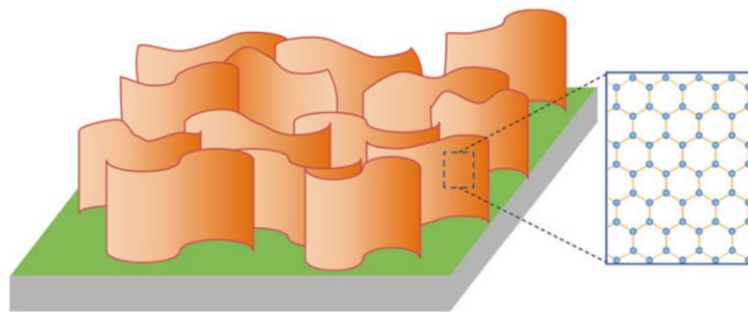


Figure 6.1 Schematic illustration of graphene nanowalls.

Here, we directly synthesized uniform and vertically oriented graphene films on multiple substrates including glass, Si/SiO₂ wafers, Cu foils through radio-frequency PECVD using methane (CH₄) as the precursor at a relatively low temperature. Electrical transport properties and surface characteristics have been presented to elucidate the electronic transport mechanisms and demonstrate the potential of this low temperature and transfer-free graphene growth method for future graphene-based electronic applications.

6.2 Plasma Enhanced CVD of graphene nanowalls

Throughout the experiments, graphene nanowalls were synthesized in a home-made split ring radiofrequency (13.56 MHz, Max. power 600W) PECVD system (as shown in Figure 6.2) on glass, SiO₂/Si wafers, and copper foil simultaneously. Prior to synthesis, all the substrates were sonicated in acetone for 10 min, dried using a nitrogen blow gun, and placed inside the quartz reactor. Then the reactor was evacuated until the pressure lower than ~5 mTorr and gradually heated to 400 ~ 700 °C with gas mixture: Ar/H₂ (40 vol % argon, 60 vol % H₂) at a flow rate of ~20 standard cubic centimeter per minute (sccm). The total pressure was maintained at ~200 mTorr during this temperature ramp. Hydrogen plasma was ignited at the power of 50W for 20 minutes after the heating step for planarization of the surface. Pure CH₄ (99.8%) with a flow rate of ~3 sccm was introduced into the growth chamber immediately after switching off the Ar/H₂ and plasma power of ~80W for 30 ~ 120 minutes. The samples were then cooled down to room temperature with a rate of 25 °C/min.

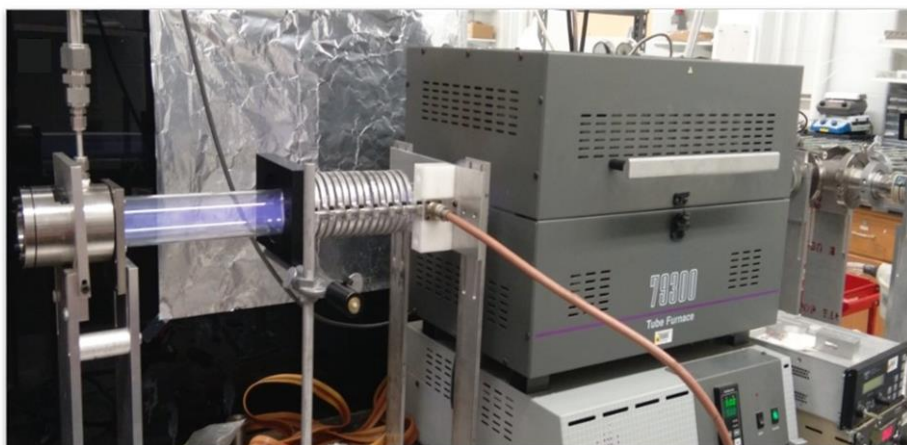
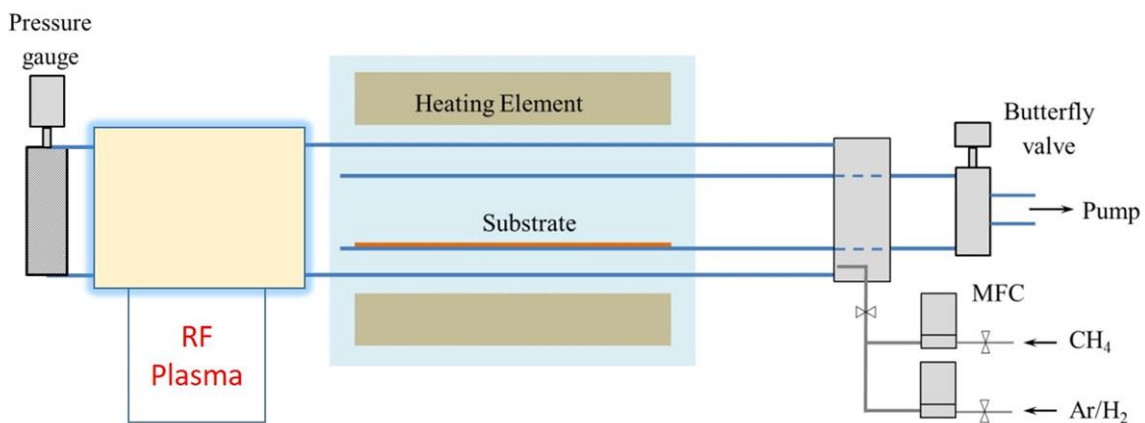


Figure 6.2 Home-made split ring radiofrequency plasma enhanced CVD system.

Electrical transport properties including four-probe resistance and thermopower (TEP) were measured by anchoring two miniature thermocouples (Chromel (KP)/Au-7 at%Fe (Au: Fe)) followed by two additional electrical concretions and a platinum resistive heater on the sample as described in Ref. [99]. The size of the tested samples was 1cm ×1cm square and the contacts were placed close to the corners of the samples. A closed cycle refrigerator (Janis Research Co. CCS-350ST-H) was used for low-temperature measurements. The Hall voltage (V_H) was measured in Hall probe configuration under +1, 0 and -1 T perpendicular magnetic fields produced by an electromagnet (LakeShore model EM4-CV 4-in. gap, Horizontal Field), and corrections were made for parasitic voltages by

averaging. An “Invia” Renishaw Raman spectrometer with 632 nm excitation wavelength was used for spectrum analysis. The microstructure and morphologies of the graphene samples were investigated using scanning electron microscopy (SEM) in Carl Zeiss FE-SEM Supra 35VP and transmission electron microscopy (TEM) with an FEI Tecnai F20 operated at 200 kV. The samples were transferred to the TEM grid by simply scraping off the substrates.

6.3 Surface characterization of PECVD graphene nanowalls

Surface characterization techniques are now available for measuring the shape, chemical, physical, and micromechanical properties. Because the surface plays a crucial role in many thermal, chemical, physical, and mechanical processes, such as oxidation, corrosion, adhesion, friction, wear, and erosion, these characterization techniques have established their importance in a number of scientific, industrial, and commercial fields.

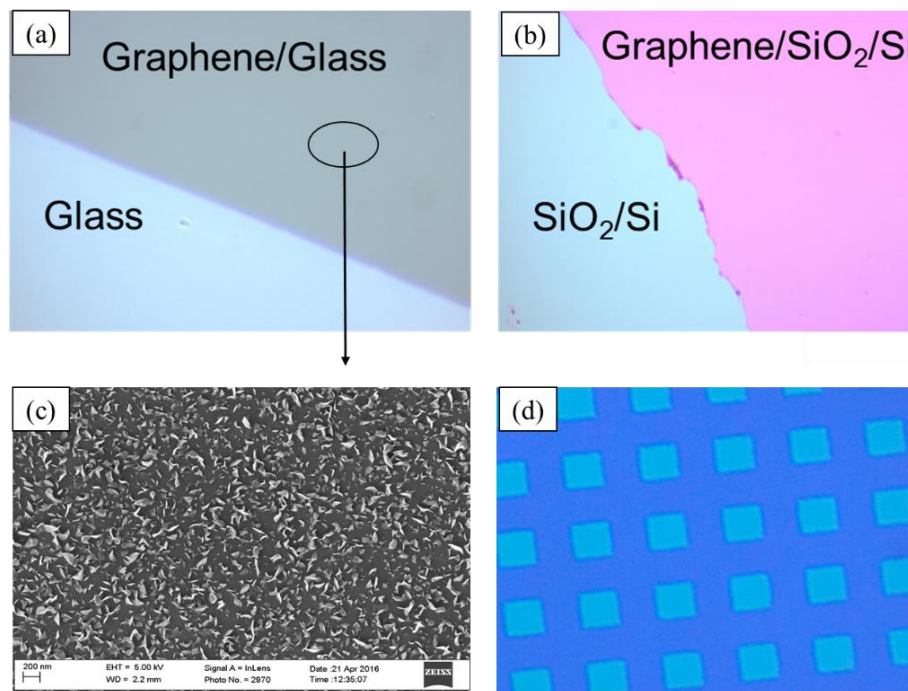


Figure 6.3 (a) Optical image of graphene nanowalls on glass substrate; (b) on SiO₂/Si wafer, (c) SEM image of graphene nanowalls on glass substrate, (d) pattern growth of graphene on SiO₂/Si wafer.

Here we characterized the surface of graphene nanowalls on different substrates by various techniques such as optical microscope, SEM, TEM and Raman spectrum. After the growth of graphene nanowalls, the coverage of these samples on different substrates was first investigated by optical microscopy. Figure 6.3 (a) and (b) show regions of glass and SiO₂/Si wafer with and without graphene nanowalls. This shows promise of obtaining patterned graphene nanowalls by placing shadow masks on the substrates during growth. Figure 6.3(d) shows a pattern of graphene nanowalls directly grown using a TEM grid as the mask. The darker regions contain well-separated areas of graphene nanowalls on SiO₂/Si wafer. The SEM image of the sample on glass in Figure 6.3 (c) clearly shows the vertical orientation of graphene nanowalls structures.

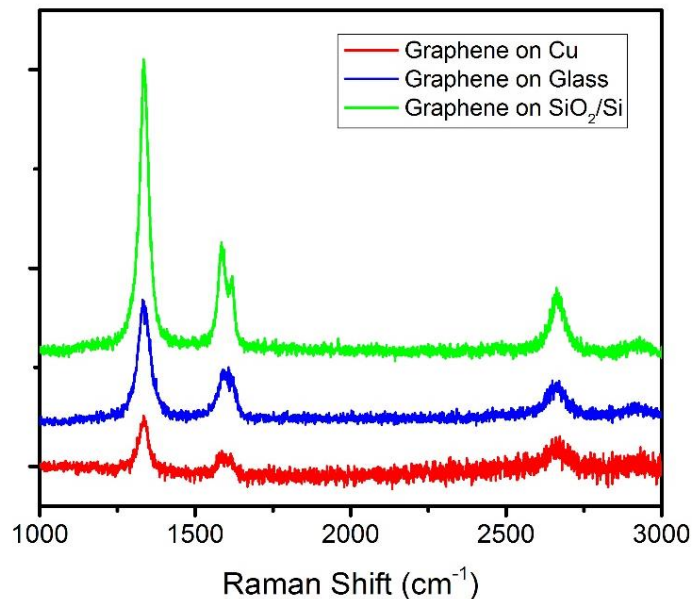


Figure 6.4 Raman spectra of graphene nanowalls on Cu, glass and SiO₂/Si substrates.

Figure 6.4 indicates the Raman spectra of the samples on three different substrates, viz., Cu foil, Si/SiO₂ wafer, and glass under the same growth condition. All these samples show typical features of graphene peaks include the D-band (around 1330 cm⁻¹) and D'-band (around 1630 cm⁻¹), associated with edges and structural disorder in graphene films [200]; G-band (around 1590 cm⁻¹), assigned to the sp² in-plane phonon vibrations and 2D-band (around 2670 cm⁻¹), indicated the formation of graphene [201-202]. We found that PECVD grown graphene nanowalls can be deposited on both conductive and insulated substrates with almost the same quality. Graphene nanowalls on glasses will be studied for electrical characterization.

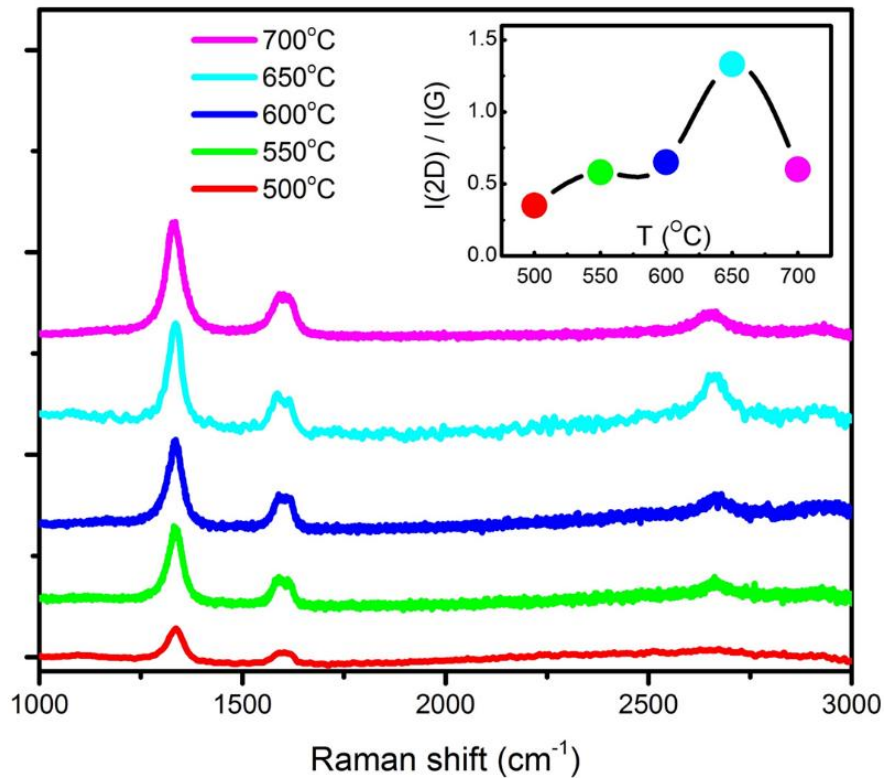


Figure 6.5 Raman spectra of the graphene nanowalls directly deposited on glass substrates at different growth temperature. The inset is the relative intensity ratio of I_{2D}/I_G.

Figure 6.5 shows the Raman spectrum of graphene nanowalls directly deposited on glasses at different growth temperature in the range of 500 °C to 700 °C. The inset shows the growth temperature dependence of the intensity ratio of 2D band and G band, $I(2D)/I(G)$. Each ample shows clear D, G, and D' bands, but the 2D band is only absent for the sample grown at 500 °C. However, the 2D band starts to grow gradually as the growth temperature increases to 650 °C where it maximizes. Interestingly, the intensity of the 2D band is seen to decrease for the sample grown at 700 °C. We believe that 650 °C is closer to the optimum growth temperature. Since the lower 2D band and higher D band reveal that the more disordered graphene growth, we believe that 650 °C is closer to the optimum growth temperature. The contribution to the D band which associated with breathing modes of the sp² atoms and activated by defect comes from edge effects due to the orientation of graphene and C-H bonds as out-of-plane defects.

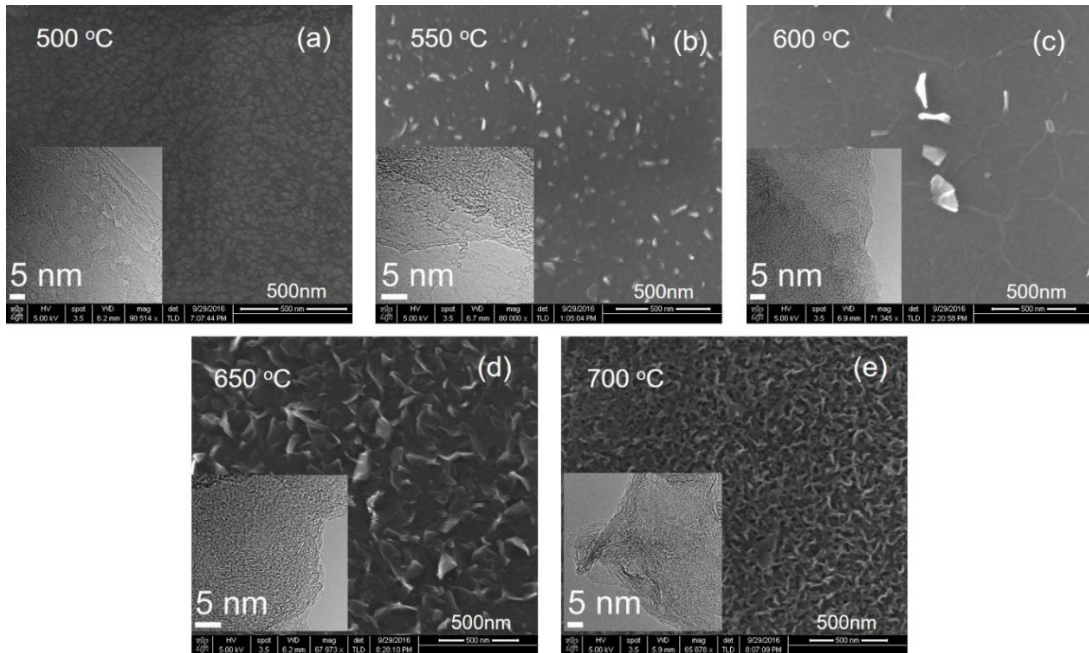


Figure 6.6 SEM images for the graphene nanowalls directly deposited on glass substrate at different growth temperatures.

The morphologies of different samples were investigated by SEM and TEM. Figure 6.6 (a-e) show the graphene nanowalls obtained on glass substrates with various deposition temperatures. The inset of each image represents the HRTEM image of the representative sample. Figure 6.6 (a) shows few layer graphene films of different sizes deposited on the glass substrate. The insufficient temperature and uneven surface of glass with different energy barriers are believed to make the film deposition discontinuous. Figure 6.6 (b) shows the formation of vertically oriented graphene flakes grown at a higher temperature. Thermodynamic factors including temperature, pressure and the Gibbs free energy are known to dictate the direction and limitation of the reaction. In CVD process of graphene, the growth is affected by both thermodynamics factors and kinetics factors. In the PECVD process, sufficiently high energies break down methane into solid carbon and hydrogen gas, then dissociated into various active groups of carbonaceous species. The thermal energy corresponding to 500 °C - 700 °C in our work can aid accumulation of charged carbonaceous ions and accelerate their surface diffusion. With time, the graphene grains coalesce with each other and stack onto polycrystalline films. Various growth temperatures lead to different deposition rates on the substrate. Lower thermal energy tends to slow down the deposition rate which in turn reduces the possibility of vertical growth. As the temperature increases, higher deposition rate results in the island growth of graphene rather than layer by layer growth. These island growth of graphene was possibly attributed to the high surface mobility of incoming carbon-bearing species, and plasma electric field oriented perpendicular to the substrate surface [203]. This phenomenon has also been reported previously in the catalyst-free growth of graphene by PECVD on insulating substrates such as SiO₂ and glass [199, 204].

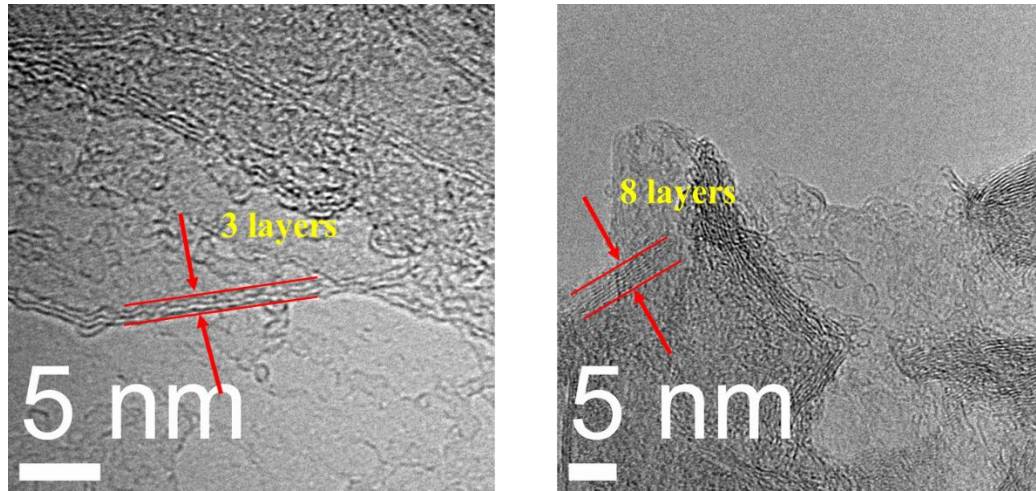


Figure 6.7 HRTEM image of graphene nanowalls synthesized at different temperature, left: 550 °C, right: 650 °C.

Higher substrate temperature usually offers more species for nucleation and thus benefits graphene growth rate. From the SEM images, it is clearly shown a low density of these vertically grown graphene and a relatively low growth rate when the temperature was less than 600 °C. With increasing the temperature, the density of this vertical growth started to increase rapidly with almost covering the entire surface when the growth temperature reached 700 °C, as well as the increasing number of layers of graphene flakes as shown in Figure 6.7.

6.4 Electronic properties of PECVD graphene nanowalls

The temperature dependence of 4-probe resistance of each sample grown at varying temperatures is shown in Figure 6.8 (a). For PECVD graphene nanowalls, electrical transport is expected to be governed partly by hopping conduction and thermally activated conduction mechanisms. Assuming the possibility of 2D-VRH conduction in our system,

we fitted $R(T)$ dependence by the the classical law for variable range hopping (VRH) $R = R_0 \exp(T_0/T)^{1/3}$, where $T_0 = 13.8/(k_B N(E_F) \xi^2)$, k_B is the Boltzmann constant, $N(E_F)$ is the density of states at the Fermi energy, and ξ is the localization length [205]. From the fitted parameters the localization length ξ can be evaluated by $\xi = [13.8/(k_B N(E_F) T_0)]^{1/2}$ with the density of states of graphene $N(E) = (2E/(\pi \hbar^2 v_F^2))$ (assuming $v_F \sim 1 \times 10^6$ m/s) and the carrier density $n = E_F^2/(2\pi \hbar^2 v_F^2)$ which can be calculated from conductivity and Hall measurements.

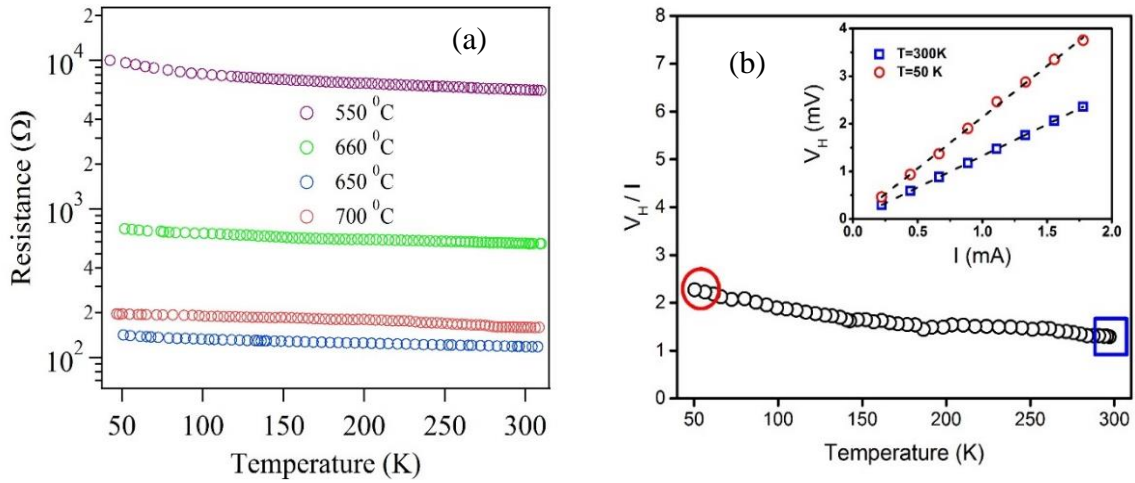


Figure 6.8 (a) Temperature dependence of 4-probe resistance for graphene nanowalls grown at varying temperatures (b) Temperature dependence of Hall voltage over excitation current, V_H/I for graphene on glass at 650 °C. The inset shows V_H vs I curve at 300 K and 50 K.

Using Hall voltage (V_H) and sheet resistance (R_s), sheet carrier density n_s , carrier mobility μ_s and localization length ξ at room temperature were calculated as follows:

$$n_s = \frac{IB}{V_H e} = \frac{0.8 \times 10^{-4}}{1.5 \times 1.6 \times 10^{-19}} = 3.3 \times 10^{14} \text{ cm}^{-2}$$

$$E_F = \sqrt{2\pi n \hbar v_F}$$

$$N(E_F) = \frac{\sqrt{8\pi n}}{\pi \hbar v_F} = 2.75 \times 10^{33}$$

$$\mu_s = \frac{1}{en_s R_S} = \frac{1}{1.6 \times 10^{-19} \times 3.3 \times 10^{14} \times 150} = 125 \text{ cm}^2 \text{ V}^{-1} \text{ s}^{-1}$$

$$\xi = \sqrt{\frac{13.8}{k_B N(E_F) T_0}} = \sqrt{\frac{13.8}{1.38 \times 10^{-23} \times 2.75 \times 10^{33} \times T_0}}$$

The localization length $\xi = 34\text{nm}$, 101nm , 191nm , 149nm for growth temperatures 550°C , 600°C , 650°C and 700°C , respectively.

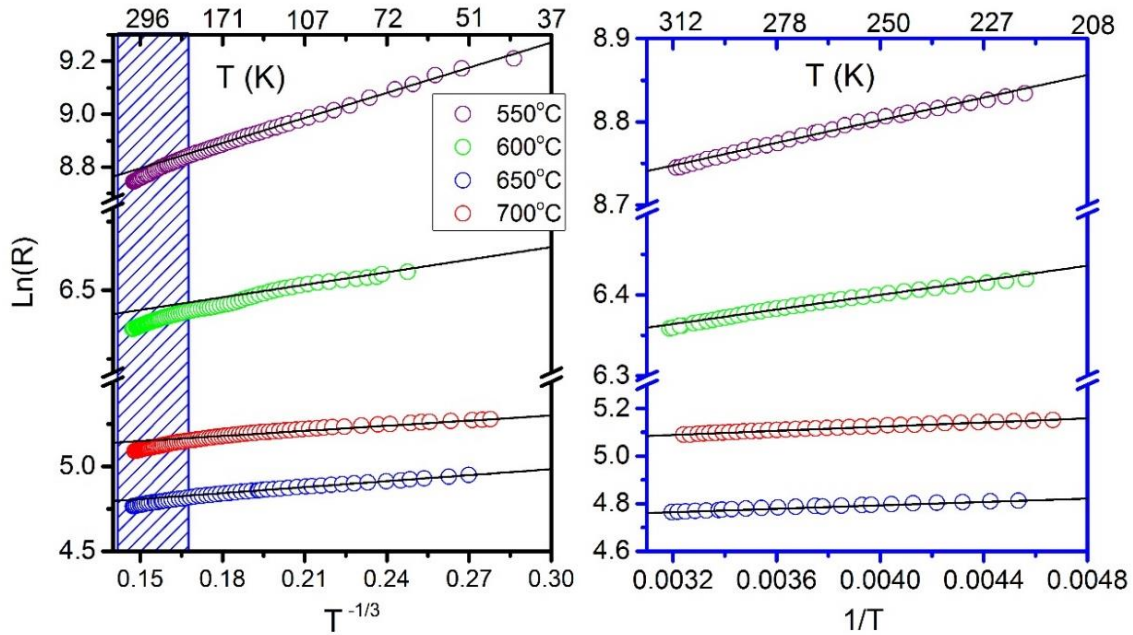


Figure 6.9 Best fits (black curves) of temperature dependent resistance for graphene on glass deposited at different temperatures (a) Best fits for VRH model at low temperatures (b) Best fits for TA model at high temperatures.

In this context, we plot logarithmic R , $\log(R)$ vs $T^{-1/3}$ for low temperatures as shown in Figure 6.9 (a). It is evident from the plot that the data fit very well with the 2-D VRH theory for low temperature regime (below ~ 210 K). For high temperature regime ($210 \sim 300$ K), thermal activated conduction model well fits the experimental data as shown in Figure 6.9 (b). However, the data is seen to deviate from the VRH model for high temperatures (due to the fact that thermal excitation of charge carriers becoming more dominant) and obey thermally activated T^{-1} behavior as shown in Figure 6.9 (b). For higher temperatures > 210 K, $\text{Log}(R)$ data is well fitted with T^{-1} dependence. This T^{-1} dependence of $\text{Log}(R)$ can be interpreted as due to thermal activation at the mid-gap states in the graphene nanowalls contributing to the carrier transport properties. The contribution of the thermally activated (TA) conduction reflects the fact that phonon scattering is observed in the PECVD graphene nanowalls. The characteristics of $\text{Log}(R)$ at high temperature can be fitted by the sum of the 2D-VRH ($R = R_0 \exp(T_0/T)^{1/3}$) and TA conduction ($R = R_0 \exp(E_A/k_B T)$, where E_A is the activation energy). The combination of the 2D-VRH and TA conduction has been observed in some disordered systems, such as amorphous semiconductors in bulk materials [206]. This is the first observation of transport properties explained by the sum of the 2D-VRH and TA conduction in graphene nanowalls directly deposited on glass via PECVD.

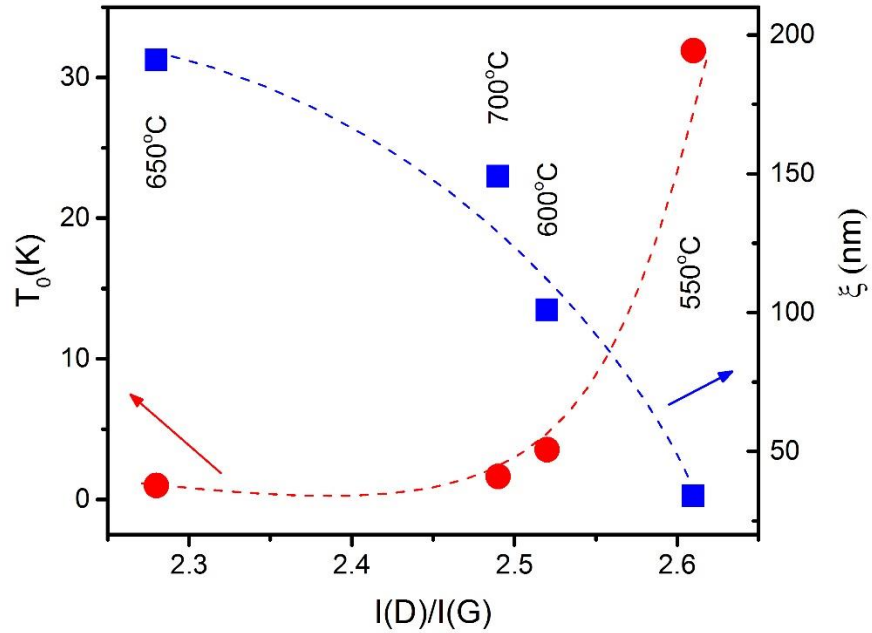


Figure 6.10 T_0 values (extracted from VRH fitting to resistance data) for each synthesis temperature vs. $I(D)/I(G)$ ratio. The ξ localization lengths are plotted in the right-hand axis.

Figure 6.10 shows the T_0 (left axis) extracted from VRH analysis at low temperatures as a function of $I(D)/I(G)$ ratio which represent the quality of graphene related to the growth temperature. For the lowest growth temperature (550 °C), T_0 remains large (> 30 K), and starts to decrease as the growth temperature increases showing a minimum at 650 °C. The localization length, ξ for each growth temperature is shown on the right axis of Figure 6.10. The value of ξ was found to vary from 35 nm to 150 nm within the growth temperature window of 550 °C-700 °C, respectively.

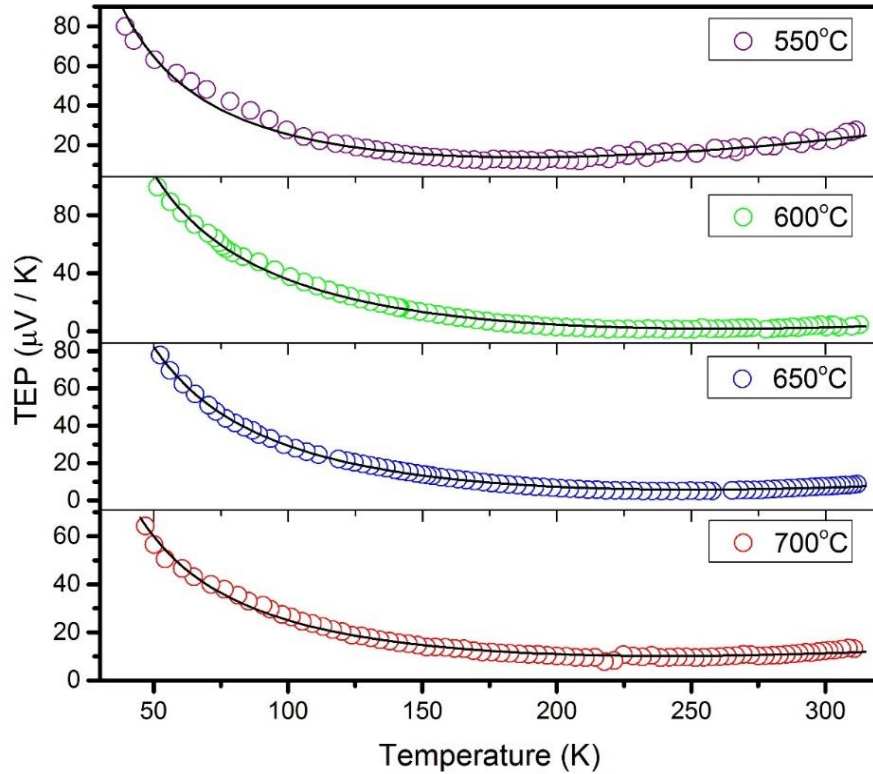


Figure 6.11 Best fits (black curves) of temperature dependent TEP for graphene nanowalls on glass deposited at different temperatures.

Thermopower is another important transport property of great interest in graphene since it is sensitive to the composition and structure of the system and to the external stimuli. Figure 6.11 shows the temperature dependence of the TEP for the graphene nanowalls grown at temperatures, 550 °C, 600 °C, 650 °C, and 700 °C. All the samples show positive TEP values in the range 5-20 $\mu\text{V}/\text{K}$ at room temperature. However, this temperature dependence is rather anomalous compared to graphene grown under conventional CVD techniques where TEP shows linear temperature dependence. Here, as the temperature decreases, TEP is seen to decrease linearly down to ~ 220 K, but below ~ 220 K, all the samples show an anomalous behavior with a rapid increase in TEP with further lowering of temperature. The diffusion thermopower, S_d is usually expressed as a function of

temperature and carrier concentration by Mott expression [207], $S_d = (\pi^2 k^2 T / 3e) [d \ln(\sigma) / dE]_{E=E_F}$, where σ is the energy-dependent conductivity that does not vary with temperature. Therefore, S_d should be a linear function of temperature simply written as $S_d = S_1 T$. The low temperature behavior below ~ 220 K with a rapid increase in TEP is represented with a term proportional to $1/T$ as in a semiconductor [208]. Hence, we fitted the temperature dependence of TEP with the equation given by $S(T) = S_1 T + S_2 / T + S_3$. Figure 6.11 shows the best fits of data for this equation. Details of the fitting parameters have been shown in table 4.

Table 4. Fitted parameters for graphene samples on glass at varying growth temperatures.

Temperature	I(D)/I(G)	T_0	ξ (nm)	S_1	S_2
550°C	2.62	31.9	34	0.14	4687
600°C	2.53	3.5	101	0.10	7974
650°C	2.28	1.0	191	0.09	5968
700°C	2.47	1.6	149	0.06	3837

It should be noted that for the range of temperatures considered ($30 < T < 300$ K), various scattering mechanisms are expected to influence the diffusion TEP of graphene. The scattering mechanisms include acoustic phonons, optical phonons via optical deformation potential, surface roughness, charged impurities via long-range Coulomb interaction and vacancies in the system [209]. However, the observed temperature dependence can only be explained by $1/T$ temperature dependence, which requires further investigation.

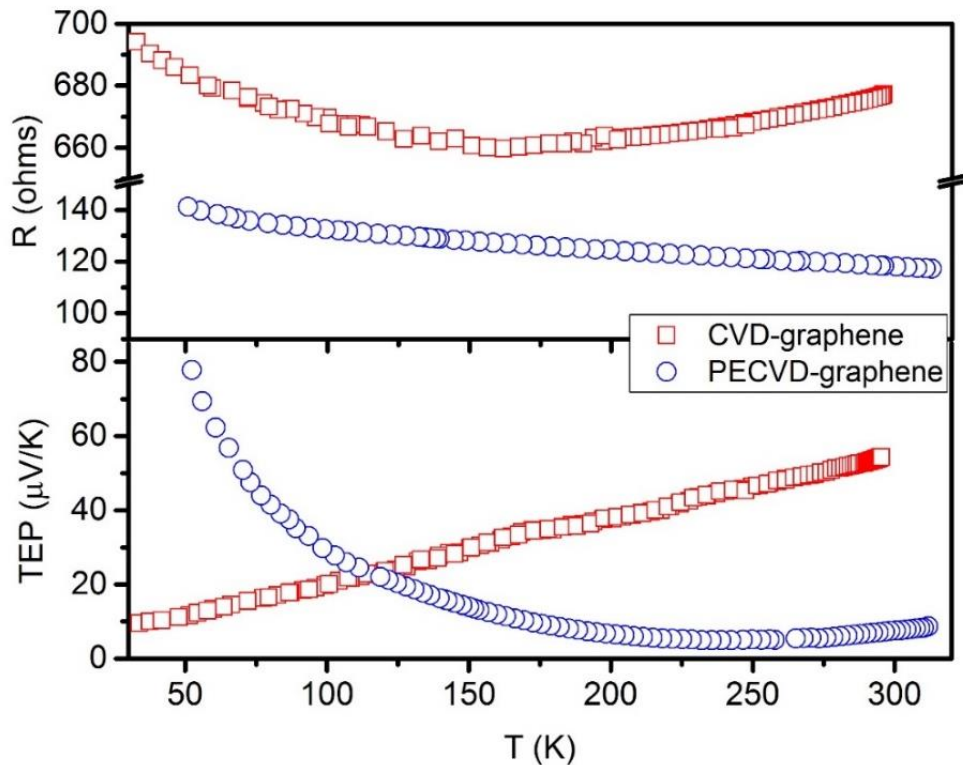


Figure 6.12 Comparison of 4-probe resistance (top) and thermopower (bottom) of CVD graphene grown on copper foils at 1000 °C and PECVD graphene nanowalls grown on glass at 600 °C.

Finally, Figure 6.12 compares the transport properties of graphene nanowalls grown on copper foils by conventional CVD techniques at 1000 °C with that of samples directly grown on glass substrates at lower temperatures by PECVD. Thermal CVD derived graphene shows an initial decrease of 4-probe resistance when the temperature decreases (metallic) followed by an increase in R for further decrease in temperature. In contrast, PECVD graphene nanowalls show negative temperature coefficient of resistance in the entire temperature region. The sheet resistance of this pristine graphene synthesized via

CVD and then transferred from Cu foil to glass substrate was calculated in our previous work, which is $R_s = 880 \text{ } \Omega/\text{sq}$ [153]. The other recently reported growth of graphene by CVD with subsequent transfer onto bendable substrates enabled the production of large area graphene film with $R_s = 275 \text{ } \Omega/\text{sq}$ for single layer and $\sim 40 \text{ } \Omega/\text{sq}$ for four-layer graphene films after p-type doping with HNO_3 [210]. For our results, the sheet resistance of the graphene nanowalls directly deposited on glass substrates by PECVD can reach $\sim 100 \text{ } \Omega/\text{sq}$ which is believed to be more effective than conventional CVD method. Meanwhile, the thermopower of thermal CVD derived graphene shows linear metallic temperature dependence while all the PECVD grown graphene nanowalls show initial decrease of thermopower at high temperatures, but starts to increase with further decrease of temperature.

6.5 Conclusion

In summary, we have successfully developed a low temperature process to deposit graphene nanowalls directly on amorphous insulating glass surface, also on SiO_2/Si wafers, Cu and Ni foil by PECVD. The morphological properties of the graphene samples on glass show the formation of vertically oriented graphene flakes. The temperature dependence of electrical transport properties including resistivity and thermopower were studied in the temperature range, 30-300 K. The fitted results show the combination of the 2D-Variable Range Hopping (VRH) at low temperature and Thermally Activated (TA) conduction mechanisms at temperatures over 210 K. We believe this approach would be a significant step in future graphene electronics due to low-cost growth directly on arbitrary substrates as well as avoidance of the inconvenient post-growth transfer processes commonly used.

REFERENCES

1. Low, J. X.; Cao, S. W.; Yu, J. G.; Wageh, S., Two-dimensional layered composite photocatalysts. *Chem Commun* **2014**, 50 (74), 10768-10777.
2. Fradkin, E., Critical-Behavior of Disordered Degenerate Semiconductors .2. Spectrum and Transport-Properties in Mean-Field Theory. *Physical Review B* **1986**, 33 (5), 3263-3268.
3. Novoselov, K. S.; Geim, A. K.; Morozov, S. V.; Jiang, D.; Zhang, Y.; Dubonos, S. V.; Grigorieva, I. V.; Firsov, A. A., Electric field effect in atomically thin carbon films. *Science* **2004**, 306 (5696), 666-669.
4. Wallace, P. R., The Band Theory of Graphite. *Phys. Rev.* **1947**, 72 (3), 258.
5. Castro Neto, A. H.; Guinea, F.; Peres, N. M. R.; Novoselov, K. S.; Geim, A. K., The electronic properties of graphene. *Reviews of Modern Physics* **2009**, 81 (1), 109-162.
6. Brenner, D. W.; Shenderova, O. A.; Harrison, J. A.; Stuart, S. J.; Ni, B.; Sinnott, S. B., A second-generation reactive empirical bond order (REBO) potential energy expression for hydrocarbons. *J Phys-Condens Mat* **2002**, 14 (4), 783-802.
7. Lee, C.; Wei, X. D.; Kysar, J. W.; Hone, J., Measurement of the elastic properties and intrinsic strength of monolayer graphene. *Science* **2008**, 321 (5887), 385-388.
8. Du, X.; Skachko, I.; Barker, A.; Andrei, E. Y., Approaching ballistic transport in suspended graphene. *Nature Nanotechnology* **2008**, 3 (8), 491-495.

9. Zhang, Y. B.; Tan, Y. W.; Stormer, H. L.; Kim, P., Experimental observation of the quantum Hall effect and Berry's phase in graphene. *Nature* **2005**, *438* (7065), 201-204.
10. Wu, X. S.; Hu, Y. K.; Ruan, M.; Madiomanana, N. K.; Hankinson, J.; Sprinkle, M.; Berger, C.; de Heer, W. A., Half integer quantum Hall effect in high mobility single layer epitaxial graphene. *Applied Physics Letters* **2009**, *95* (22).
11. Zomer, P. J.; Guimaraes, M. H. D.; Tombros, N.; van Wees, B. J., Long-distance spin transport in high-mobility graphene on hexagonal boron nitride. *Physical Review B* **2012**, *86* (16).
12. Ghosh, S.; Bao, W. Z.; Nika, D. L.; Subrina, S.; Pokatilov, E. P.; Lau, C. N.; Balandin, A. A., Dimensional crossover of thermal transport in few-layer graphene. *Nature Materials* **2010**, *9* (7), 555-558.
13. Pop, E.; Varshney, V.; Roy, A. K., Thermal properties of graphene: Fundamentals and applications. *Mrs Bull* **2012**, *37* (12), 1273-1281.
14. Kim, K. S.; Zhao, Y.; Jang, H.; Lee, S. Y.; Kim, J. M.; Kim, K. S.; Ahn, J. H.; Kim, P.; Choi, J. Y.; Hong, B. H., Large-scale pattern growth of graphene films for stretchable transparent electrodes. *Nature* **2009**, *457* (7230), 706-710.
15. Chen, J. H.; Jang, C.; Xiao, S. D.; Ishigami, M.; Fuhrer, M. S., Intrinsic and extrinsic performance limits of graphene devices on SiO₂. *Nature Nanotechnology* **2008**, *3* (4), 206-209.
16. Murali, R.; Yang, Y. X.; Brenner, K.; Beck, T.; Meindl, J. D., Breakdown current density of graphene nanoribbons. *Applied Physics Letters* **2009**, *94* (24).

17. Nair, R. R.; Blake, P.; Grigorenko, A. N.; Novoselov, K. S.; Booth, T. J.; Stauber, T.; Peres, N. M. R.; Geim, A. K., Fine structure constant defines visual transparency of graphene. *Science* **2008**, *320* (5881), 1308-1308.
18. Bao, Q. L.; Loh, K. P., Graphene Photonics, Plasmonics, and Broadband Optoelectronic Devices. *Acs Nano* **2012**, *6* (5), 3677-3694.
19. Khan, U.; Kim, T. H.; Ryu, H.; Seung, W.; Kim, S. W., Graphene Tribotronics for Electronic Skin and Touch Screen Applications. *Adv Mater* **2017**, *29* (1).
20. Kuhn, L.; Gorji, N. E., Review on the graphene/nanotube application in thin film solar cells. *Mater Lett* **2016**, *171*, 323-326.
21. Ubani, C. A.; Ibrahim, M. A.; Teridi, M. A. M.; Sopian, K.; Ali, J.; Chaudhary, K. T., Application of graphene in dye and quantum dots sensitized solar cell. *Sol Energy* **2016**, *137*, 531-550.
22. Lancellotti, L.; Polichetti, T.; Ricciardella, F.; Tari, O.; Gnanapragasam, S.; Daliento, S.; Di Francia, G., Graphene applications in Schottky barrier solar cells. *Thin Solid Films* **2012**, *522*, 390-394.
23. Radhakrishnan, G.; Cardema, J. D.; Adams, P. M.; Kim, H. I.; Foran, B., Fabrication and Electrochemical Characterization of Single and Multi-Layer Graphene Anodes for Lithium-Ion Batteries. *J Electrochem Soc* **2012**, *159* (6), A752-A761.
24. Stoller, M. D.; Park, S. J.; Zhu, Y. W.; An, J. H.; Ruoff, R. S., Graphene-Based Ultracapacitors. *Nano Letters* **2008**, *8* (10), 3498-3502.

25. Kwak, Y. H.; Choi, D. S.; Kim, Y. N.; Kim, H.; Yoon, D. H.; Ahn, S. S.; Yang, J. W.; Yang, W. S.; Seo, S., Flexible glucose sensor using CVD-grown graphene-based field effect transistor. *Biosens Bioelectron* **2012**, *37* (1), 82-87.
26. Sun, L.; Li, S. S.; Ding, W.; Yao, Y. W.; Yang, X. Y.; Yao, C., Fluorescence detection of cholesterol using a nitrogen-doped graphene quantum dot/chromium picolinate complex-based sensor. *J Mater Chem B* **2017**, *5* (45), 9006-9014.
27. Sharma, A. K.; Gupta, J., Graphene based chalcogenide fiber-optic evanescent wave sensor for detection of hemoglobin in human blood. *Opt Fiber Technol* **2018**, *41*, 125-130.
28. Kilic, T.; Erdem, A.; Erac, Y.; Seydibeyoglu, M. O.; Okur, S.; Ozsoz, M., Electrochemical Detection of a Cancer Biomarker mir-21 in Cell Lysates Using Graphene Modified Sensors. *Electroanal* **2015**, *27* (2), 317-326.
29. Zhang, X.; Rajaraman, B. R. S.; Liu, H. H.; Ramakrishna, S., Graphene's potential in materials science and engineering. *Rsc Adv* **2014**, *4* (55), 28987-29011.
30. Tour, J. M., Top-Down versus Bottom-Up Fabrication of Graphene-Based Electronics. *Chem Mater* **2014**, *26* (1), 163-171.
31. Allen, M. J.; Tung, V. C.; Kaner, R. B., Honeycomb Carbon: A Review of Graphene. *Chem Rev* **2010**, *110* (1), 132-145.
32. Park, S.; Ruoff, R. S., Chemical methods for the production of graphenes. *Nature Nanotechnology* **2009**, *4* (4), 217-224.
33. Chen, X. P.; Zhang, L. L.; Chen, S. S., Large area CVD growth of graphene. *Synthetic Met* **2015**, *210*, 95-108.

34. Jiao, L. Y.; Wang, X. R.; Diankov, G.; Wang, H. L.; Dai, H. J., Facile synthesis of high-quality graphene nanoribbons. *Nature Nanotechnology* **2010**, *5* (5), 321-325.
35. Jiao, L. Y.; Zhang, L.; Wang, X. R.; Diankov, G.; Dai, H. J., Narrow graphene nanoribbons from carbon nanotubes. *Nature* **2009**, *458* (7240), 877-880.
36. Kosynkin, D. V.; Higginbotham, A. L.; Sinitskii, A.; Lomeda, J. R.; Dimiev, A.; Price, B. K.; Tour, J. M., Longitudinal unzipping of carbon nanotubes to form graphene nanoribbons. *Nature* **2009**, *458* (7240), 872-U5.
37. Xin, G. Q.; Hwang, W.; Kim, N.; Cho, S. M.; Chae, H., A graphene sheet exfoliated with microwave irradiation and interlinked by carbon nanotubes for high-performance transparent flexible electrodes. *Nanotechnology* **2010**, *21* (40).
38. Bhuyan, M. S. A.; Uddin, M. N.; Islam, M. M.; Bipasha, F. A.; Hossain, S. S., Synthesis of graphene. *Int Nano Lett* **2016**, *6* (2), 65-83.
39. Zhang, Y. B.; Small, J. P.; Pontius, W. V.; Kim, P., Fabrication and electric-field-dependent transport measurements of mesoscopic graphite devices. *Applied Physics Letters* **2005**, *86* (7).
40. Novoselov, K. S.; Geim, A. K.; Morozov, S. V.; Jiang, D.; Katsnelson, M. I.; Grigorieva, I. V.; Dubonos, S. V.; Firsov, A. A., Two-dimensional gas of massless Dirac fermions in graphene. *Nature* **2005**, *438* (7065), 197-200.
41. Ci, L. J.; Song, L.; Jariwala, D.; Elias, A. L.; Gao, W.; Terrones, M.; Ajayan, P. M., Graphene Shape Control by Multistage Cutting and Transfer. *Adv Mater* **2009**, *21* (44), 4487-+.
42. Liang, X. G.; Chang, A. S. P.; Zhang, Y. G.; Harteneck, B. D.; Choo, H.; Olynick, D. L.; Cabrini, S., Electrostatic Force Assisted Exfoliation of Prepatterned Few-

- Layer Graphenes into Device Sites (vol 9, pg 467, 2009). *Nano Letters* **2009**, *9* (2), 919-919.
43. Liang, X.; Fu, Z.; Chou, S. Y., Graphene transistors fabricated via transfer-printing in device active-areas on large wafer. *Nano Letters* **2007**, *7* (12), 3840-3844.
44. Chen, J. H.; Ishigami, M.; Jang, C.; Hines, D. R.; Fuhrer, M. S.; Williams, E. D., Printed graphene circuits. *Adv Mater* **2007**, *19* (21), 3623-3629.
45. Dasari, B. L.; Nouri, J. M.; Brabazon, D.; Naher, S., Graphene and derivatives - Synthesis techniques, properties and their energy applications. *Energy* **2017**, *140*, 766-778.
46. Coleman, J. N., Liquid Exfoliation of Defect-Free Graphene. *Accounts Chem Res* **2013**, *46* (1), 14-22.
47. Ciesielski, A.; Samori, P., Graphene via sonication assisted liquid-phase exfoliation. *Chemical Society Reviews* **2014**, *43* (1), 381-398.
48. Ciesielski, A.; Samori, P., Supramolecular Approaches to Graphene: From Self-Assembly to Molecule-Assisted Liquid-Phase Exfoliation. *Adv Mater* **2016**, *28* (29), 6030-6051.
49. Hernandez, Y.; Nicolosi, V.; Lotya, M.; Blighe, F. M.; Sun, Z. Y.; De, S.; McGovern, I. T.; Holland, B.; Byrne, M.; Gun'ko, Y. K.; Boland, J. J.; Niraj, P.; Duesberg, G.; Krishnamurthy, S.; Goodhue, R.; Hutchison, J.; Scardaci, V.; Ferrari, A. C.; Coleman, J. N., High-yield production of graphene by liquid-phase exfoliation of graphite. *Nature Nanotechnology* **2008**, *3* (9), 563-568.

50. Hamilton, C. E.; Lomeda, J. R.; Sun, Z. Z.; Tour, J. M.; Barron, A. R., High-Yield Organic Dispersions of Unfunctionalized Graphene. *Nano Letters* **2009**, *9* (10), 3460-3462.
51. Li, X. L.; Zhang, G. Y.; Bai, X. D.; Sun, X. M.; Wang, X. R.; Wang, E.; Dai, H. J., Highly conducting graphene sheets and Langmuir-Blodgett films. *Nature Nanotechnology* **2008**, *3* (9), 538-542.
52. Wu, C. X.; Li, F. S.; Wu, W.; Chen, W.; Guo, T. L., Liquid-phase exfoliation of chemical vapor deposition-grown single layer graphene and its application in solution-processed transparent electrodes for flexible organic light-emitting devices. *Applied Physics Letters* **2014**, *105* (24).
53. Torrisi, F.; Hasan, T.; Wu, W. P.; Sun, Z. P.; Lombardo, A.; Kulmala, T. S.; Hsieh, G. W.; Jung, S. J.; Bonaccorso, F.; Paul, P. J.; Chu, D. P.; Ferrari, A. C., Inkjet-Printed Graphene Electronics. *Acs Nano* **2012**, *6* (4), 2992-3006.
54. Desai, J. A.; Biswas, C.; Kaul, A. B., Inkjet printing of liquid-exfoliated, highly conducting graphene/poly(3,4 ethylenedioxythiophene): poly(styrenesulfonate) nanosheets for organic electronics. *J Vac Sci Technol B* **2017**, *35* (3).
55. Srivastava, P. K.; Yadav, P.; Ghosh, S., Dielectric environment as a factor to enhance the production yield of solvent exfoliated graphene. *Rsc Adv* **2015**, *5* (79), 64395-64403.
56. Berger, C.; Song, Z. M.; Li, X. B.; Wu, X. S.; Brown, N.; Naud, C.; Mayou, D.; Li, T. B.; Hass, J.; Marchenkov, A. N.; Conrad, E. H.; First, P. N.; de Heer, W. A., Electronic confinement and coherence in patterned epitaxial graphene. *Science* **2006**, *312* (5777), 1191-1196.

57. Jernigan, G. G.; VanMil, B. L.; Tedesco, J. L.; Tischler, J. G.; Glaser, E. R.; Davidson, A.; Campbell, P. M.; Gaskill, D. K., Comparison of Epitaxial Graphene on Si-face and C-face 4H SiC Formed by Ultrahigh Vacuum and RF Furnace Production. *Nano Letters* **2009**, *9* (7), 2605-2609.
58. Norimatsu, W.; Kusunoki, M., Epitaxial graphene on SiC{0001}: advances and perspectives. *Physical Chemistry Chemical Physics* **2014**, *16* (8), 3501-3511.
59. Hummers, W. S.; Offeman, R. E., Preparation of Graphitic Oxide. *Journal of the American Chemical Society* **1958**, *80* (6), 1339-1339.
60. Becerril, H. A.; Mao, J.; Liu, Z.; Stoltenberg, R. M.; Bao, Z.; Chen, Y., Evaluation of solution-processed reduced graphene oxide films as transparent conductors. *ACS Nano* **2008**, *2* (3), 463-470.
61. Bourlinos, A. B.; Gournis, D.; Petridis, D.; Szabo, T.; Szeri, A.; Dekany, I., Graphite oxide: Chemical reduction to graphite and surface modification with primary aliphatic amines and amino acids. *Langmuir* **2003**, *19* (15), 6050-6055.
62. Wang, G. X.; Yang, J.; Park, J.; Gou, X. L.; Wang, B.; Liu, H.; Yao, J., Facile synthesis and characterization of graphene nanosheets. *J Phys Chem C* **2008**, *112* (22), 8192-8195.
63. Dua, V.; Surwade, S. P.; Ammu, S.; Agnihotra, S. R.; Jain, S.; Roberts, K. E.; Park, S.; Ruoff, R. S.; Manohar, S. K., All-Organic Vapor Sensor Using Inkjet-Printed Reduced Graphene Oxide. *Angew Chem Int Edit* **2010**, *49* (12), 2154-2157.
64. Stankovich, S.; Dikin, D. A.; Piner, R. D.; Kohlhaas, K. A.; Kleinhammes, A.; Jia, Y.; Wu, Y.; Nguyen, S. T.; Ruoff, R. S., Synthesis of graphene-based nanosheets

- via chemical reduction of exfoliated graphite oxide. *Carbon* **2007**, *45* (7), 1558-1565.
65. McAllister, M. J.; Li, J. L.; Adamson, D. H.; Schniepp, H. C.; Abdala, A. A.; Liu, J.; Herrera-Alonso, M.; Milius, D. L.; Car, R.; Prud'homme, R. K.; Aksay, I. A., Single sheet functionalized graphene by oxidation and thermal expansion of graphite. *Chem Mater* **2007**, *19* (18), 4396-4404.
66. Behura, S. K.; Nayak, S.; Mukhopadhyay, I.; Jani, O., Junction characteristics of chemically-derived graphene/p-Si heterojunction solar cell. *Carbon* **2014**, *67*, 766-774.
67. Duan, H. G.; Xie, E. Q.; Han, L.; Xu, Z., Turning PMMA nanofibers into graphene nanoribbons by in situ electron beam irradiation. *Adv Mater* **2008**, *20* (17), 3284-+.
68. Subrahmanyam, K. S.; Panchakarla, L. S.; Govindaraj, A.; Rao, C. N. R., Simple Method of Preparing Graphene Flakes by an Arc-Discharge Method. *J Phys Chem C* **2009**, *113* (11), 4257-4259.
69. Wu, Z. S.; Ren, W. C.; Gao, L. B.; Zhao, J. P.; Chen, Z. P.; Liu, B. L.; Tang, D. M.; Yu, B.; Jiang, C. B.; Cheng, H. M., Synthesis of Graphene Sheets with High Electrical Conductivity and Good Thermal Stability by Hydrogen Arc Discharge Exfoliation. *Acs Nano* **2009**, *3* (2), 411-417.
70. Ileri, N.; Goldman, N., Graphene and nano-diamond synthesis in expansions of molten liquid carbon. *J Chem Phys* **2014**, *141* (16).
71. Lee, H. C.; Liu, W. W.; Chai, S. P.; Mohamed, A. R.; Aziz, A.; Khe, C. S.; Hidayah, N. M. S.; Hashim, U., Review of the synthesis, transfer, characterization and

- growth mechanisms of single and multilayer graphene (vol 7, pg 15644, 2017). *Rsc Adv* **2017**, 7 (45), 28427-28427.
72. Yu, Q. K.; Lian, J.; Siriponglert, S.; Li, H.; Chen, Y. P.; Pei, S. S., Graphene segregated on Ni surfaces and transferred to insulators. *Applied Physics Letters* **2008**, 93 (11).
73. Reina, A.; Thiele, S.; Jia, X. T.; Bhaviripudi, S.; Dresselhaus, M. S.; Schaefer, J. A.; Kong, J., Growth of Large-Area Single- and Bi-Layer Graphene by Controlled Carbon Precipitation on Polycrystalline Ni Surfaces. *Nano Research* **2009**, 2 (6), 509-516.
74. McCarty, K. F.; Feibelman, P. J.; Loginova, E.; Bartelt, N. C., Kinetics and thermodynamics of carbon segregation and graphene growth on Ru(0001). *Carbon* **2009**, 47 (7), 1806-1813.
75. Thangaraja, A.; Shinde, S. M.; Kalita, G.; Papon, R.; Sharma, S.; Vishwakarma, R.; Sharma, K. P.; Tanemura, M., Structure dependent hydrogen induced etching features of graphene crystals. *Applied Physics Letters* **2015**, 106 (25).
76. Sutter, P. W.; Flege, J. I.; Sutter, E. A., Epitaxial graphene on ruthenium. *Nature Materials* **2008**, 7 (5), 406-411.
77. Ueta, H.; Saida, M.; Nakai, C.; Yamada, Y.; Sasaki, M.; Yamamoto, S., Highly oriented monolayer graphite formation on Pt(111) by a supersonic methane beam. *Surf Sci* **2004**, 560 (1-3), 183-190.
78. Marchini, S.; Gunther, S.; Wintterlin, J., Scanning tunneling microscopy of graphene on Ru(0001). *Physical Review B* **2007**, 76 (7).

79. Coraux, J.; N'Diaye, A. T.; Busse, C.; Michely, T., Structural coherency of graphene on Ir(111). *Nano Letters* **2008**, *8* (2), 565-570.
80. Gall', N. R.; Rut'kov, E. V.; Tontegode, A. Y., Interaction of silver atoms with iridium and with a two-dimensional graphite film on iridium: Adsorption, desorption, and dissolution. *Phys Solid State+* **2004**, *46* (2), 371-377.
81. Nandamuri, G.; Roumimov, S.; Solanki, R., Chemical vapor deposition of graphene films. *Nanotechnology* **2010**, *21* (14).
82. Chen, X. D.; Liu, Z. B.; Zheng, C. Y.; Xing, F.; Yan, X. Q.; Chen, Y. S.; Tian, J. G., High-quality and efficient transfer of large-area graphene films onto different substrates. *Carbon* **2013**, *56*, 271-278.
83. Reina, A.; Son, H. B.; Jiao, L. Y.; Fan, B.; Dresselhaus, M. S.; Liu, Z. F.; Kong, J., Transferring and Identification of Single- and Few-Layer Graphene on Arbitrary Substrates. *J Phys Chem C* **2008**, *112* (46), 17741-17744.
84. Suk, J. W.; Kitt, A.; Magnuson, C. W.; Hao, Y. F.; Ahmed, S.; An, J. H.; Swan, A. K.; Goldberg, B. B.; Ruoff, R. S., Transfer of CVD-Grown Monolayer Graphene onto Arbitrary Substrates. *Acs Nano* **2011**, *5* (9), 6916-6924.
85. Liang, X. L.; Sperling, B. A.; Calizo, I.; Cheng, G. J.; Hacker, C. A.; Zhang, Q.; Obeng, Y.; Yan, K.; Peng, H. L.; Li, Q. L.; Zhu, X. X.; Yuan, H.; Walker, A. R. H.; Liu, Z. F.; Peng, L. M.; Richter, C. A., Toward Clean and Crackless Transfer of Graphene. *Acs Nano* **2011**, *5* (11), 9144-9153.
86. Jiao, L. Y.; Fan, B.; Xian, X. J.; Wu, Z. Y.; Zhang, J.; Liu, Z. F., Creation of nanostructures with poly(methyl methacrylate)-mediated nanotransfer printing. *Journal of the American Chemical Society* **2008**, *130* (38), 12612-12618.

87. Li, X. S.; Zhu, Y. W.; Cai, W. W.; Borysiak, M.; Han, B. Y.; Chen, D.; Piner, R. D.; Colombo, L.; Ruoff, R. S., Transfer of Large-Area Graphene Films for High-Performance Transparent Conductive Electrodes. *Nano Letters* **2009**, *9* (12), 4359-4363.
88. Matruglio, A.; Nappini, S.; Naumenko, D.; Magnano, E.; Bondino, F.; Lazzarino, M.; Dal Zilio, S., Contamination-free suspended graphene structures by a Ti-based transfer method. *Carbon* **2016**, *103*, 305-310.
89. Chen, M. G.; Stekovic, D.; Li, W. X.; Arkook, B.; Haddon, R. C.; Bekyarova, E., Sublimation-assisted graphene transfer technique based on small polyaromatic hydrocarbons. *Nanotechnology* **2017**, *28* (25).
90. Zhang, G. H.; Guell, A. G.; Kirkman, P. M.; Lazenby, R. A.; Miller, T. S.; Unwin, P. R., Versatile Polymer-Free Graphene Transfer Method and Applications. *Acs Appl Mater Inter* **2016**, *8* (12), 8008-8016.
91. Wang, D. Y.; Huang, I. S.; Ho, P. H.; Li, S. S.; Yeh, Y. C.; Wang, D. W.; Chen, W. L.; Lee, Y. Y.; Chang, Y. M.; Chen, C. C.; Liang, C. T.; Chen, C. W., Clean-Lifting Transfer of Large-area Residual-Free Graphene Films. *Adv Mater* **2013**, *25* (32), 4521-4526.
92. Yamada, T.; Ishihara, M.; Hasegawa, M., Large area coating of graphene at low temperature using a roll-to-roll microwave plasma chemical vapor deposition. *Thin Solid Films* **2013**, *532*, 89-93.
93. Kalita, G.; Wakita, K.; Umeno, M., Low temperature growth of graphene film by microwave assisted surface wave plasma CVD for transparent electrode application. *Rsc Adv* **2012**, *2* (7), 2815-2820.

94. Khalid, A.; Mohamed, M. A.; Umar, A. A., Graphene Growth at Low Temperatures using RF-Plasma Enhanced Chemical Vapour Deposition. *Sains Malays* **2017**, *46* (7), 1111-1117.
95. Bo, Z.; Ma, W.; Wang, P. X.; Wu, E. K.; Yang, W. C.; Yu, K. H.; Zhang, X. P.; Yan, J. H.; Cen, K. F., Multi-pin dc glow discharge PECVD for uniform growth of vertically oriented graphene at atmospheric pressure. *Phys Status Solidi B* **2014**, *251* (1), 155-161.
96. Miccoli, I.; Edler, F.; Pfnur, H.; Tegenkamp, C., The 100th anniversary of the four-point probe technique: the role of probe geometries in isotropic and anisotropic systems. *J Phys-Condens Mat* **2015**, *27* (22).
97. Bougrine, H.; Ausloos, M., Highly Sensitive Method for Simultaneous Measurements of Thermal-Conductivity and Thermoelectric-Power - Fe and Al Examples. *Rev Sci Instrum* **1995**, *66* (1), 199-206.
98. Kettler, W. H.; Wernhardt, R.; Rosenberg, M., Differential Ac Method of Thermopower Measurement. *Rev Sci Instrum* **1986**, *57* (12), 3053-3058.
99. Sumanasekera, G. U.; Grigorian, L.; Eklund, P. C., Low-temperature thermoelectrical power measurements using analogue subtraction. *Meas Sci Technol* **2000**, *11* (3), 273-277.
100. Elyutin, P. V., Theory of Stimulated Raman Scattering. *Opt Spectrosc-Ussr* **1971**, *30* (2), 131-&.
101. Malard, L. M.; Pimenta, M. A.; Dresselhaus, G.; Dresselhaus, M. S., Raman spectroscopy in graphene. *Phys Rep* **2009**, *473* (5-6), 51-87.

102. Wu, J. B.; Lin, M. L.; Cong, X.; Liu, H. N.; Tan, P. H., Raman spectroscopy of graphene-based materials and its applications in related devices. *Chemical Society Reviews* **2018**, *47* (5), 1822-1873.
103. Begliarbekov, M.; Sul, O.; Kalliakos, S.; Yang, E. H.; Strauf, S., Determination of edge purity in bilayer graphene using mu-Raman spectroscopy. *Applied Physics Letters* **2010**, *97* (3).
104. Wang, H.; Wang, Y. F.; Cao, X. W.; Feng, M.; Lan, G. X., Vibrational properties of graphene and graphene layers. *J Raman Spectrosc* **2009**, *40* (12), 1791-1796.
105. Wang, H. F.; Yamada, C.; Homma, Y., Scanning electron microscopy imaging mechanisms of CVD-grown graphene on Cu substrate revealed by in situ observation. *Japanese Journal of Applied Physics* **2015**, *54* (5).
106. Huang, P. Y.; Ruiz-Vargas, C. S.; van der Zande, A. M.; Whitney, W. S.; Levendorf, M. P.; Kevek, J. W.; Garg, S.; Alden, J. S.; Hustedt, C. J.; Zhu, Y.; Park, J.; McEuen, P. L.; Muller, D. A., Grains and grain boundaries in single-layer graphene atomic patchwork quilts. *Nature* **2011**, *469* (7330), 389-395.
107. Wang, Q. H.; Hersam, M. C., Room-temperature molecular-resolution characterization of self-assembled organic monolayers on epitaxial graphene. *Nat Chem* **2009**, *1* (3), 206-211.
108. Si, Y.; Samulski, E. T., Synthesis of water soluble graphene. *Nano Letters* **2008**, *8* (6), 1679-1682.
109. Elias, D. C.; Nair, R. R.; Mohiuddin, T. M. G.; Morozov, S. V.; Blake, P.; Halsall, M. P.; Ferrari, A. C.; Boukhvalov, D. W.; Katsnelson, M. I.; Geim, A. K.;

- Novoselov, K. S., Control of Graphene's Properties by Reversible Hydrogenation: Evidence for Graphane. *Science* **2009**, 323 (5914), 610-613.
110. Loh, K. P.; Bao, Q. L.; Ang, P. K.; Yang, J. X., The chemistry of graphene. *Journal of Materials Chemistry* **2010**, 20 (12), 2277-2289.
111. Kozbial, A.; Li, Z. T.; Conaway, C.; McGinley, R.; Dhingra, S.; Vahdat, V.; Zhou, F.; D'Urso, B.; Liu, H. T.; Li, L., Study on the Surface Energy of Graphene by Contact Angle Measurements. *Langmuir* **2014**, 30 (28), 8598-8606.
112. Nair, R. R.; Ren, W. C.; Jalil, R.; Riaz, I.; Kravets, V. G.; Britnell, L.; Blake, P.; Schedin, F.; Mayorov, A. S.; Yuan, S. J.; Katsnelson, M. I.; Cheng, H. M.; Strupinski, W.; Bulusheva, L. G.; Okotrub, A. V.; Grigorieva, I. V.; Grigorenko, A. N.; Novoselov, K. S.; Geim, A. K., Fluorographene: A Two-Dimensional Counterpart of Teflon. *Small* **2010**, 6 (24), 2877-2884.
113. Cheng, H. S.; Sha, X. W.; Chen, L.; Cooper, A. C.; Foo, M. L.; Lau, G. C.; Bailey, W. H.; Pez, G. P., An Enhanced Hydrogen Adsorption Enthalpy for Fluoride Intercalated Graphite Compounds. *Journal of the American Chemical Society* **2009**, 131 (49), 17732-17733.
114. Tahara, K.; Iwasaki, T.; Matsutani, A.; Hatano, M., Effect of radical fluorination on mono- and bi-layer graphene in Ar/F-2 plasma. *Applied Physics Letters* **2012**, 101 (16).
115. Chen, M. J.; Zhou, H. Q.; Qiu, C. Y.; Yang, H. C.; Yu, F.; Sun, L. F., Layer-dependent fluorination and doping of graphene via plasma treatment. *Nanotechnology* **2012**, 23 (11).

116. Chen, M. J.; Qiu, C. Y.; Zhou, H. Q.; Yang, H. C.; Yu, F.; Sun, L. F., Fluorination of Edges and Central Areas of Monolayer Graphene by SF₆ and CHF₃ Plasma Treatments. *J Nanosci Nanotechno* **2013**, *13* (2), 1331-1334.
117. Bon, S. B.; Valentini, L.; Verdejo, R.; Fierro, J. L. G.; Peponi, L.; Lopez-Manchado, M. A.; Kenny, J. M., Plasma Fluorination of Chemically Derived Graphene Sheets and Subsequent Modification With Butylamine. *Chem Mater* **2009**, *21* (14), 3433-3438.
118. Lee, K. M.; Lee, S. E.; Lee, Y. S., Effect of Fluorination on Thermal and Mechanical Properties of Carbon Nanotube and Graphene Nanoplatelet Reinforced Epoxy Composites. *Polym-Korea* **2016**, *40* (4), 553-560.
119. Gong, P. W.; Wang, Z. F.; Li, Z. P.; Mi, Y. J.; Sun, J. F.; Niu, L. Y.; Wang, H. G.; Wang, J. Q.; Yang, S. R., Photochemical synthesis of fluorinated graphene via a simultaneous fluorination and reduction route. *Rsc Adv* **2013**, *3* (18), 6327-6330.
120. Meduri, P.; Chen, H. H.; Xiao, J.; Martinez, J. J.; Carlson, T.; Zhang, J. G.; Deng, Z. D., Tunable electrochemical properties of fluorinated graphene. *J Mater Chem A* **2013**, *1* (27), 7866-7869.
121. Zhao, R.; Jayasingha, R.; Sherehiy, A.; Dharmasena, R.; Akhtar, M.; Jasinski, J. B.; Wu, S.-Y.; Henner, V.; Sumanasekera, G. U., In Situ Transport Measurements and Band Gap Formation of Fluorinated Graphene. *The Journal of Physical Chemistry C* **2015**, *119* (34), 20150-20155.
122. Chakrapani, V.; Angus, J. C.; Anderson, A. B.; Wolter, S. D.; Stoner, B. R.; Sumanasekera, G. U., Charge transfer equilibria between diamond and an aqueous oxygen electrochemical redox couple. *Science* **2007**, *318* (5855), 1424-1430.

123. Sidorov, A. N.; Sherehiy, A.; Jayasinghe, R.; Stallard, R.; Benjamin, D. K.; Yu, Q.; Liu, Z.; Wu, W.; Cao, H.; Chen, Y. P.; Jiang, Z.; Sumanasekera, G. U., Thermoelectric power of graphene as surface charge doping indicator. *Applied Physics Letters* **2011**, *99* (1), 013115.
124. Sidorov, A. N.; Gaskill, K.; Buongiorno Nardelli, M.; Tedesco, J. L.; Myers-Ward, R. L.; Eddy, C. R.; Jayasekera, T.; Kim, K. W.; Jayasingha, R.; Sherehiy, A.; Stallard, R.; Sumanasekera, G. U., Charge transfer equilibria in ambient-exposed epitaxial graphene on (0001 $\bar{1}$) 6 H-SiC. *J Appl Phys* **2012**, *111* (11), 113706.
125. Jayasingha, R.; Sherehiy, A.; Wu, S. Y.; Sumanasekera, G. U., In situ study of hydrogenation of graphene and new phases of localization between metal-insulator transitions. *Nano Lett* **2013**, *13* (11), 5098-105.
126. von Lohneysen, H., Electron-electron interactions and the metal-insulator transition in heavily doped silicon. *Ann Phys-Berlin* **2011**, *523* (8-9), 599-611.
127. Helgren, E.; Gruner, G.; Ciofalo, M. R.; Baxter, D. V.; Carini, J. P., Measurements of the complex conductivity of Nb_xSi_{1-x} alloys on the insulating side of the metal-insulator transition. *Physical Review Letters* **2001**, *87* (11), art. no.-116602.
128. Mott, N., The Mobility Edge and the 8-N Rule - a Citation Classic Commentary on Conduction in Non-Crystalline Materials .3. Localized States in a Pseudogap and near Extremities of Conduction and Valence Bands by Mott,N.F. *Cc/Eng Tech Appl Sci* **1989**, (27), 12-12.
129. Robinson, J. T.; Burgess, J. S.; Junkermeier, C. E.; Badescu, S. C.; Reinecke, T. L.; Perkins, F. K.; Zalalutdniov, M. K.; Baldwin, J. W.; Culbertson, J. C.; Sheehan, P.

- E.; Snow, E. S., Properties of Fluorinated Graphene Films. *Nano Letters* **2010**, *10* (8), 3001-3005.
130. Wang, B.; Wang, J. J.; Zhu, J., Fluorination of Graphene: A Spectroscopic and Microscopic Study. *Acs Nano* **2014**, *8* (2), 1862-1870.
131. Wang, Z. F.; Wang, J. Q.; Li, Z. P.; Gong, P. W.; Liu, X. H.; Zhang, L. B.; Ren, J. F.; Wang, H. G.; Yang, S. R., Synthesis of fluorinated graphene with tunable degree of fluorination. *Carbon* **2012**, *50* (15), 5403-5410.
132. McCann, E.; Kechedzhi, K.; Fal'ko, V. I.; Suzuura, H.; Ando, T.; Altshuler, B. L., Weak-localization magnetoresistance and valley symmetry in graphene. *Physical Review Letters* **2006**, *97* (14).
133. Hong, X.; Cheng, S. H.; Herding, C.; Zhu, J., Colossal negative magnetoresistance in dilute fluorinated graphene. *Physical Review B* **2011**, *83* (8).
134. Morozov, S. V.; Novoselov, K. S.; Katsnelson, M. I.; Schedin, F.; Elias, D. C.; Jaszczak, J. A.; Geim, A. K., Giant intrinsic carrier mobilities in graphene and its bilayer. *Physical Review Letters* **2008**, *100* (1).
135. Li, Y. F.; Zhou, Z.; Shen, P. W.; Chen, Z. F., Spin Gapless Semiconductor-Metal-Half-Metal Properties in Nitrogen-Doped Zigzag Graphene Nanoribbons. *Acs Nano* **2009**, *3* (7), 1952-1958.
136. Wang, X. R.; Li, X. L.; Zhang, L.; Yoon, Y.; Weber, P. K.; Wang, H. L.; Guo, J.; Dai, H. J., N-Doping of Graphene Through Electrothermal Reactions with Ammonia. *Science* **2009**, *324* (5928), 768-771.

137. Qu, L. T.; Liu, Y.; Baek, J. B.; Dai, L. M., Nitrogen-Doped Graphene as Efficient Metal-Free Electrocatalyst for Oxygen Reduction in Fuel Cells. *Acs Nano* **2010**, *4* (3), 1321-1326.
138. Reddy, A. L. M.; Srivastava, A.; Gowda, S. R.; Gullapalli, H.; Dubey, M.; Ajayan, P. M., Synthesis Of Nitrogen-Doped Graphene Films For Lithium Battery Application. *Acs Nano* **2010**, *4* (11), 6337-6342.
139. Wang, Y.; Shao, Y. Y.; Matson, D. W.; Li, J. H.; Lin, Y. H., Nitrogen-Doped Graphene and Its Application in Electrochemical Biosensing. *Acs Nano* **2010**, *4* (4), 1790-1798.
140. Gong, K. P.; Du, F.; Xia, Z. H.; Durstock, M.; Dai, L. M., Nitrogen-Doped Carbon Nanotube Arrays with High Electrocatalytic Activity for Oxygen Reduction. *Science* **2009**, *323* (5915), 760-764.
141. Huang, B., Electronic properties of boron and nitrogen doped graphene nanoribbons and its application for graphene electronics. *Physics Letters A* **2011**, *375* (4), 845-848.
142. Geng, D. S.; Chen, Y.; Chen, Y. G.; Li, Y. L.; Li, R. Y.; Sun, X. L.; Ye, S. Y.; Knights, S., High oxygen-reduction activity and durability of nitrogen-doped graphene. *Energ Environ Sci* **2011**, *4* (3), 760-764.
143. Zhou, X. S.; Wan, L. J.; Guo, Y. G., Binding SnO₂ Nanocrystals in Nitrogen-Doped Graphene Sheets as Anode Materials for Lithium-Ion Batteries. *Adv Mater* **2013**, *25* (15), 2152-2157.
144. Wang, H. B.; Zhang, C. J.; Liu, Z. H.; Wang, L.; Han, P. X.; Xu, H. X.; Zhang, K. J.; Dong, S. M.; Yao, J. H.; Cui, G. L., Nitrogen-doped graphene nanosheets with

- excellent lithium storage properties. *Journal of Materials Chemistry* **2011**, *21* (14), 5430-5434.
145. Wen, Z. H.; Wang, X. C.; Mao, S.; Bo, Z.; Kim, H.; Cui, S. M.; Lu, G. H.; Feng, X. L.; Chen, J. H., Crumpled Nitrogen-Doped Graphene Nanosheets with Ultrahigh Pore Volume for High-Performance Supercapacitor. *Adv Mater* **2012**, *24* (41), 5610-5616.
146. Zhang, C. K.; Lin, W. Y.; Zhao, Z. J.; Zhuang, P. P.; Zhan, L. J.; Zhou, Y. H.; Cai, W. W., CVD synthesis of nitrogen-doped graphene using urea. *Sci China Phys Mech* **2015**, *58* (10).
147. Liu, Y.; Dai, D.; Jiang, N., Synthesis of the Nitrogen-doped CVD Graphene through Triazine. *J Inorg Mater* **2017**, *32* (5), 517-522.
148. Sheng, Z. H.; Shao, L.; Chen, J. J.; Bao, W. J.; Wang, F. B.; Xia, X. H., Catalyst-Free Synthesis of Nitrogen-Doped Graphene via Thermal Annealing Graphite Oxide with Melamine and Its Excellent Electrocatalysis. *Acs Nano* **2011**, *5* (6), 4350-4358.
149. Terasawa, T.; Saiki, K., Synthesis of Nitrogen-Doped Graphene by Plasma-Enhanced Chemical Vapor Deposition. *Japanese Journal of Applied Physics* **2012**, *51* (5).
150. Wang, C. D.; Yuen, M. F.; Ng, T. W.; Jha, S. K.; Lu, Z. Z.; Kwok, S. Y.; Wong, T. L.; Yang, X.; Lee, C. S.; Lee, S. T.; Zhang, W. J., Plasma-assisted growth and nitrogen doping of graphene films. *Applied Physics Letters* **2012**, *100* (25).

151. Wang, H. B.; Maiyalagan, T.; Wang, X., Review on Recent Progress in Nitrogen-Doped Graphene: Synthesis, Characterization, and Its Potential Applications. *Acs Catalysis* **2012**, *2* (5), 781-794.
152. Sidorov, A. N.; Sherehiy, A.; Jayasinghe, R.; Stallard, R.; Benjamin, D. K.; Yu, Q. K.; Liu, Z. H.; Wu, W.; Cao, H. L.; Chen, Y. P.; Jiang, Z. G.; Sumanasekera, G. U., Thermoelectric power of graphene as surface charge doping indicator. *Applied Physics Letters* **2011**, *99* (1).
153. Zhao, R.; Afaneh, T.; Dharmasena, R.; Jasinski, J.; Sumanasekera, G.; Henner, V., Study of nitrogen doping of graphene via in-situ transport measurements. *Physica B: Condensed Matter* **2016**, *490*, 21-24.
154. Wang, H.; Maiyalagan, T.; Wang, X., Review on Recent Progress in Nitrogen-Doped Graphene: Synthesis, Characterization, and Its Potential Applications. *ACS Catalysis* **2012**, *2* (5), 781-794.
155. Wehling, T. O.; Lichtenstein, A. I.; Katsnelson, M. I., First-principles studies of water adsorption on graphene: The role of the substrate. *Applied Physics Letters* **2008**, *93* (20).
156. Bergmann, G., Weak Localization in Thin-Films - a Time-of-Flight Experiment with Conduction Electrons. *Phys Rep* **1984**, *107* (1), 1-58.
157. Li, X.; Zhuang, J. C.; Sun, Y.; Bai, J.; Zafar, Z. N.; Ni, Z. H.; Jin, B. B.; Shi, Z. X., Enhancement of weak localization for nitrogen-doped graphene by short range potentials. *Carbon* **2015**, *82*, 346-352.
158. Mousavi, H., Graphene as Gas Sensors. *Commun Theor Phys* **2011**, *56* (2), 373-376.

159. Yuan, W. J.; Shi, G. Q., Graphene-based gas sensors. *J Mater Chem A* **2013**, *1* (35), 10078-10091.
160. Reshak, A. H.; Auluck, S., Adsorbing H₂S onto a single graphene sheet: A possible gas sensor. *J Appl Phys* **2014**, *116* (10).
161. Berahman, M.; Sheikhi, M. H., Hydrogen sulfide gas sensor based on decorated zigzag graphene nanoribbon with copper. *Sensor Actuat B-Chem* **2015**, *219*, 338-345.
162. Lebedev, A. A.; Lebedev, S. P.; Novikov, S. N.; Davydov, V. Y.; Smirnov, A. N.; Litvin, D. P.; Makarov, Y. N.; Levitskii, V. S., Supersensitive graphene-based gas sensor. *Tech Phys+* **2016**, *61* (3), 453-457.
163. Hakimi, M.; Salehi, A.; Boroumand, F. A.; Mosleh, N., Fabrication of a Room Temperature Ammonia Gas Sensor Based on Polyaniline With N-Doped Graphene Quantum Dots. *Ieee Sens J* **2018**, *18* (6), 2245-2252.
164. Ovsianytskyi, O.; Nam, Y. S.; Tsymbalenko, O.; Lan, P. T.; Moon, M. W.; Lee, K. B., Highly sensitive chemiresistive H₂S gas sensor based on graphene decorated with Ag nanoparticles and charged impurities. *Sensor Actuat B-Chem* **2018**, *257*, 278-285.
165. Choi, H.; Jeong, H. Y.; Lee, D. S.; Choi, C. G.; Choi, S. Y., Flexible NO₂ gas sensor using multilayer graphene films by chemical vapor deposition. *Carbon Lett* **2013**, *14* (3), 186-189.
166. Novikov, S.; Lebedeva, N.; Satrapinski, A., Ultrasensitive NO₂ Gas Sensor Based on Epitaxial Graphene. *J Sensors* **2015**.

167. Ngo, Y. L. T.; Hur, S. H., Low-temperature NO₂ gas sensor fabricated with NiO and reduced graphene oxide hybrid structure. *Mater Res Bull* **2016**, *84*, 168-176.
168. Huang, X. L.; Hu, N. T.; Zhang, L. L.; Wei, L. M.; Wei, H.; Zhang, Y. F., The NH₃ sensing properties of gas sensors based on aniline reduced graphene oxide. *Synthetic Met* **2013**, *185*, 25-30.
169. DaSilva, A. M.; Cole, M. W., Effects of Physically Adsorbed Films on Conductivity of Two-Dimensional Metal Surfaces and Graphene. *Journal of Low Temperature Physics* **2011**, *163* (3-4), 122-130.
170. Maiga, S. M.; Gatica, S. M., Monolayer adsorption of noble gases on graphene. *Chem Phys* **2018**, *501*, 46-52.
171. Neek-Amal, M.; Lajevardipour, A., Stochastic motion of noble gases on a graphene sheet. *Computational Materials Science* **2010**, *49* (4), 839-844.
172. Ambrosetti, A.; Silvestrelli, P. L., Adsorption of Rare-Gas Atoms and Water on Graphite and Graphene by van der Waals-Corrected Density Functional Theory. *J Phys Chem C* **2011**, *115* (9), 3695-3702.
173. Abbaspour, M.; Akbarzadeh, H.; Salemi, S.; Sherafati, M., Molecular dynamics simulation of noble gas adsorption on graphite: New effective potentials including many-body interactions. *J Mol Liq* **2016**, *222*, 915-922.
174. Zhang, Y. B.; Small, J. P.; Amori, M. E. S.; Kim, P., Electric field modulation of galvanomagnetic properties of mesoscopic graphite. *Physical Review Letters* **2005**, *94* (17).

175. Gomez-Navarro, C.; Weitz, R. T.; Bittner, A. M.; Scolari, M.; Mews, A.; Burghard, M.; Kern, K., Electronic transport properties of individual chemically reduced graphene oxide sheets. *Nano Letters* **2007**, *7* (11), 3499-3503.
176. Kudin, K. N.; Ozbas, B.; Schniepp, H. C.; Prud'homme, R. K.; Aksay, I. A.; Car, R., Raman spectra of graphite oxide and functionalized graphene sheets. *Nano Letters* **2008**, *8* (1), 36-41.
177. Niyogi, S.; Bekyarova, E.; Itkis, M. E.; McWilliams, J. L.; Hamon, M. A.; Haddon, R. C., Solution properties of graphite and graphene. *Journal of the American Chemical Society* **2006**, *128* (24), 7720-7721.
178. Rutter, G. M.; Crain, J. N.; Guisinger, N. P.; Li, T.; First, P. N.; Stroschio, J. A., Scattering and interference in epitaxial graphene. *Science* **2007**, *317* (5835), 219-222.
179. Faugeras, C.; Nerriere, A.; Potemski, M.; Mahmood, A.; Dujardin, E.; Berger, C.; de Heer, W. A., Few-layer graphene on SiC, pyrolytic graphite, and graphene: A Raman scattering study. *Applied Physics Letters* **2008**, *92* (1).
180. Wood, J. D.; Schmucker, S. W.; Lyons, A. S.; Pop, E.; Lyding, J. W., Effects of Polycrystalline Cu Substrate on Graphene Growth by Chemical Vapor Deposition. *Nano Letters* **2011**, *11* (11), 4547-4554.
181. Zhang, Y.; Gomez, L.; Ishikawa, F. N.; Madaria, A.; Ryu, K.; Wang, C. A.; Badmaev, A.; Zhou, C. W., Comparison of Graphene Growth on Single-Crystalline and Polycrystalline Ni by Chemical Vapor Deposition. *J Phys Chem Lett* **2010**, *1* (20), 3101-3107.

182. Yao, Y. G.; Wong, C. P., Monolayer graphene growth using additional etching process in atmospheric pressure chemical vapor deposition. *Carbon* **2012**, *50* (14), 5203-5209.
183. Zhang, Y. F.; Gao, T.; Xie, S. B.; Dai, B. Y.; Fu, L.; Gao, Y. B.; Chen, Y. B.; Liu, M. X.; Liu, Z. F., Different growth behaviors of ambient pressure chemical vapor deposition graphene on Ni(111) and Ni films: A scanning tunneling microscopy study. *Nano Research* **2012**, *5* (6), 402-411.
184. Song, W.; Jeon, C.; Kim, S. Y.; Kim, Y.; Kim, S. H.; Lee, S. I.; Jung, D. S.; Jung, M. W.; An, K. S.; Park, C. Y., Two selective growth modes for graphene on a Cu substrate using thermal chemical vapor deposition. *Carbon* **2014**, *68*, 87-94.
185. Faggio, G.; Capasso, A.; Messina, G.; Santangeo, S.; Dikonimos, T.; Gagliardi, S.; Giorgi, R.; Morandi, V.; Ortolani, L.; Lisi, N., High-Temperature Growth of Graphene Films on Copper Foils by Ethanol Chemical Vapor Deposition. *J Phys Chem C* **2013**, *117* (41), 21569-21576.
186. Gao, T.; Xie, S. B.; Gao, Y. B.; Liu, M. X.; Chen, Y. B.; Zhang, Y. F.; Liu, Z. F., Growth and Atomic-Scale Characterizations of Graphene on Multifaceted Textured Pt Foils Prepared by Chemical Vapor Deposition. *Acs Nano* **2011**, *5* (11), 9194-9201.
187. Yao, Y. G.; Li, Z.; Lin, Z. Y.; Moon, K. S.; Agar, J.; Wong, C. P., Controlled Growth of Multilayer, Few-Layer, and Single-Layer Graphene on Metal Substrates. *J Phys Chem C* **2011**, *115* (13), 5232-5238.
188. Guermoune, A.; Chari, T.; Popescu, F.; Sabri, S. S.; Guillemette, J.; Skulason, H. S.; Szkopek, T.; Siaj, M., Chemical vapor deposition synthesis of graphene on

- copper with methanol, ethanol, and propanol precursors. *Carbon* **2011**, *49* (13), 4204-4210.
189. Dong, X. C.; Wang, P.; Fang, W. J.; Su, C. Y.; Chen, Y. H.; Li, L. J.; Huang, W.; Chen, P., Growth of large-sized graphene thin-films by liquid precursor-based chemical vapor deposition under atmospheric pressure. *Carbon* **2011**, *49* (11), 3672-3678.
190. Reina, A.; Jia, X. T.; Ho, J.; Nezich, D.; Son, H. B.; Bulovic, V.; Dresselhaus, M. S.; Kong, J., Layer Area, Few-Layer Graphene Films on Arbitrary Substrates by Chemical Vapor Deposition. *Nano Letters* **2009**, *9* (8), 3087-3087.
191. Cai, C. Y.; Jia, F. X.; Li, A. L.; Huang, F.; Xu, Z. H.; Qiu, L. Z.; Chen, Y. Q.; Fei, G. T.; Wang, M., Crackless transfer of large-area graphene films for superior-performance transparent electrodes. *Carbon* **2016**, *98*, 457-462.
192. Malesevic, A.; Vitchev, R.; Schouteden, K.; Volodin, A.; Zhang, L.; Tendeloo, G. V.; Vanhulsel, A.; Haesendonck, C. V., Synthesis of few-layer graphene via microwave plasma-enhanced chemical vapour deposition. *Nanotechnology* **2008**, *19* (30), 305604.
193. Bo, Z.; Yang, Y.; Chen, J.; Yu, K.; Yan, J.; Cen, K., Plasma-enhanced chemical vapor deposition synthesis of vertically oriented graphene nanosheets. *Nanoscale* **2013**, *5* (12), 5180-204.
194. Yamada, T.; Kim, J.; Ishihara, M.; Hasegawa, M., Low-temperature graphene synthesis using microwave plasma CVD. *Journal of Physics D: Applied Physics* **2013**, *46* (6), 063001.

195. Chen, S.; Gao, M.; Cao, R.; Du, H.; Yang, J.; Zhao, L.; Ma, Z., Hydrogen-free synthesis of graphene–graphitic films directly on Si substrate by plasma enhanced chemical vapor deposition. *Journal of Materials Science: Materials in Electronics* **2014**, *26* (3), 1485-1493.
196. Woehrl, N.; Ochedowski, O.; Gottlieb, S.; Shibasaki, K.; Schulz, S., Plasma-enhanced chemical vapor deposition of graphene on copper substrates. *AIP Advances* **2014**, *4* (4), 047128.
197. Othman, M.; Ritikos, R.; Hafiz, S. M.; Khanis, N. H.; Rashid, N. M. A.; Rahman, S. A., Low-temperature plasma-enhanced chemical vapour deposition of transfer-free graphene thin films. *Mater Lett* **2015**, *158*, 436-438.
198. Xu, Z. G.; Zheng, R. J.; Khanaki, A.; Zuo, Z.; Liu, J. L., Direct growth of graphene on in situ epitaxial hexagonal boron nitride flakes by plasma-assisted molecular beam epitaxy. *Applied Physics Letters* **2015**, *107* (21).
199. Sun, J.; Chen, Y.; Cai, X.; Ma, B.; Chen, Z.; Priyadarshi, M. K.; Chen, K.; Gao, T.; Song, X.; Ji, Q.; Guo, X.; Zou, D.; Zhang, Y.; Liu, Z., Direct low-temperature synthesis of graphene on various glasses by plasma-enhanced chemical vapor deposition for versatile, cost-effective electrodes. *Nano Research* **2015**, *8* (11), 3496-3504.
200. Ferrari, A. C.; Meyer, J. C.; Scardaci, V.; Casiraghi, C.; Lazzeri, M.; Mauri, F.; Piscanec, S.; Jiang, D.; Novoselov, K. S.; Roth, S.; Geim, A. K., Raman spectrum of graphene and graphene layers. *Physical Review Letters* **2006**, *97* (18).

201. Dimiev, A.; Kosynkin, D. V.; Sinitiskii, A.; Slesarev, A.; Sun, Z. Z.; Tour, J. M., Layer-by-Layer Removal of Graphene for Device Patterning. *Science* **2011**, *331* (6021), 1168-1172.
202. Zhou, H. L.; Yu, W. J.; Liu, L. X.; Cheng, R.; Chen, Y.; Huang, X. Q.; Liu, Y.; Wang, Y.; Huang, Y.; Duan, X. F., Chemical vapour deposition growth of large single crystals of monolayer and bilayer graphene. *Nature Communications* **2013**, *4*.
203. Yang, C. Y.; Bi, H.; Wan, D. Y.; Huang, F. Q.; Xie, X. M.; Jiang, M. H., Direct PECVD growth of vertically erected graphene walls on dielectric substrates as excellent multifunctional electrodes. *J Mater Chem A* **2013**, *1* (3), 770-775.
204. Mao, S.; Yu, K. H.; Chang, J. B.; Steeber, D. A.; Ocola, L. E.; Chen, J. H., Direct Growth of Vertically-oriented Graphene for Field-Effect Transistor Biosensor. *Sci Rep-Uk* **2013**, *3*.
205. Mott, N. F., Conduction in non-crystalline materials. *Philos Mag* **1969**, *19* (160), 835-852.
206. Nang, T. T.; Okuda, M.; Matsushita, T.; Yokota, S.; Suzuki, A., Electrical and Optical-Properties of Ge-Xse-1-X Amorphous Thin-Films. *Japanese Journal of Applied Physics* **1976**, *15* (5), 849-853.
207. Jonson, M.; Mahan, G. D., Mott Formula for the Thermopower and the Wiedemann-Franz Law. *Physical Review B* **1980**, *21* (10), 4223-4229.
208. Kishimoto, K.; Tsukamoto, M.; Koyanagi, T., Temperature dependence of the Seebeck coefficient and the potential barrier scattering of n-type PbTe films

prepared on heated glass substrates by rf sputtering. *J Appl Phys* **2002**, 92 (9), 5331-5339.

209. Ulybyshev, M. V.; Katsnelson, M. I., Magnetism and Interaction-Induced Gap Opening in Graphene with Vacancies or Hydrogen Adatoms: Quantum Monte Carlo Study. *Physical Review Letters* **2015**, 114 (24).
210. Bae, S.; Kim, H.; Lee, Y.; Xu, X. F.; Park, J. S.; Zheng, Y.; Balakrishnan, J.; Lei, T.; Kim, H. R.; Song, Y. I.; Kim, Y. J.; Kim, K. S.; Ozyilmaz, B.; Ahn, J. H.; Hong, B. H.; Iijima, S., Roll-to-roll production of 30-inch graphene films for transparent electrodes. *Nature Nanotechnology* **2010**, 5 (8), 574-578.

CURRICULUM VITAE

NAME: Rong Zhao

ADDRESS: Department of Physics and Astronomy
102 Natural Science Building
University of Louisville
Louisville, KY, 40292

EMAIL: ZHAOROONG@GMAIL.COM

EDUCATION:

Ph. D.: Department of Physics & Astronomy University of Louisville – Kentucky, U.S.A	August 2018 GPA: 4/4
Master: Department of Physics & Astronomy University of Louisville – Kentucky, U.S.A	August 2015 GPA: 3.92/4
Master: Department of Physics Shanghai University – Shanghai, China	July 2013
Bachelor: Optical Information Sciences and Technology Xidian University – Xi'an, China	July 2008

PUBLICATIONS & PRESENTATIONS:

1. “Electrical transport properties of graphene nanowalls grown at low temperature using PECVD” Rong Zhao, M. Akhtar, A. Alruqi, J. Jasinski, G. Sumanasekera. *Mater. Res. Express* 4 (2017) 055007.
2. “Study of nitrogen doping of graphene via in-situ transport measurements”. Rong Zhao, T. Afaneh, R. Dharmasena, J. Jasinski, G. Sumanasekera, V. Henner. *Physica B* 490 (2016) 21–24.
3. “In Situ Transport Measurements and Band Gap Formation of Fluorinated Graphene”. Rong Zhao, R. Jayasingha, A. Sherehiy, R. Dharmasena, M. Akhtar, J. Jasinski, Shi-Yu Wu, V. Henner and G. Sumanasekera. *J. Phys. Chem. C* (2015), 119, 20150–20155.
4. “Photoluminescence in Functionalized/Doped Graphene Quantum Dots: Role of Surface States”, Uliana Salgaeva, Rong Zhao, Sergey Mushinsky, Jacek Jasinski, Xiao-An Fu, Victor Henner, Ruchira Dharmasena, Gamini Sumanasekera. *J Nanomater Mol Nanotechnol* (2017) 6:2.
5. “Recent Advances in Synthesis, Properties, and Applications of Phosphorene”, M. Akhtar, G. Anderson, Rong Zhao, A. Alruqi, J. Mroczkowska, G. Sumanasekera, J. Jasinski. *NPJ 2D Materials and Applications* (2017) 1:5.
6. “Effect of Y₂O₃ Seed Layer on Epitaxial Growth of Oxide Barrier Layer for YBCO Coated Conductor”, Rong Zhao, F. Fan, W. B. Qiu, Y. M. Lu, Z. Y. Liu, C. Y. Bai, Y. Q. Guo, and C. B. Cai, *Applied Superconductivity*, VOL. 23, NO. 3, June (2013).
7. “Epitaxial growth of Gd₂Zr₂O₇/Y₂O₃ buffer layers for YBa₂Cu₃O_{7-δ} coated conductors”, Y.M. Lu, Rong Zhao, Z. Y. Liu, and B. Holzapfel, *Physica C* 485 (2013) 15-19.
8. “Low temperature synthesis of graphene on arbitrary substrates and its transport properties” Oral presentation, APS march meeting (2017), New Orleans, Louisiana
9. “Synthesis&Plasma Functionalize of Graphene and its transport properties” Oral

presentation, GSRRC (2018), University of Louisville, Kentucky

AWARDS

- The Iyad Khair Scholarship Award for Outstanding Performance in Physics, University of Louisville, Department of Physics and Astronomy (2015)
- Featured Graduate Student in the College of Arts and Sciences, University of Louisville (2017)
- GSC Travel Funding, School of Interdisciplinary and Graduate Studies, University of Louisville (2016-2017)
- Arts and Sciences Research & Creative Activities Award, College of Arts and Sciences, University of Louisville (2017-2018)
- The Manuel Schwartz Award for Outstanding Graduate Performance in Physics, University of Louisville (2018)